FAILURE PROPERTIES OF NANOCRYSTALLINE FCC METALLIC ULTRATHIN FILMS

A Dissertation
Presented to
The Academic Faculty

By

Ehsan Hosseinian

In Partial Fulfillment
of the Requirements for the Degree
Doctor of Philosophy in the
George W. Woodruff School of Mechanical Engineering

Georgia Institute of Technology
August 2016

FAILURE PROPERTIES OF NANOCRYSTALLINE FCC METALLIC ULTRATHIN FILMS

Approved by:

Dr. Olivier N. Pierron, Advisor
George W. Woodruff School of
Mechanical Engineering
Georgia Institute of Technology

Dr. Stephen D. Antolovich
George W. Woodruff School of
Mechanical Engineering
Georgia Institute of Technology

Dr. David L. McDowell
George W. Woodruff School of
Mechanical Engineering
Georgia Institute of Technology

Dr. Ting Zhu,
George W. Woodruff School of
Mechanical Engineering
Georgia Institute of Technology

Dr. Hamid Garmesani,
George W. Woodruff School of
Mechanical Engineering
Georgia Institute of Technology

Date Approved: May 10, 2016

To my parents, Hamimeh and Issa

&

To my wife, Zeynab

ACKNOWLEDGEMENTS

A number of people in my life have contributed greatly to my educational path and to this thesis. First and foremost I would like to thank my adviser, Prof. Olivier N. Pierron, for giving me the opportunity to be part of his research group at Georgia Tech. I cannot find words to express my gratitude for his availability toward students, for his generous support and guidance over the course of my Ph.D. I hope the professional relationship that we built during my Ph.D. study continue well beyond graduate school.

My special thanks go to Dr. Marc Legros, who generously offered his knowledge, expertise, and time during my internship in France without which a key part of my work would not have been completed.

I would also like to thank my other committee members, Dr. McDowell, Dr. Garmestani, Dr. Zhu, and Dr. Antolovich, for all their valuable insight, discussion and comments to this dissertation. Their assistance brought me up to speed and enriched my insight. In addition, I would like to thank my senior colleagues, especially Brian Allen and Eva Baumert and Bhaskar Pant who served as my mentors from the early stages of this journey. I would also like to appreciate the camaraderie of my friends and colleagues Farzad Sadeghi-Tohidi and Kyungjin

Kim, Sushruta Surappa and Hamid Ebrahimi. Special thanks to Saurabh Gupta whose post-processing routines I used in the dissertation. His help in analyzing the raw data to calculate stress and strain was instrumental. In addition, I would like to thank Georgia Tech's Institute for Electronics and Nanotechnology staff, especially Eric Woods, Charlie Sue, Tiejun Zhang and Garry Spinner for training and tool trouble-shooting. Special thank you my dear friend and roommate Seyed Parsa Banihashemi for sharing your point of view with me and helping me.

Last but not least, I would like to thank my family, whose care and concern I felt all this time, despite being half-way around the world. They invariably offered their sincere support, never-ending encouragement, and unconditional love.

TABLE OF CONTENTS

LIST OF TABLES

LIST OF FIGURES

LIST OF SYMBOLS AND ABBREVIATIONS

V_{act}	Activation Volume
$\vec{b}$	Burgers Vector
E	Elastic Modulus
ε_0	Electric Permittivity of Air, $\varepsilon_0 = 8.854\times10^{-12}$ F/m
R	Load Ratio
ε_p	Plastic Strain
$\dot{\varepsilon}_p$	Plastic Strain Rate
n	Power-law Exponent
m	Strain-rate Sensitivity Factor
σ_Y	Yield Stress
γ_{utf}	Unstable Twinning Fault Energy
γ_{usf}	Unstable Stacking Fault Energy
AFM	Atomic Force Microscopy
BCC	Body Centered Cubic
BF	Bright Field
CG	Coarse Grain
ECAP	Equal-Channel Angular Pressing.
ED	Electrodeposition

FCC	Face Centered Cubic
FIB	Focused Ion Beam
GB	Grain Boundary
HAGBs	High-Angle Grain Boundaries.
HCF	High Cycle Fatigue
HCP	Hexagonal-Close-Packed
HRTEM	High-Resolution Transmission Electron Microscopy
LCF	Low Cycle Fatigue
MD	Molecular Dynamics
MEMS	Microelectromechanical Systems
MS	Molecular Statics
NC	Nanocrystalline
NEMS	Nanoelectromechanical Systems
PSB	Persistent Slip Band
RIE	Reactive Ion Etching
SEM	Scanning Electron Microscope
SF	Stacking Fault
SFE (γ_{sf})	Stacking Fault Energy
SOI	Silicon-On-Insulator
SPD	Severe Plastic Deformation
TEM	Transmission Electron Microscope
TKD	Transmission Kikuchi Diffraction

UFG	Ultra-fine Grained

SUMMARY

This dissertation presents the investigation of failure properties of nanocrystalline FCC metallic ultrathin films. For this purpose, a unique MEMS-based experimental technique is presented to perform quantitative *in situ* TEM uniaxial mechanical testing on nanocrystalline ultrathin films. The MEMS device provides both actuation and sensing of the specimen via electrical signals while TEM imaging could provide information on the microstructure evolution during deformation. Compared to previously demonstrated MEMS-based *in situ* TEM techniques, the MEMS takes advantage of two identical capacitive sensors on each side of the specimen that are used to measure both the specimen elongation and applied force with nano-meter and micro-newton precision, respectively. Specimens were manipulated and fixed onto the MEMS device without the use of a focused ion-beam microscope and therefore, eliminating ion-beam related damage to the tested specimen. The major advantage of the technique is its capability to use TEM imaging solely for high magnification microstructural observations while the MEMS device provides continuous tracking of the material's response, thereby expanding the capabilities of MEMS-based techniques towards more complex *in situ* TEM nanomechanical tests. MEMS devices were previously used to investigate monotonic behaviors at small scales. This work is the first in using a MEMS to (1) investigate the monotonic and fatigue properties of nanocrystalline ultrathin gold films. The 100-nm-thick, 1.5-μm-wide NC Au specimens have a tensile strength of

~1-1.13 GPa, and a total elongation to failure of ~2.8-5%. The specimens exhibit a ratcheting behavior under tension-tension cyclic loading in near stress-controlled conditions. Nanoscale fatigue cracks were observed after nearly 7000 cycles for σ_{max} ~0.8 GPa. (2) Investigate the viscoplastic behavior of nanocrystalline gold thin films by performing *in situ* stress relaxation experiments. Upon successive relaxation segments, the power-law exponent n continuously decreases from initial large values (n from 6 to 14 at $t = 0$) to low values (n ~1-2) if the test is long enough (several hours). The *in situ* TEM results show that the transient relaxation behavior under large stresses is accommodated by sustained dislocation motion, either intergranular or transgranular, only in a few grains (the larger grains (above ~200 nm) that are favorably oriented for maximum shear in the main glide plane. Over time, the dislocation sources, located in or close to grain boundary and triple junctions, become less operative as a result of the decrease in applied stress or exhausted, likely leading to a transition to a GB-diffusion based mechanism. However, most of these sources are robust enough to produce additional dislocations upon increase of the applied stress, contributing to significantly larger ductility than for monotonic tests by maintaining localized shear regions. (3) Study crack growth behavior for two types of nanocrystalline gold films with different thickness and grain size distribution. For the 100-nm-thick films, there exist both intragranular and intergranular deformation mechanisms. Based on *in situ* TEM observation, dislocations flow along the grain boundaries, leading to grain boundary sliding. The initiated sharp cracks blunt and grow slowly along the grain

boundaries during the stress relaxation segments without requiring to increase the stress even after tens of minutes. In contrast, for 30-nm-thick film, intergranular crack grows mainly via the growth of nanocracks that occurs due to GB decohesion ahead of the main crack and that eventually coalesce with the main crack. Most of the GB decohesion occurs during the loading steps or at the very beginning (i.e. within the first minute) of the holding steps. In contrast to 100 nm films it is required to increase the stress for the cracks in 30-nm-thick film to grow further. The outcome of this research significantly advances the fundamental understanding regarding the mechanical reliability of nanostructured metallic thin film devices.

CHAPTER I

BACKGROUND AND MOTIVATION

In this chapter we start with a brief introduction on thin film technology (section 1.1) followed by an overview of fabrication techniques of nanocrystalline thin films (section 1.2). In section 1.3 mechanical testing techniques, including that of nanostructured metals, are introduced. In section 1.4, we continue with a description of the current understanding of failure properties in NC metals (monotonic plasticity, creep, fatigue and fracture) and related size effects. Finally, a short section 1.5 highlights the motivation for this thesis.

1.1 Introduction

Thin film technology is pervasive in many applications, including optics, microelectronics and structural components in micro/nano electromechanical systems (MEMS/NEMS). Optical components usually have thin layers of various materials such as aluminum, gold and silver to alter optical and physical properties [1, 2]. Nanocrystalline (NC) usually refers to an average grain size smaller than 100 nm. Another important area for thin film applications is in flexible microelectronics which promises new functionalities and cheaper fabrication processes. Flexible electronic devices integrate diverse inorganic materials including thin film metals on a polymer substrate. Recently, thin films were successfully grown on flexible plastic

substrates at low temperatures, compatible with polymeric substrates [3]. By patterning the metal or addition of a buffer layer between the metallic film and substrate, the polymer substrate could carry most of the deformation while the thin metallic film undergo small strains [4-6]. In recent years signi cant progress is also being made in the realization and fabrication of thin- lm transistors which are the fundamental building blocks for state-of-the-art microelectronics, such as at-panel and system-on-glass displays [7-10]. Extensive investigation has been performed to study the reliability of thin-film transistors. For example, mechanisms of instabilities caused by the sole applied gate bias stress and that combined with temperature and/or environmental effects have been investigated [11-14]. The third and one of the foremost applications of metallic thin films is for micro and nano-electromechanical systems (MEMS/NEMS). Superior material properties along with cheap and relatively simple technologies make thin film metals as a basic and key components for MEMS devices such as pressure sensors, accelerometers, resonators and gyroscopes [15-17].

Reliability is a critical issue in any of the aforementioned applications of thin films and a major hurdle to commercialization of MEMS devices [18]. A major reliability problem associated with these devices is the time-dependent degradation and fatigue failure of the materials. In most cases, thin films are under stress, either due to repeated surface contact, vibration-induced fatigue or thermally-induced stresses.

1.2 Fabrication of Ultrathin Films

There are numerous techniques for fabrication of NC materials. First, we focus on bottom-up processes where the nanostructure is built atom by atom and layer by layer. Metallic thin films are usually deposited using chemical or physical methods such as electrodeposition, chemical vapor deposition (CVD), plasma-enhanced CVD, atomic layer deposition (ALD), electron beam evaporation or magnetron sputtering. Each method has some advantages over the other regarding the controlling the physical parameters of deposition, deposition time and microstructure characteristics. For example, electrodeposition has some advantages over other methods for synthesizing NC films: (1) Electrodeposition enables the less expensive processing of NC metals with grain sizes down to a few nanometers and a narrow grain size distribution [19] with a high deposition rate and a better chance of adaptation in today's electroplating industry. (2) The material usually exhibits a high density, although some nanoporosity has been reported [20].

On the other hand, physical vapor deposition (PVD) technique is more compatible with other microfabrication process in cleanroom for fabrication of freestanding cantilevers. In PVD techniques the metal is deposited in ultrahigh vacuum chamber leading to a very uniform nanostructure and high purity of the thin film by reducing the pollution effect. This is a crucial factor for mechanical properties of thin films as existence of 0.001% of impurity and level of vacuum could drastically change the ductility and corresponding deformation mechanisms [21-23]. As such, impurities, also play a big role in the thermal stability of NC

nanostructures, a critical issue in the development of commercial materials [23]. Typical microstructure of physical evaporation, made of columnar grains; with a particular texture and average grain size and grain size distribution in which all depends on thickness, deposition temperature and vacuum pressure and deposition method [24, 25] as shown in Figure 1.1. Several grains over the thickness could be also achieved by repeated interruptions of the deposition process [24] but the grain size could not exceed the thickness of the film due to geometrical constraint.

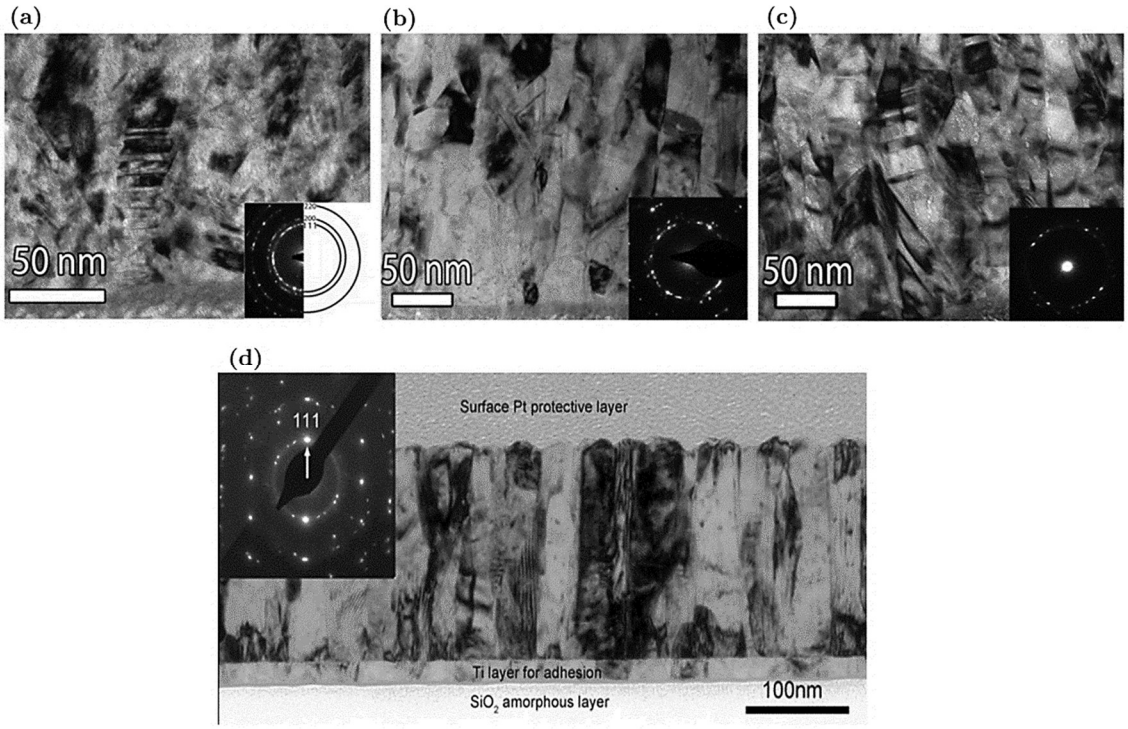

Figure 1.1 BF TEM image and corresponding diffraction pattern of 310 nm thick Pd film deposited by electron beam evaporation at (a) 0.3 Å/s (b) 1 Å/s and (c) 5 Å/s [24]. (d) BF micrograph of cross-sectional FIB specimen, prepared with sputtering, with the inset shows the <111> texture parallel to normal of the film [25].

Small specimens and thin films could also be produced by top-bottom approaches. A widely used method is Focused Ion Beam (FIB), often with Ga ions, which allows machining small structures with micron sizes down to hundreds of

nanometers [26-30]. This method is now routinely available in many experimental laboratories and does not necessitate clean room environment. It is also predominantly used in manipulation of specimen onto the testing stage. However, this technique suffers several drawbacks, including possible compliance of the Pt clamps, Pt overspray covering the surface of the specimen, and ion-beam damage of the specimen's surface (See section 2.3 for more details). Thus, investigations into alternative methods for preparing and manipulating ultrathin materials is needed to prevent damage to the samples.

1.3 Nanomechanical Testing Methodologies of Free-standing Specimens

Measuring mechanical properties of small-scale objects usually require the development of new testing methodologies. The goal is to determine quantitative properties such as elastic modulus, flow stress, strain-rate sensitivity, fracture stress and endurance limit etc. in small volumes. In addition, a qualitative understanding of the governing mechanisms of plasticity is of great interest to material scientists. Many conventional macro-testing techniques have simply been scaled down [31-33], but other novel techniques such as bulge testing, and AFM-based techniques, microresonators and nanoindentation have been also developed [34-37] (see Figure 1.2 for a number of existing setups). Tensile testing is the most important and desirable testing method, mainly due to the specimen's uniform one dimensional stress state [38]. Compression and bending modes are also widely used in above mentioned techniques (see Figure 1.2 for various experimental setups). Any of these

techniques could be implemented under optical or electron microscope which gives direct observation in an optical or electron microscope that could bring important understandings of deformation mechanisms. As such, quantitative *in situ* testing provides an opportunity to observe the microstructure evolution during deformation of the specimen, while both the applied force and deformation are measured. This powerful technique has been employed extensively over the past 10 years to investigate the monotonic deformation of metallic nanospecimens and ultrathin films [39]. Among the existing *in situ* TEM testing techniques, the MEMS based techniques [40] have evolved tremendously since the pioneering work of Haque and Saif [41-43]. Notably, Espinosa and coworkers have demonstrated the use of MEMS components (thermal actuator, comb structures) for *in situ* TEM actuation and load sensing [44-46]. These state-of-the-art MEMS based techniques are mostly suited for short experiments (such as monotonic loading to failure) given the time-consuming digital image correlation process of measuring apparent or local strain. These strains are measured based on relatively low magnification electron images of the entire specimen, during which the evolution of the microstructure cannot be observed in great details. Similar constraints have also inhibited the progress to conduct both *in situ* and *ex situ* nanostructure characterization. Therefore, more advanced and versatile setups than the leading MEMS techniques are required to address these concerns and limitations.

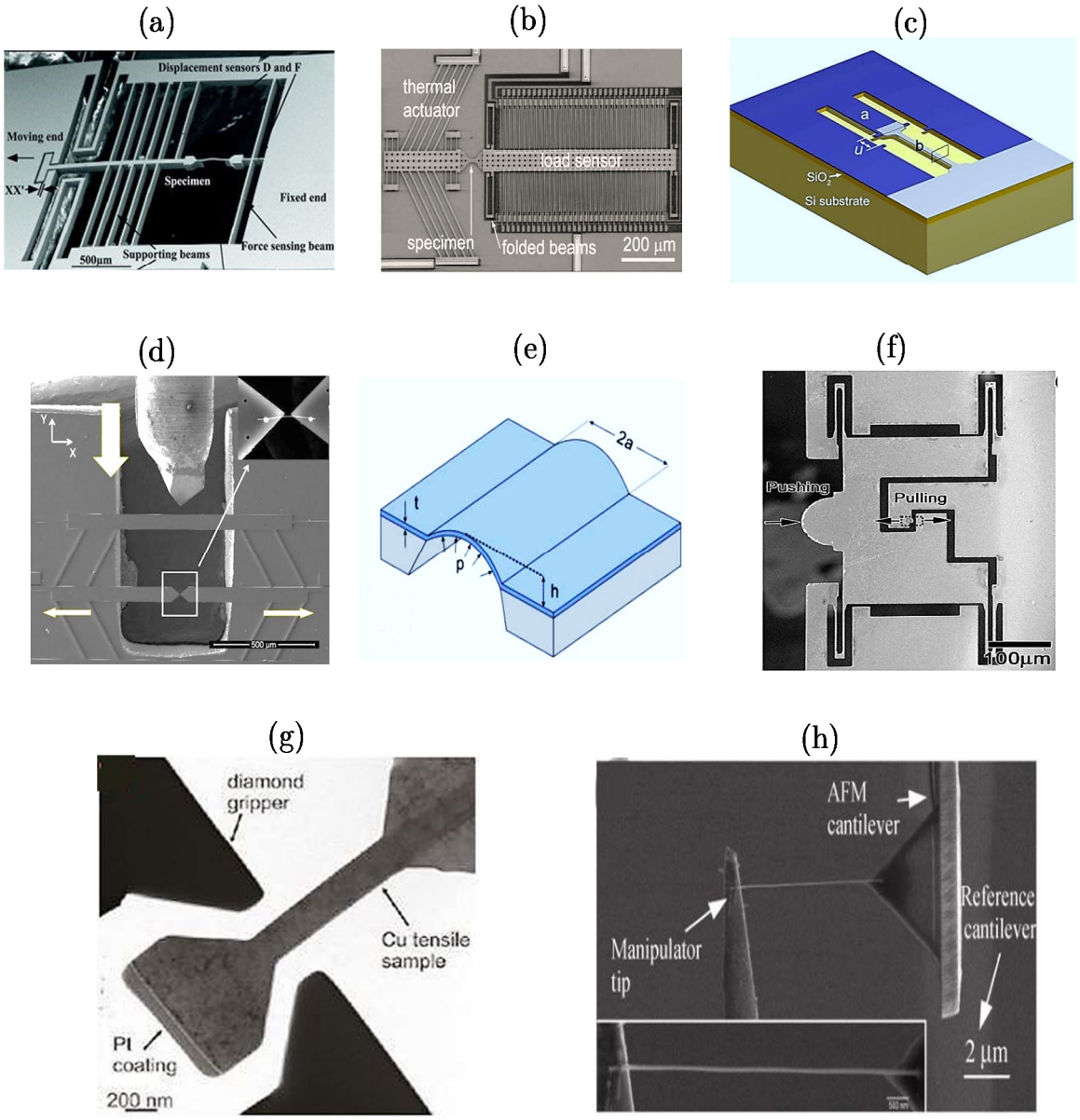

Figure 1.2 Various experimental set ups for nanomechanical testing of freestanding thin films and/or nanowires: (a) SEM micrograph of the microstage showing the freestanding thin-film specimen being attached to the force sensor beam at one end and to supporting beams at the other [43]. (b) The MEMS platform consisting of a thermal actuator and capacitive load sensor [45]. (c) Schematic of on-chip tensile testing stage [47]. (d) SEM image showing the geometry of the fabricated device and the nanoindenter tip. Arrows show the direction of movement of the top shuttle and sample stage shuttles upon load application. The inset shows a close up image of a mounted Ni nanowire sample [48]. e) Membrane for bulge testing [49]. (f) SEM image of push-to-pull MEMS-based testing system by Hysitron for *in situ* TEM testing [50]. (g) Modified Hysitron nanoindenter tip to probe tensile properties of nanomaterials [51]. (h) SEM micrograph of nanowire mechanical testing configuration with AFM cantilever [48].

1.4 Failure Properties of NC Metals

NC metals, having superior mechanical strength to conventional coarse-grained counter-parts, offers the possibility of a new metallurgical pathway to improve the failure properties of thin films [52-58]. Failure properties of NC metals, including thin films, are size-dependent and cannot be extrapolated from bulk counterparts and are still an open challenge. Therefore, it is of great importance to understand failure behavior of NC thin films including the sources of plasticity in nano-sized grains.

1.4.1 Monotonic Plasticity

The deformation behavior of NC metals has attracted extensive interest in recent years. In the literature, results show that NC pure FCC metals are characterized by ultra-high strength compared to the corresponding coarser-grained metals [53, 58-62]. NC copper with an average grain size of 23 nm exhibited a hardness of about 20 times greater than its large-grained counterpart [63]. Yield strengths as high as 1 GPa for Cu (average grain size: 10 nm) [64] and 2.4 GPa for Ni (average grain size: 20 nm) were measured [61]. According to atomistic simulations, FCC metals initially nucleate partial dislocations. As such, the metal with high γ_{sf} is able to emit second partials to form perfect dislocations and thus entering the 'perfect dislocation slip' regime [65, 66]. MD simulations also show that maximum yield strength in Cu occurred at grain size of 10–15 nm [67]. This study along with some others implies that there is a reverse trend, the so called "Inverse Hall-Petch" relationship [68, 69]. Such a maximum strength has also been confirmed

experimentally [70]. Recent experiments have also shown a significant dependence of flow stress on strain rate and temperature [71-73].

The above-mentioned unique properties of NC FCC metals clearly suggest a departure in plastic deformation mechanisms from the conventional trans-granular dislocation processes in CG metals. As the grain size becomes smaller the dislocation-mediated processes becomes increasingly more difficult and grain boundary-assisted mechanisms become increasingly more important. Limited available sources for dislocation processes leads to activation of alternative deformation mechanisms including grain boundary (GB) sliding [74, 75], grain rotation [76, 77], grain growth [78, 79] and twinning [21, 22, 80] as shown in Figure 1.3.

In addition to flow stress, ductility is the most explored mechanical property of NC materials. It is a crucial property to possess in order for NC materials to be practically competitive as new functional materials. The ductility of NC metals is subjected to considerable experimental variation. According to the experimental results for NC materials, elongation to failure depends on geometrical constraints (thin film vs. bulk material), microstructural heterogeneities (such as grain size distribution), and the presence of processing flaws such as porosities and contamination. Plastic instability is also another major limiting factor, leading to localized shear band formation due to limited strain hardening capacity. However, introduction of a high density of nanoscale growth twins can significantly enhance the strain hardening capacity [81-83]. For example, unexpected large strain hardening for NC Pd thin films has been reported recently [21]. This large

strength/ductility balance was mainly attributed to presence of nanotwins. Nanotwin acts as a barrier for dislocation motion and a new source for dislocation nucleation and interactions. There is also a significant size-dependence of mechanical properties on the twin lamellar spacing much like the grain size dependence of the strength in NC metals [81-83]. These interactions between nanotwins and dislocations have been studied extensively by atomistic simulations. For example dislocation/coherent TB interactions for FCC nano-twinned systems with a twin spacing between 1 to 25 nm with average grain size between 10 to 70 nm were studied [84, 85]. Geometrical constraints (as opposed to microstructural constraint such as grain size and twin spacing) could also be another crucial factor on plasticity in small scale. For example it is argued that the constraints on geometry of specimens can expedite nucleation and motion of dislocations in sub-micrometer-sized crystals [86-88]. Thickness is the dimensional constraint for plasticity of thin films. Therefore, it is evident that the deformation mechanisms in thin lms are also affected by the presence of free surfaces [89, 90]. For example, the free surface exerts attractive image forces on the dislocation. Moreover, if the surface is impenetrable for dislocations (for example by localized fatigue-induce surface oxide [37]) dislocation loops requires to fit inside the film [91]. In such cases it is essential to superpose thin-film effect with grain size and other possible hardening mechanisms which may not be trivial.

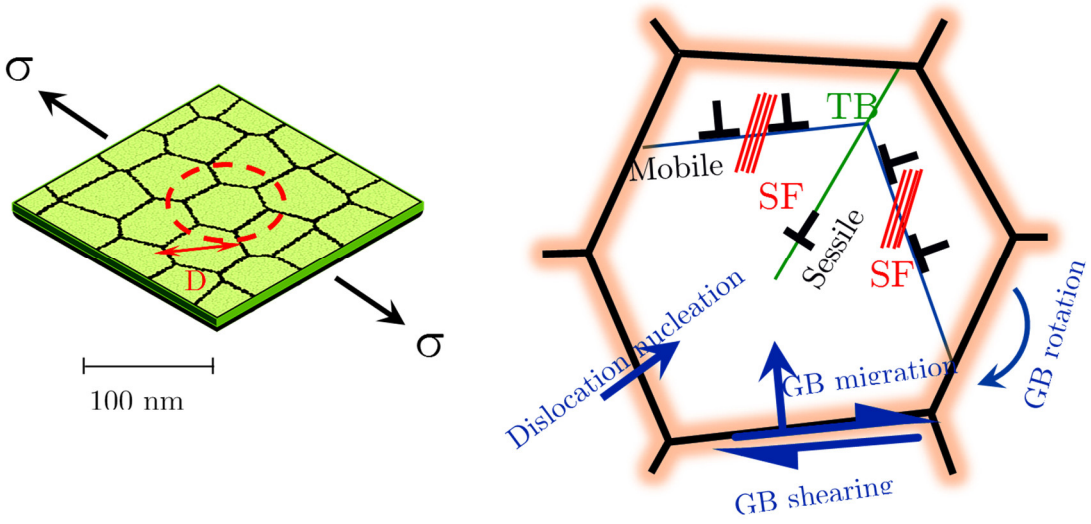

Figure 1.3 Summary of possible source of plasticity in nanocrystalline FCC metals including dislocation [22] and/or grain boundary-mediated plasticity [78].

1.4.2 Creep

There have been reports of increased strain rate sensitivity with decreasing grain size in metals [53, 54, 64, 71, 73, 83, 92]. For FCC metals, which is normally rate sensitive, with a strain rate exponent m (defined as $m = \frac{\partial \ln \sigma}{\partial \ln \dot{\varepsilon}}$) hardening exponent on the order of 0.001, goes up in the value to the order of 0.01 and higher when the grain size is less than 100 nm [53, 55, 73, 92]. The strain rate dependence of the deformation behavior should shed light on the operating mechanisms. This is being determined by V_{act}, which is a microscopic quantity and a real signature of the operating deformation mechanism. The increased rate sensitivity and the resulting reduced activation volume were attributed to grain boundary-mediated mechanisms with small activation volumes ($<$10-20 b^3), resulting in a large strain rate sensitivity of the NC metals compared to coarse-grained metals. The competition between inter and intragranular deformation mechanisms is expected to

control rate sensitivity and the activation volumes in nanocrystalline metals. While higher strain rate sensitivity could help some limited increase in the ductility of NC metals, this could also lead to significant stress relaxation and/or creep deformation even at room temperature. High strain rate sensitivity of NC materials and susceptibility of small grains to creep in room temperature brings the importance of creep deformation. This could occur due to reduced values for activation volume and thermally activated mechanisms for NC metals. The significant increase in the volume fraction of grain boundaries and intergranular defects such as triple junctions, affecting the creep mechanisms, complicates finding models to understand the deformation process. Figure 1.4 shows a deformation mechanism map for pure nickel [93, 94]. It is expected that the boundary lines, shown in Figure 1.4, are pushed towards the top and/or the right as grain size decreases [53, 93]. This is because in NC metals extremely small grain sizes make it difficult for intragranular sources to operate and leave little possibility for cross slip, but offer a high density of non-equilibrium grain boundaries, GB dislocation sources and pinning sites [53, 95, 96]. Low-stress compression tests of NC-Ni at room temperature on nano/micro-pillars along with other studies on tensile testing of NC metals suggest that the creep could be dominated by diffusion-controlled mechanisms such as GB diffusion and GB sliding [73, 97-100]. MD simulations also reveal that under relatively high tensile stresses, NC palladium indeed exhibits steady-state diffusion creep with a strain rate that agrees well with the quantitative Coble-creep formula [101]. The steady state

creep properties of thin films are also extrinsic and should show strong dependence on thickness and grain size [53, 54, 64, 73, 83].

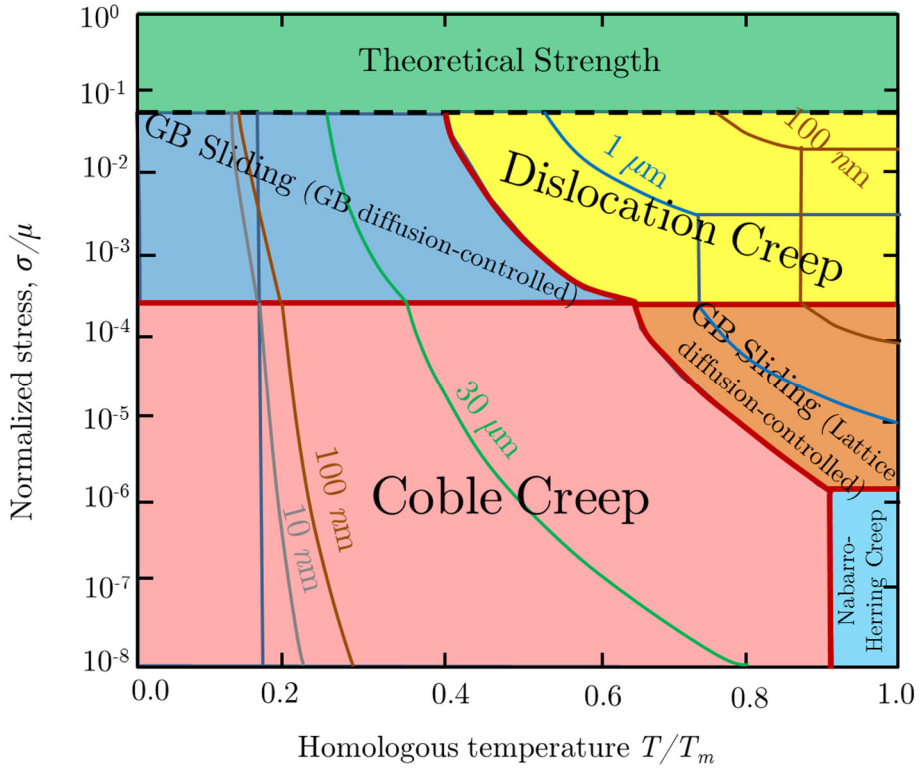

Figure 1.4 A schematic, showing grain-size-dependent deformation mechanism map for steady state creep of pure nickel [93]

Based on the abovementioned studies, steady state creep deformation mechanisms have been well characterized in NC metals. While steady state creep response of NC metals is important, from a reliability viewpoint, the steady state creep properties are not sufficient, as transient (primary) creep deformation can also play a significant role. More importantly, from a scientific viewpoint, the governing mechanisms for transient creep remain elusive, due to the lack of *in situ* observation of this phenomenon. Hence, mainly hypotheses have been formulated so far to explain transient creep in these materials, such as diffusional processes at the extended grain boundaries, or dislocation motion with concurrent dislocation source

exhaustion. Van Swygenhoven and coworkers studied the dynamic recovery mechanisms in NC Ni using *in situ* X-ray diffraction stress reduction experiments [98, 102]. Based on the evolution of the diffraction peak width, they concluded that the recovery processes are mainly dictated by the competition between grain boundary accommodation and dislocation generation [98, 102].

1.4.3 Fatigue

Many attractive above-mentioned features of NC metals, such as high strength would likely be unavailing if the fatigue resistance of these materials does not meet certain minimum acceptable levels for particular demands.

It is now well-known that fatigue crack initiation in conventional coarse grain pure FCC metals is triggered by extrusion-mediated surface roughness as presented in Figure 1.5 [103, 104]. This roughness occurs at the intersection of free surface and persistent slip bands (PSBs) and is a direct consequence of cyclic microplasticity [105]. In the saturation stage of the cyclic loading, strain is highly localized near PSBs. Ultimately cyclic irreversibilities along PSBs trigger the formation of protrusions [106, 107]. The corners of protrusions, with irreversible slip-unslip, are the preferential sites for fatigue crack initiation [108, 109]. This sequence of events is regarded as conventional for fatigue crack nucleation in pure mono-crystalline and coarse grain FCC metals. One of the most comprehensive theories of surface relief formation is based on the hypothesis that the origin of irreversibility for the motion of PSBs is dislocation pair annihilation and generation of vast number of vacancies within PSBs [110].

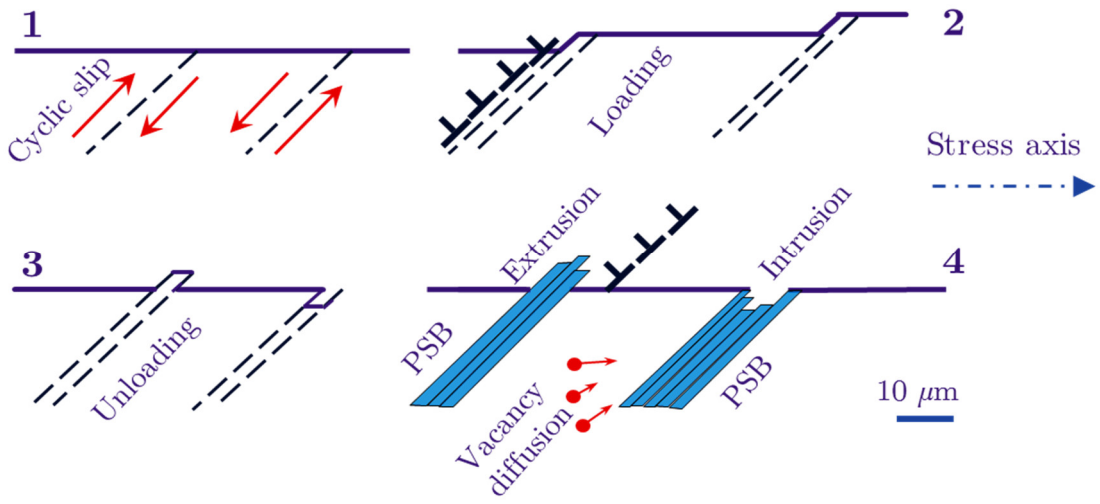

Figure 1.5 Schematic diagram of stages before crack nucleation in fatigued coarse grain FCC metals

The PSB-based models are unlikely to apply for NC metallic thin films, as the typical micron-size PSBs are too large to form within nano-grains. This is only true when the structure of the grains are stable; otherwise, cyclic stress-assisted grain growth could lead to conventional fatigue mechanisms by PSB formation in coarsened grains [58, 111-114]

While the size effects of grain size on plasticity of metals are beginning to be well understood, there is so far little mechanistic interpretation of the size effects in fatigue mechanisms. Moreover, limited quantitative data are available for cyclic plasticity and fatigue damage accumulation. One possible reason for the paucity of this information could be experimental challenges for fabrication of pure thin film specimens along with difficulties for performing valid fatigue tests in small scale. Moreover, due to high strain rate sensitivity, NC metals can also creep at room temperature and therefore it is difficult to distinguish time-dependent degradation from cycle-dependent deformation [72, 73, 115]. Despite these challenges, there are a

few experimental data on the fatigue properties of FCC metals with submicron grain size, summarized below.

Early experimental studies on fatigued ultrafine grain (UFG) specimens show enhanced fatigue life for the high-cycle fatigue (HCF)regime compared to the behavior of CG material, while fatigue life in the low-cycle fatigue (LCF) range decreased [116-121]. This trend is attributed to an improved resistance to fatigue crack initiation, responsible for the HCF regime, and reduced ductility which is a governing factor for LCF. This also makes NC metals more susceptible for fatigue crack growth [58]. Crack path tortuosity also decreases with grain refinement [58]. Sequential loading and unloading of heterogeneous NC Aluminum and gold films exhibits a large Bauschinger effect. This behavior is much less pronounced for homogeneous NC and coarse grain counterparts [119, 122, 123]. This phenomenon has been attributed to heterogeneous microstructure of the sample, inducing back stress at grain boundaries [122, 124]. Recent studies also show that engineering microstructure to a bimodal grain structure could be an approach to optimize the fatigue life by transition from nanograins at the surface to larger grains in the core [125]. As such, the small grains help to improve resistance to crack initiation while the larger grains enhance the ductility of the microstructure. Molecular simulations showed that for columnar grain structure with no texture and grain size of 6 nm, crack propagation is mainly due to nano-void formation ahead of the crack [69]. Although atomistic simulations are promising they are still limited by length and time scale, too short for crack extension and study of fatigue mechanisms.

Fatigue crack initiation in NC FCC metals were also observed both at regions with localized stresses at the specimen's surface [113] or from internal microstructural defects [126] while no TEM work was performed to investigate the source of damage formation in NC metals.

1.4.4 Fracture

Overall, there is only little information on the fracture and crack behavior of NC metals and a lot needs to be done to understand the fundamental properties. One reason could be the fact that it is difficult to measure fracture toughness in small scale for NC thin films because the specimen geometry cannot fulfill the ASTM testing standards [127]. More importantly linear fracture mechanics' basic assumptions are not generally true for NC films as the remaining un-cracked ligament should be at least twenty times larger than the crack tip plastic zone size [58, 127]. Metallic thin film have low fracture toughness and inferior resistance to crack propagation when compared to conventional coarse grained bulk form of the same metal [128, 129]. Atomistic simulations on NC Ni (grain sizes ranging from 5 to 10-12 nm) revealed that the amplified stresses ahead of the crack tip trigger intra-granular dislocations that would otherwise not occur in such small grains [69, 130, 131]. Figure 1.6 shows the emission of leading and trailing Shockley partial dislocations from the crack tip and neighboring [130]. The large stresses also result in grain boundary decohesion and nano-void formation which coalesce with the main crack, leading to intergranular fracture (in contrast to the typical trans-granular cracking in coarse-grained metals).

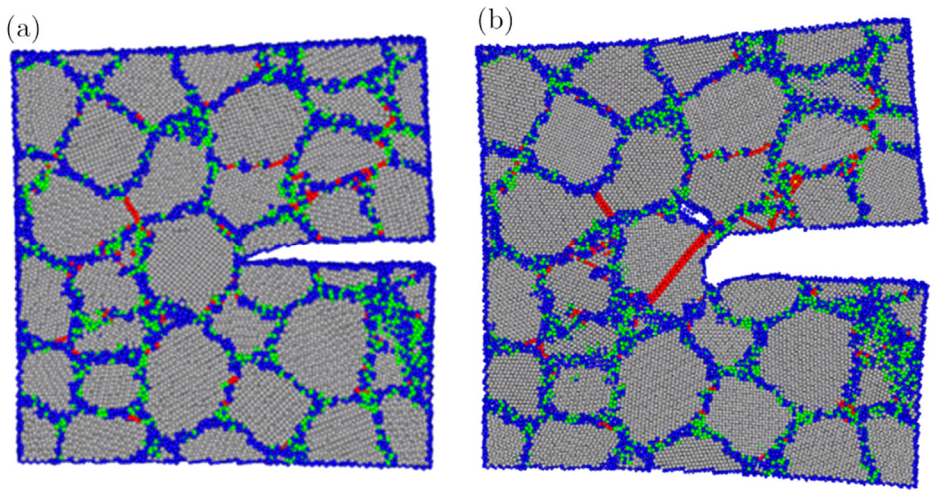

Figure 1.6 Intergranular crack propagation in nanocrystalline Ni with a mean grain size of 10 nm [130]

However, other simulations on NC Al (grain size: 5 nm) ahead of a "blunt" crack (or nano-notch, with a root radius of 5 nm) highlighted the role of grain rotation (similar to the Ashby-Verral mechanism [132]) ahead of the notch, which resulted in a homogeneous (gradient free) stress field and led to the conclusion that NC metals may be insensitive to stress concentration [133]. Such discrepancy highlights the challenges in capturing the governing crack growth mechanisms in NC metals.

A few experimental studies have been carried out to unveil the crack propagation mechanisms using *in situ* TEM observations on ultrathin films (<200 nm) [134-142]. It is important to realize that these studies may not be representative of bulk NC metals, due to the thin film effects [137, 143]. Nonetheless, *in situ* TEM experiments provide a unique opportunity to observe the deformation mechanisms at the crack tip and directly compare them with atomistic simulations. Most of these *in situ* TEM observations revealed intergranular crack growth via nucleation and

growth of nanovoids at triple junctions and/or grain boundary nanocracks, and their coalescence to the main crack, as predicted by atomic simulations [69, 130, 131], even though the studied grain sizes are significantly larger (electroplated Ni with average grain size of 30 nm and narrow grain size distribution (unknown thickness) [137], 100-nm-thick pulsed laser deposited Ni with grain size ranging from 5 to 30 nm [135], 125-nm-thick sputter-deposited Al with grains ranging from 35 to 420 nm (average grain size: 130 nm) [134], and 60-nm-thick sputter-deposited Ag with grains ranging from 10 to 120 nm (average grain size: 40 nm) [142]). These studies mainly observed trans-granular dislocation activities that led to the coalescence events, sometimes due to necking of the connecting regions. Most studies did not observe grain boundary dislocations or grain rotation in the cracking process [134, 135, 137].

1.5 Motivation for Study

Based on the abovementioned background, there is a lack of clear and comprehensive understanding in failure properties of NC metallic films. This is partly because of intrinsic challenges involved in nanomechanical testing. For example post-mortem characterization makes it challenging to understand the complex microstructure evolution and defect formation during the cyclic or creep loading and therefore it is crucial to have direct observations during loading. In the existing quantitative *in situ* TEM testing techniques, there are limitations that do not allow users to conduct long nanomechanical tests such as fatigue and creep experiments on ultrathin films while achieving direct high-resolution measurements and observations.

While the understanding of monotonic properties of NC metals have been significantly improved, comprehensible understanding of cyclic deformation and fatigue crack initiation mechanisms for UFG/NC metals is still missing. Therefore, further experiments along with direct observation of microstructure evolution are required to elucidate fatigue behavior of nano-grains. Creep experiments can also help to further understand possible fatigue-creep interactions and deconvolution of time dependent and cycle dependent mechanisms given the high strain rate sensitivity of NC materials and susceptibility of NC metals to creep in room temperature. More importantly, the governing mechanisms for transient creep remain elusive, due to the lack of quantitative *in situ* observation of this phenomenon. In addition, only a few experimental studies have been carried out to unveil the effect of grain size distribution and film thickness on mechanisms of crack propagation and failure over time for ultrathin NC freestanding films.

This research investigates the failure properties of nanocrystalline FCC metallic ultra-thin films by introducing a versatile MEMS-based nanomechanical experimental setup. The quantitative *in situ* TEM approach in this study provides an opportunity to observe the microstructure evolution during deformation of the nanospecimen, while mechanical quantities such as, stress, strain, elastic modulus and plastic accumulation could be captured by monitoring the evolution of the stress-strain curve over long period of times or large number of cycles. In this thesis, it has been demonstrated that the experimental technique works well for monotonic, fatigue and stress relaxation experiments. Specifically the transient relaxation and

mechanisms of crack growth are investigated for NC metallic thin films thanks to *in situ* TEM observations. These quantitative analyses along with real time observation allow us to further improve the understanding of fundamental deformation mechanisms in NC metallic ultrathin films.

CHAPTER II

NANOMECHANICAL TESTING TECHNIQUE: DEVELOPMENT AND CHARACTERIZATION

This chapter deals with the development and extensive characterization of a MEMS device for the tensile testing of nanostructures. In section 2.1, the details of the experimental technique and calculation of stress and strain along with calibrations of the MEMS are reported. These devices are fabricated with the SOIMUMPs process from MEMSCAP; see section 2.1.3 for an overview of the fabrication process. An extensive characterization of the MEMS device is performed experimentally as well as with finite element modeling in section 2.1.5. In section 2.2, the fabrication and characterization of NC thin film specimens is explained. This chapter concludes with the advantages and outstanding challenges of this technique in section 2.4 and 2.5.

2.1 MEMS-based Nanotensile Tester:

Our MEMS is a bulk micro-machined device, made of single crystalline Si with 10-micron-thick structural layer and is isolated from the wafer by a 1-micron-thick oxide layer. It comprises a thermal actuator, a specimen gap, two capacitive sensors located on each side of the specimen gap, and a load sensor as shown in Figure 2.1 and Figure 2.2. All these components are fabricated over a through-wafer

window, for TEM imaging purpose. The experiments rely on this MEMS device that provides both actuation and sensing of the specimen via electrical signals, while TEM imaging provides information on the microstructure evolution during deformation.

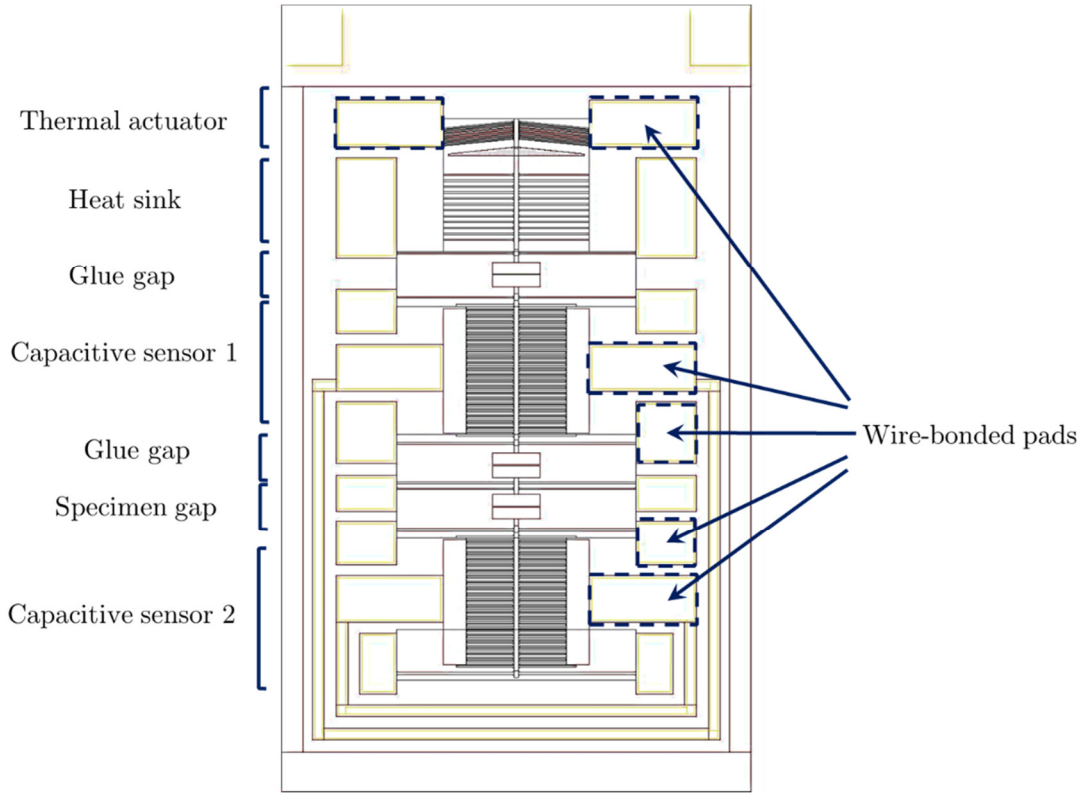

Figure 2.1 Schematic layout of MEMS device with a description of its different components.

2.1.2 Principle of Operation

In this section, the main role and physical principle of operation for each of the device's component will be briefly explained:

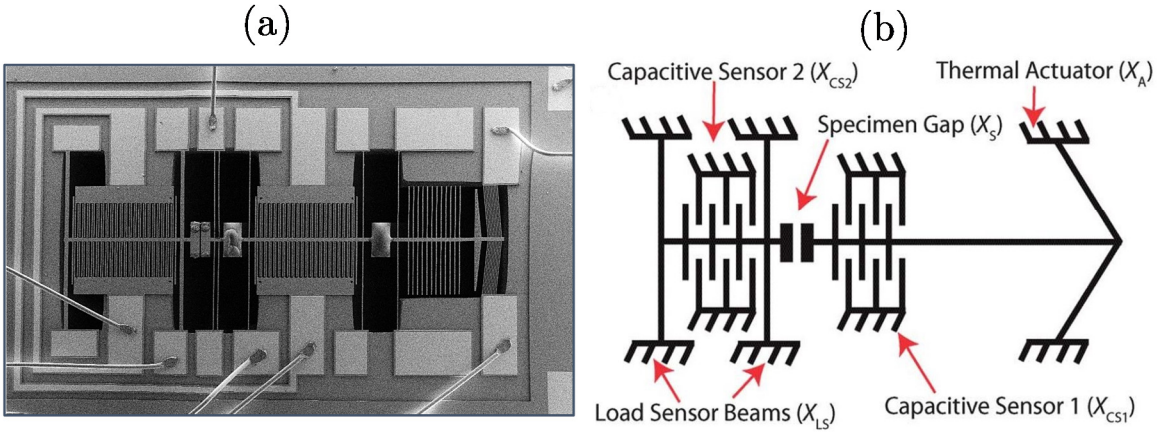

Figure 2.2 (a) SEM image of a wirebonded MEMS device. (b) Corresponding schematic, with a description of its components and their displacements

2.1.2.2 Thermal Actuator

The thermal actuator, working based on Joule heating, consists of 10 pairs of beams inclined at 5°, providing a displacement X_A for an input voltage, V_{in}, applied across the beams. The thermal actuator provides the necessary loading for tensile testing of the nanospecimens. A potential difference applied across the V-shaped symmetric actuator beams, causes a current to flow through the actuator as shown in Figure 2.3. This results in a temperature increase in the actuator beams due to Joule heating, which in turn causes the thermal expansion of these beams. The actuator can provide $X_A = 1.6$ μm for $V_{in} = 4$ V without any appreciable increase in temperature ($<$10 °C) near the specimen, thanks to a heat sink located next to the actuator and a large distance ($>$1 mm) between the actuator and the specimen [144]. Consequently a net displacement of the actuator is obtained (due to symmetry) leading to tensile loading on the specimen placed across the specimen gap.

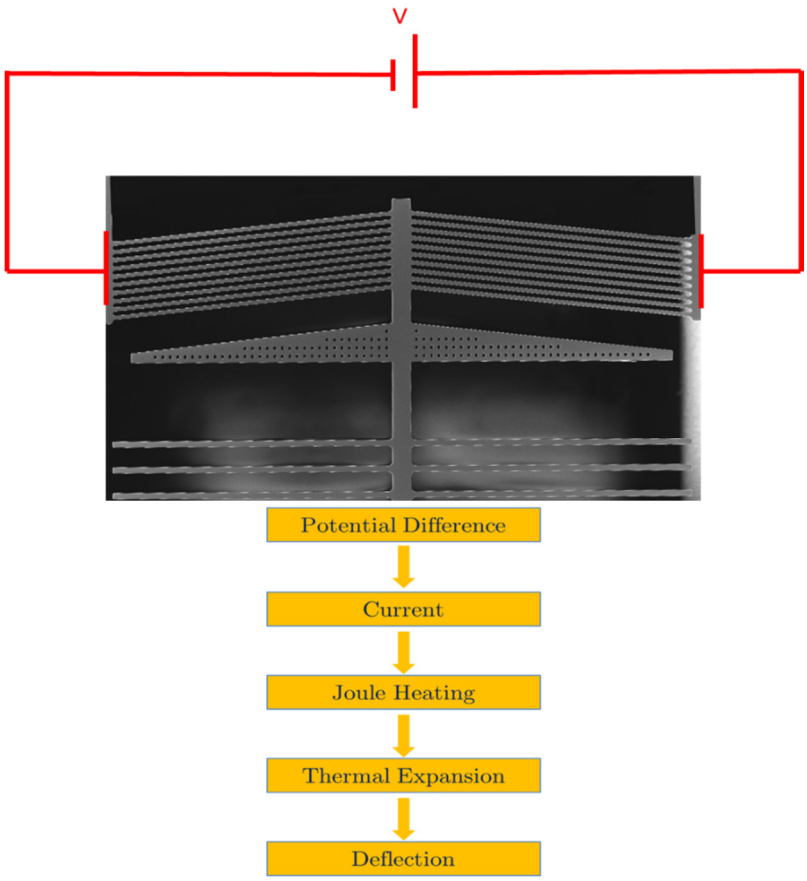

Figure 2.3 SEM micrograph of the actuator with flow chart of the principle of operation

2.1.2.3 Capacitive Sensors

The first capacitive sensor, CS_1, is rigidly connected by a non-conductive UV-curable glue to the thermal actuator (i.e., $X_{CS1} = X_A$), while electrically isolated from it, and consists of 21 pairs of "combs" on each side of the MEMS device's symmetry axis. During a tensile testing on a specimen, the deflection of the thermal actuator along the long axis of the MEMS device causes a reduction in the gap between these combs. In the absence of a specimen (or after failure of the specimen), the output signal of the MEMS corresponds to the change in capacitance of CS_1 (ΔC_1) which can be directly related to X_A using the parallel plate capacitance

formula (for more details see section 2.1.5.2). The second capacitive sensor, CS_2, is rigidly connected to the load sensor ($X_{CS2} = X_{LS}$), and is identical to CS_1 (see Figure 2.2 (b)). ΔC_1-ΔC_2 is then measured and used to determine the applied force and specimen elongation.

2.1.2.4 Load Sensor

The role of the load sensor beams are to measure the applied force on the specimen under tensile load. The force applied on the sample is determined by the deflection of the load sensor with a known stiffness. The load sensor is made of four beams (length: 500 μm), deforming in bending mode as shown in Figure 2.2 (b). The stiffness of the load sensor, K_{LS}, can be accurately calculated given the known properties of monocrystalline Si. The width of the beam mainly dictates K_{LS} that ranges from 100 N/m (width: 12.5 μm) to 480 N/m (width: 21 μm; see section 2.1.5.1.1 for details).

2.1.2.5 Specimen Gap

The specimen gap is about 5 μm, and consists of two adjacent large areas (50 μm by 200 μm) for proper clamping of the specimen onto the MEMS device. (see Figure 2.2)

2.1.3 MEMS Fabrication Process

Figure 2.4 shows an overview of the SOIMUMPs fabrication process used for the MEMS device [145]. Briefly, an n-type silicon-on-insulator (SOI) wafer is first surface doped; see Figure 2.4(a). Then a metallic layer is deposited and patterned

onto the SOI wafer (Figure 2.4(c)), which is followed by the patterning of the Si layer using a deep reactive ion etching process; see Figure 2.4(d). A front side protective material is applied before the back of the wafer is patterned to provide through-hole structures, an essential aspect of these MEMS devices for *in situ* TEM purposes; see Figure 2.4(e). The front side protection layer is then removed, as well as the exposed oxide layer from the top surface; see Figure 2.4(f).

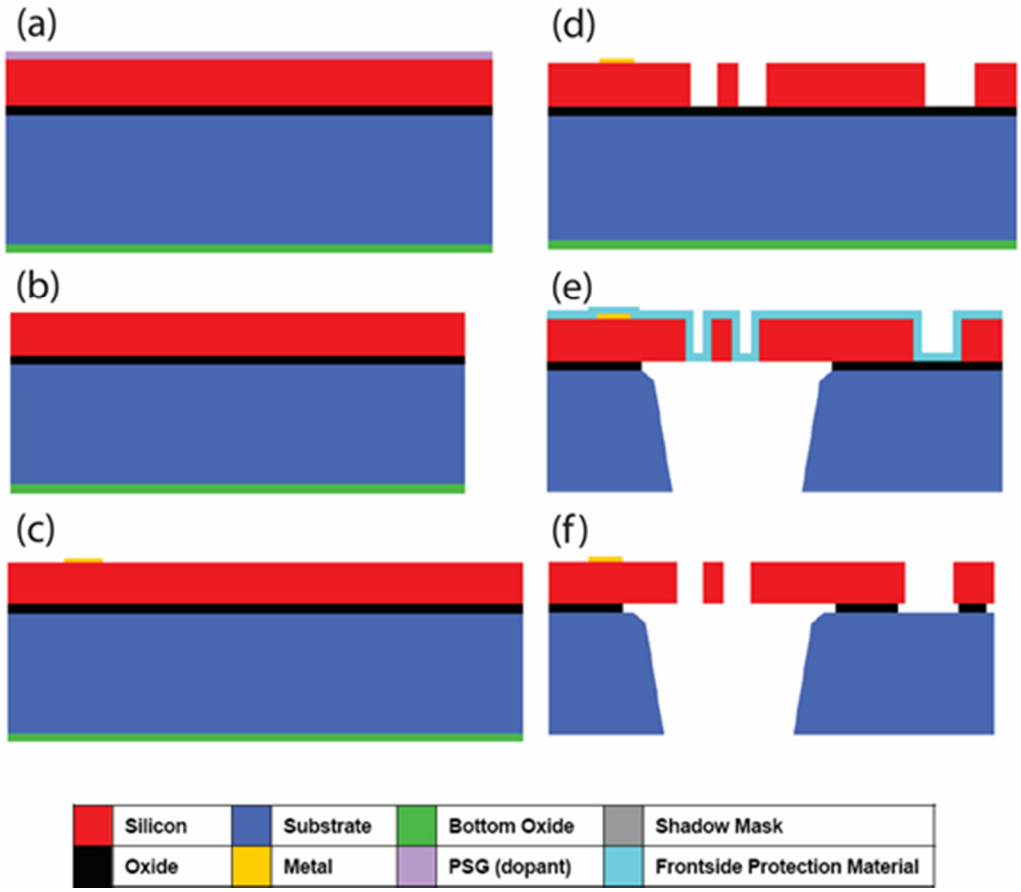

Figure 2.4 SOIMUMPs fabrication process [145]. See text for details.

2.1.4 Experimental Setup

This section explains different segments of the experimental setup of sensing electronics for *in situ* and *ex situ* setups.

2.1.4.1 Sensing Electronics

The capacitance change $\Delta C_1 - \Delta C_2$ (or ΔC_1 in the absence of a specimen) is measured using a universal capacitive readout sensor (MS 3110, Irvine Sensor). The MS 3110 works in differential mode (see Figure 2.5). It senses the capacitance change between two capacitors resulting in an output proportional to the capacitance change $\Delta C_1 - \Delta C_2$. If one of these capacitances is known, the capacitance change for the other capacitor could be calculated.

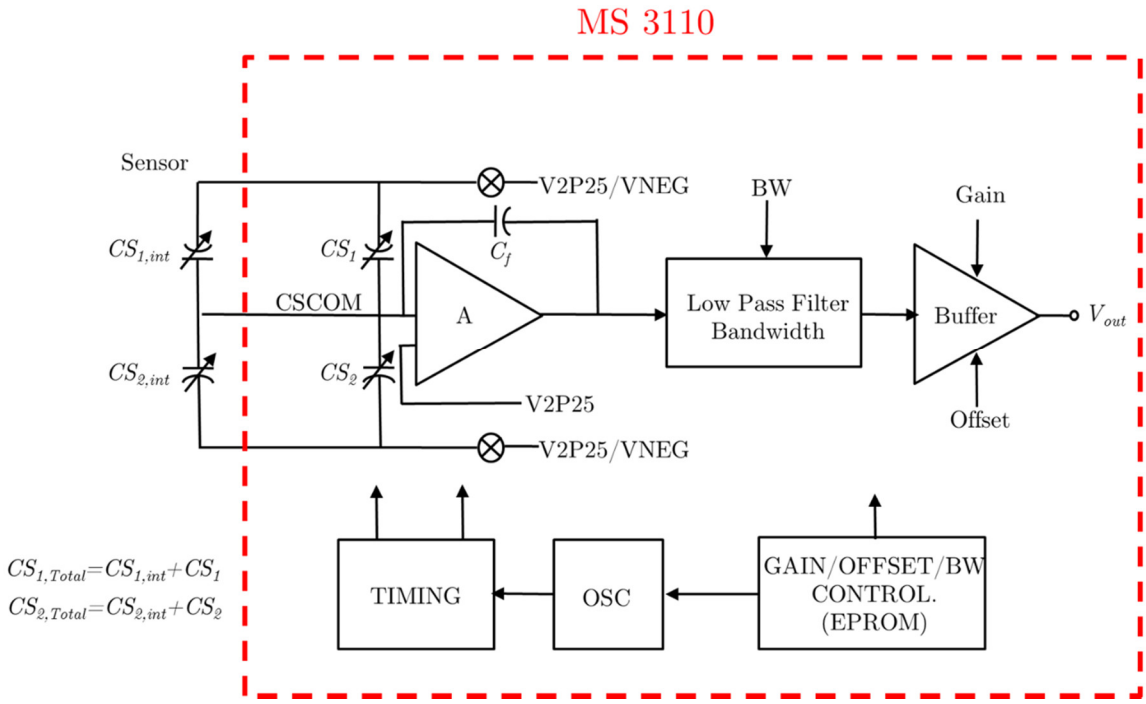

Figure 2.5 MS 3110 functional diagram (with V2P25=2.25 V, VNEG=0, V_0 is the output voltage, C_f is the feedback capacitance). V_{out} is the output which is linealry proportional to $\Delta C_1 - \Delta C_2$

The output voltage V_0 (in Volt) is related to the change in capacitance via the following equation:

$$V_0 = 5.13 \times \frac{C_2 - C_1 + C_{2,int} - C_{1,int}}{C_f} + 2.25 \qquad (2\text{-}1)$$

Where C_f is the feedback capacitor (C_f = 399 fF), $C_{1,int}$ and $C_{2,int}$ are pre-programmed internal capacitances (in fF). During a test, the driving voltage V_{in} is applied in incremental steps and the corresponding V_0 is averaged after measurement durations ranging from 500 ms to 2 s at an acquisition rate of 1 KHz (for noise reduction). The capacitance change is therefore given by:

$$\Delta C_1 - \Delta C_2 = C_f \times \frac{\bar{V}_0(V_{in}=0) - \bar{V}_0(V_{in})}{5.13} \qquad (2\text{-}2)$$

Where $\bar{V}_0$ represents the average V_0 over the acquisition period.

2.1.4.2 *Ex situ* Setup

An Agilent 6708 power source was used to give the required voltage to the actuator. Contact pads of the MEMS device were wire bonded to the IC package which was then connected to the driving source and the sensing circuit as shown in Figure 2.6. The output voltage was transferred with a BNC cable to one of the channels of NI SCXI-1305 block, mounted in a slot of an NI SCXI-1000 chassis to have communication with a desktop computer. LabVIEW interface was used to control the driving voltage and to capture the output signal from the circuit.

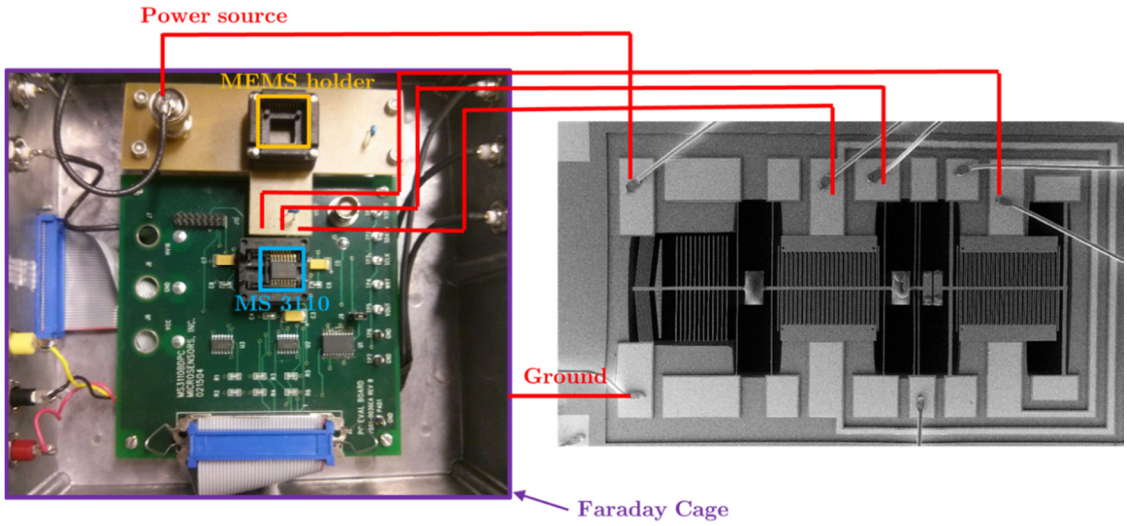

Figure 2.6 An illustration of *ex situ* experimental setup (capacitive sensing circuit). The setup is enclosed in a Faraday cage for noise reduction. The red wires connect the device pads to thermal actuator, CS1, CS2 and CSCOM respectively of MS3110.

2.1.4.3 *In situ* Setup

A similar setup was used to perform the experiments inside a transmission electron microscope (TEM). An Agilent 3649a power source was used to give the required voltage to the actuator. All *in situ* experiments were carried out inside a HF 2000 TEM (acceleration voltage: 150 kV) or JEOL 2010 (acceleration voltage: 200 kV). MEMS devices are designed such that they can be directly mounted on a specially designed TEM holder (Hummingbird) with 6 leads which contains a feed-through and interconnects as shown in Figure 2.7. They illustrate the MEMS device which is small enough, ~1 mm by 3 mm, to fit inside an electrical basing holder. This Hummingbird TEM holder allows positioning of MEMS inside the microscope. It also provides electrical addressing for actuation and sensing. The sensing integrated circuit chip (MS 3110) is located outside of the microscope. In the quantitative *in situ* TEM experiments, the MEMS device provides stress and strain

measurements via electrical signals, while TEM imaging provides information on the microstructure evolution during testing.

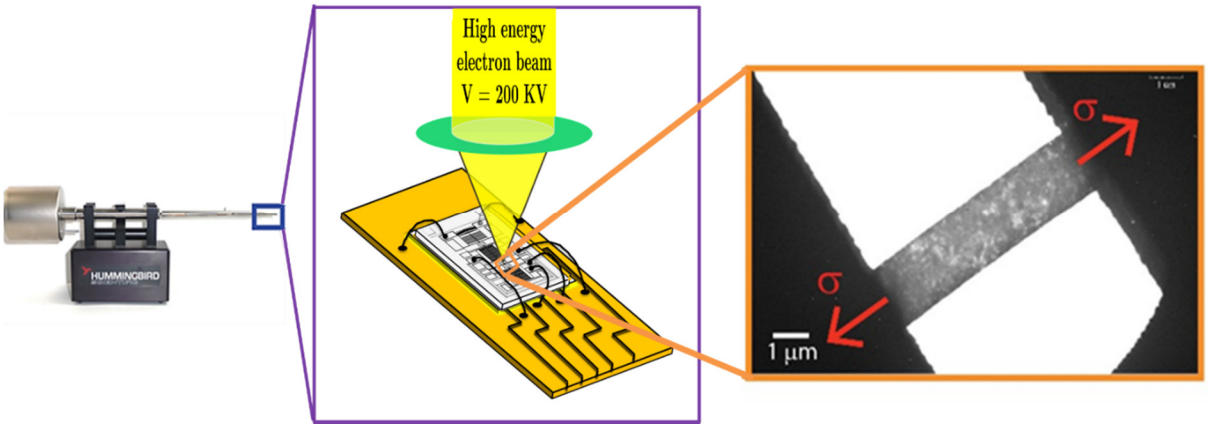

Figure 2.7 Hummingbird electrical biasing holder with 6 leads for which a wirebonded MEMS device can be fit into. Schematic of specimen carrier with a mounted MEMS in the trench for *in situ* experiment. There are 6 electrical leads in the specimen carrier for wirebonding to apply and meausre electrical signals.

2.1.5 MEMS Characterization

To determine the displacements of the thermal actuator and load sensor, and consequently applied force and specimen elongation, a relationship between capacitance change and displacement has to be established. Similarly, the displacement of the thermal actuator (X_A) as a function of voltage is also required. Hence, accurate characterization of capacitance sensing and actuator displacement is necessary to accurately calculate stress and strain.

2.1.5.1 Actuator Characterization

Thermal actuator has already been thoroughly modeled numerically to determine X_A [144, 146]. However, the response of thermal actuator at different environmental conditions is missing. In section 2.1.5.1.1, a three dimensional finite

element model was performed to study the response of the thermal actuator to electric potential in different environmental conditions. Specifically, a coupled electrical-thermal-structural analysis was performed to determine the stiffness of the actuator and its displacement X_A as a function of applied driving voltage in different ambient temperatures and compare. In section 2.1.5.1.2 the numerical results directly compared to experimental measurement of displacement X_A.

2.1.5.1.1 Finite Element Analysis

The actuator made of a 10 μm thick doped single crystal silicon beams. Surface doping brings a gradient in resistivity along the depth of the device. To consider this, the silicon structural layer was modeled as a bimorph. The layer at the bottom was assumed to be n-type silicon layer with a resistivity of 10 Ohm-cm [146]. The top layer was assumed to be highly doped silicon and the resistivity of the layer for a particular layer thickness was calculated based on the total resistance measured experimentally (typical value for actuator resistance is about 100 Ω) [146]. The 500 μm thick air cushion between the device and the substrate was modeled to account for conductive heat transfer through the air to the substrate below and from the device to the air. Due to symmetry in geometric boundary conditions only half the actuator was modeled to decrease the computational time.

Air/Substrate:

The air has major heat conduction though air to the substrate below. Thus the air block modeled below the region near the actuator to a depth of 500 μm (substrate). The substrate is assumed to be at room temperature.

Material Properties:

There were three material properties in the simulations: the top silicon layer, the non-doped silicon layer at the bottom and the surrounding air. Each of these materials had a corresponding resistivity, thermal conduction, stiffness matrix, and thermal conductivity as seen in Table 2.1. Below is the stiffness matrix for silicon in Table 2.2. The device is oriented along the <110> direction on (100) plane, the local coordinates for the two single crystal silicon layers were defined at 45° to global coordinates as anisotropic materials [146].

Table 2.1 Material properties of intrinsic and doped Silicon and air

Material	Resistivity	Thermal Conductivity	Coefficient of Thermal Expansion	Other Properties
Doped silicon	16 Ohms-micron	150 W/mK	$\alpha(T)$	
Silicon	10-6 ohms-micron	150 W/mK		
Air	0	0.03 W/mK	0	Ex, PRXY = 0
Modal Si				ρ= 2329 Kg/m^3

Table 2.2 Stiffness matrix for Silicon with values in GPa

$$\begin{bmatrix} 166 & 64 & 64 & 0 & 0 & 0 \\ 64 & 166 & 64 & 0 & 0 & 0 \\ 64 & 64 & 166 & 0 & 0 & 0 \\ 0 & 0 & 0 & 80 & 0 & 0 \\ 0 & 0 & 0 & 0 & 80 & 0 \\ 0 & 0 & 0 & 0 & 0 & 80 \end{bmatrix}$$

The coefficient of linear thermal expansion and thermal conductivity of silicon shows a temperature dependent behavior which was included in the model[1].

Element Type:

SOLID 227 is used for modelling the coupled multi-physics problem.

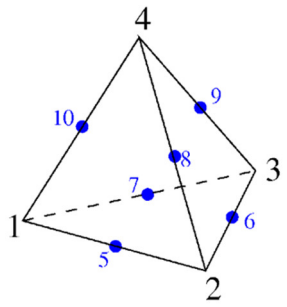

Figure 2.8 node tetrahedral element

Boundary and Load Conditions:

Analysis of a thermal actuator requires a coupled electric, thermal and mechanical investigation. The mechanical behavior of the device is numerically derived on the basis of small strains and negligible shear deformation of the beams, i.e. an in nite shear stiffness is assumed. Boundary conditions are essential for the

[1] The value of the linear thermal expansion coefficient $\alpha(T)$ is given by the following expression: $\alpha(T) = \left(3.725\left[1 - e^{-5.88\times10^{-3}(T-124)}\right] + 5.548\times10^{-3}T\right)\times10^{-3}K^{-1}$

three existing domains: electrical, thermal, and mechanical. For the electrical domain, the voltage was set to be $V_{actuation}/2$ on the actuator pad. At the symmetrical plane in the middle, the deflection is vertical, while the voltage was taken to be zero in that plane. For the thermal domain, it was assumed that the temperature on the anchor was set at room temperature (300˚K) along with the lower face of the modeled air block and infinity. Finally all the displacements were set to zero on the actuator anchors.

Meshing:

For each structure, a convergence mesh was found. Below in Figure 2.9, the analysis of mesh for thermal and deflection solution is shown. The mesh view in Figure 2.9 includes the air/substrate block. Mesh convergence results for each type of analysis in Figure 2.10 and Figure 2.11.

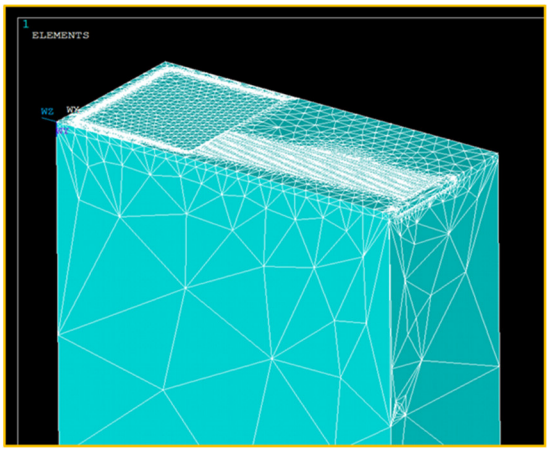

Figure 2.9 Meshing of the actuator including the air, surrounding the device

Mesh convergence analyses were performed on the vertical maximum deflection and maximum temperature achieved by the actuator as shown in Figure 2.10 and Figure 2.11.

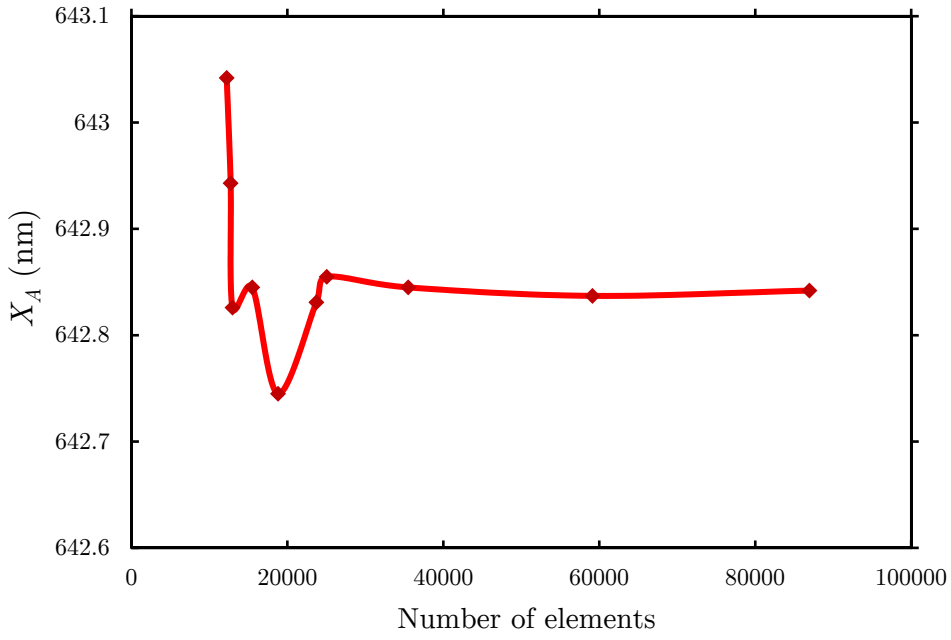

Figure 2.10 Mesh convergence for deflection at $V_{in} = 3$ volt.

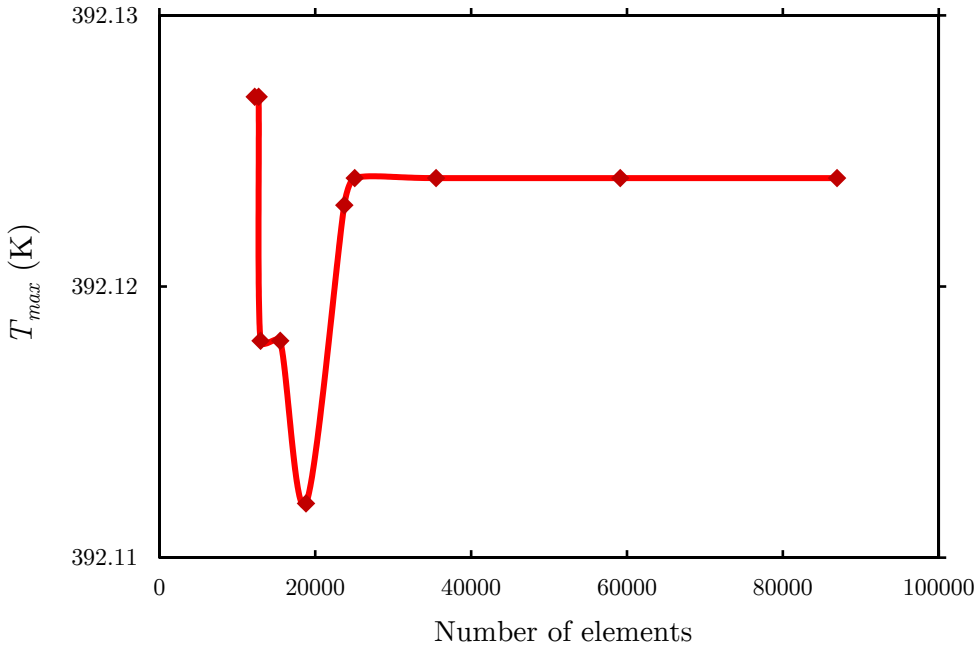

Figure 2.11 Mesh Convergence for Temperature at $V_{in} = 3$ volt

Both plots clearly show the convergence after application of 3000 elements. Accordingly, Figure 2.12 presents the response of the thermal actuator without the

heat sink in vacuum, approximating the experimental condition inside transmission electron microscope. Based on the contours in Figure 2.12, X_A at $V_{in} = 3$ V is ~640 nm. Moreover, stress distribution along the beams have a maximum stress of about 28 MPa. This ensures that the device operates in low-stress elastic regime which is crucial to ensure that the device does not go under plastic deformation.

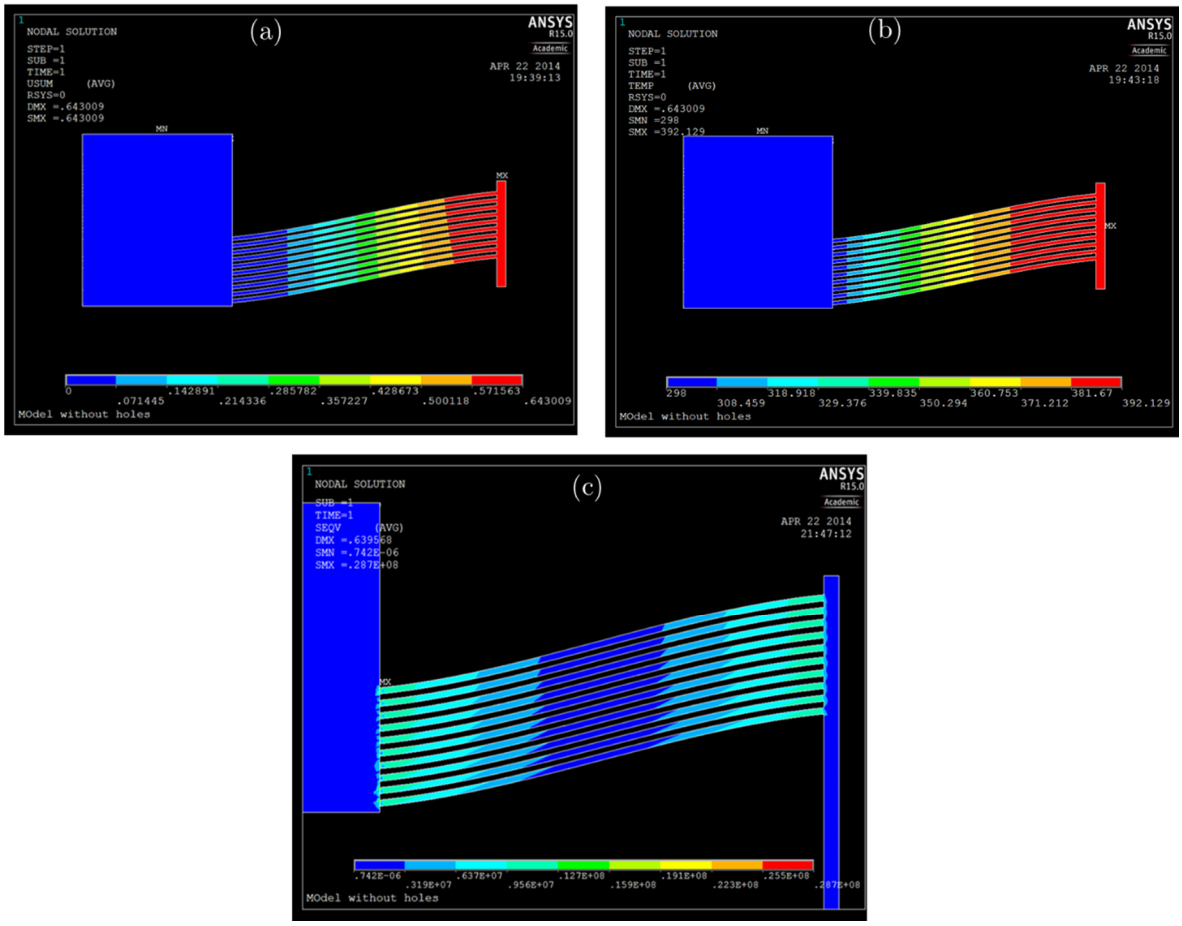

Figure 2.12 (a) Deflection contour in micrometer, (b) Temperature distribution (c) Stress distribution in Pascal (No heatsink-vacuum condition) when $V_{in} = 3$ volt.

The temperature dependence of MEMS response operating at different temperatures of the surrounding environment was also analyzed. This analysis could be useful to understand the response of MEMS-based experimental setup for high temperature nanotensile testing. Figure 2.13 (a)-(c) demonstrates the temperature

distribution in the surrounding air and across the thermal actuator for T_∞ = 298, 398 and 698 K, respectively. Defining $T'' = T(x,y,z) - T_\infty$ and careful analysis of Figure 2.13 (a)-(c) show that $T''(x,y,z)$ is independent of the temperature of the environment. This results in a constant offset in deflection vs voltage curve in case of modest increase in T_∞. This may not be true for very high temperatures as the doped Si properties could drastically change.

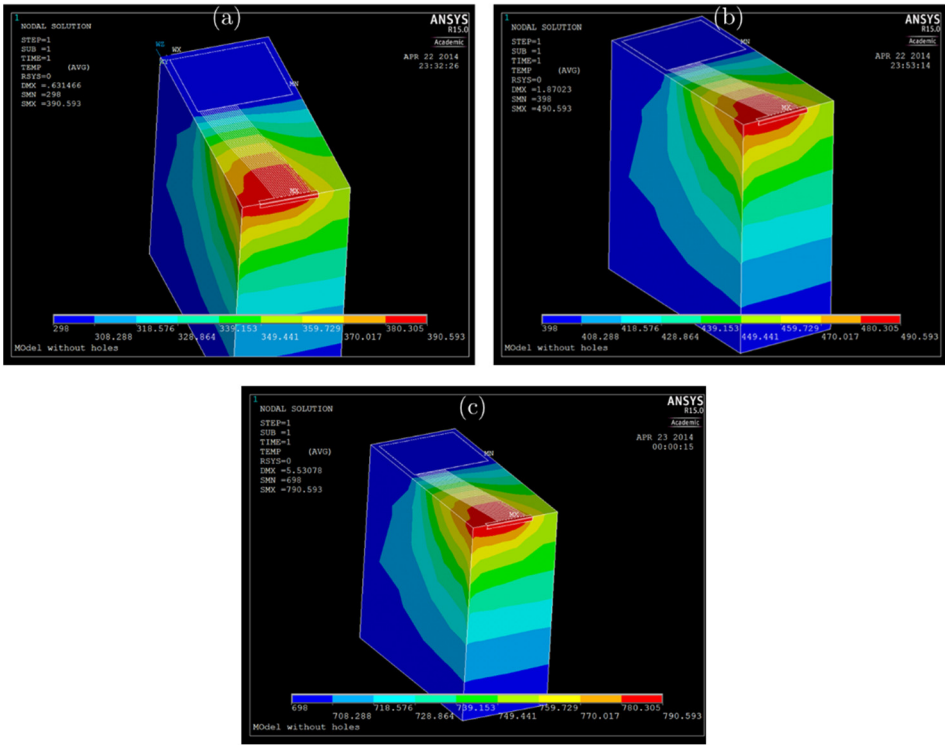

Figure 2.13 Temperature distribution with the surrounding air at 298 *K*, (b) 398 K and (c) 698 K

The thermal actuator stiffness, K_A, could be analytically approximated as [44]:

$$K_A = 20\left(\sin^2\theta + \frac{\cos^2\theta}{\psi}\right)\frac{EA}{l} \qquad (2\text{-}3)$$

Where

$$\psi = \frac{Al^2}{12I} = \frac{l^2}{b^2 + h^2} \tag{2-4}$$

with θ as the beam angle, A the cross-sectional area, E the elastic modulus, l the length of the beams, I the moment of inertia of the cross-section with respect to the out-of-plane axis, h the beam thickness and b as the beam width [44]. Plugging elastic modulus of Si in (110) direction and nominal dimensions of the thermal actuator gives actuator stiffness K_A of ~3975 N/m. However, plugging the actual geometrical dimensions, measured by SEM images, resulted in K_A of ~ 3620 N/m. The difference in nominal and actual dimensions of the device is due to the fabrication process of the MEMS.

As an alternative approach, K_A could also be numerically calculated. In this regard, 1 Newton of force was applied to the plane of symmetry and the deflection X_A has been calculated. Figure 2.14 (a) shows the force vector in the symmetric plane and the applied boundary conditions in the model while Figure 2.14 (b) demonstrates the resulting solution with contour of deflection.

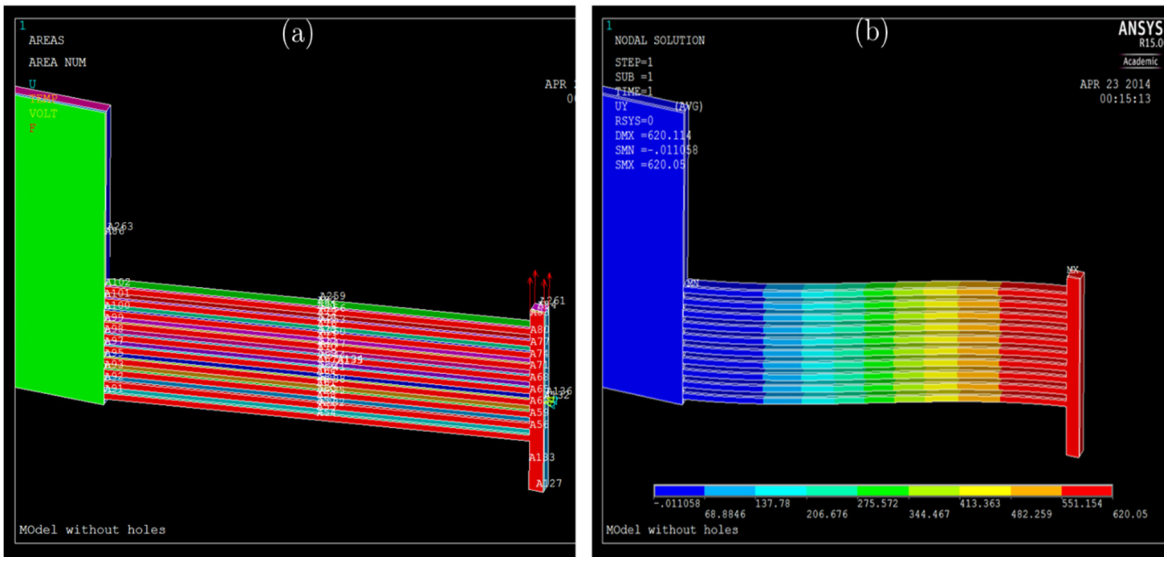

Figure 2.14 (a) Application of 1 N to measure the displacement and subsequently, stiffness of the thermal actuator in vacuum(b) Corresponding deflection contour

This approach gives a stiffness of 3226 N/m (accounting for the device geometry) which is within ~20 % of analytical data with the nominal dimensions of the actuator. While 20 % shows a good correlation of calculated K_A between the two methods, a portion of the difference in the results could be associated with the anisotropic properties of monocrystalline Si compared to the simplified elastic modulus, assumed in the analytical model. Both models also ignore the temperature dependence of elastic modulus of Si that could lead to errors in calculations of displacement. In addition, analytical model assumes a superposition of uniaxial stress state and Euler-beam theories and ignores the involved shear stress while numerical simulation calculates the deflection by splitting the actuator beams into thousands of elements and solve a three dimensional stress state.

2.1.5.1.2 Experimental Analysis

The actuator deflections for various applied driving voltages were characterized by measuring the change in the gap of comb structures as shown in Figure 2.16. Both optical and electron images (TEM) could be used for measuring the change in the gap distance. For the optical images, diffraction acts as the limiting factor in the accuracy of displacement measurements since spatial resolution is on the order of the wavelength of the used light. However, electron microscopy images does not have the diffraction issue given its much smaller wavelength, and hence much better resolution and smaller error bars (20 nm for deflection). Figure 2.15 compares the calculated X_A as a function of driving voltage using direct experimental measurements and numerical simulation, presented earlier in section 2.1.5.1.1. Note that the heatsink has negligible effect on X_A in vacuum and hence it is removed from the model to reduce the required time for numerical computation. The plot shows a reasonable agreement between the experimental and numerical results as shown in Figure 2.15. The difference in the results could be associated with the simplified bimorph-model for material properties of doped Si in numerical analysis as in reality there is a gradient of dopant concentration through the thickness. In addition, numerical simulation assumes a linear material response in thermomechanical domain and ignores the effect of material nonlinearities.

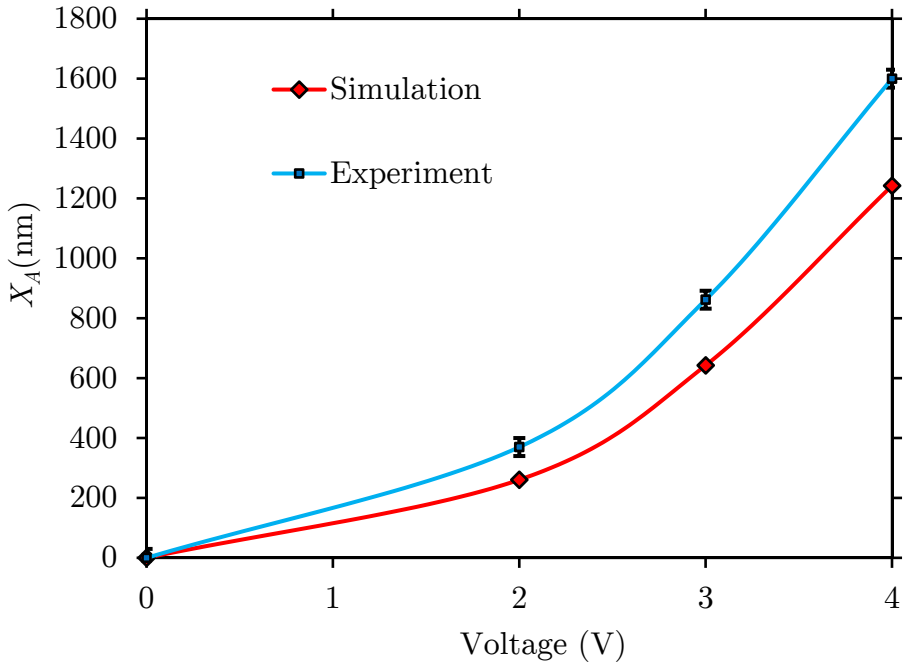

Figure 2.15 Deflection of thermal actuator (without heatsink) versus applied voltage in vacuum; comparison between experimental and FE analysis.

The calculated X_A from FEM analysis is lower than the similar previous simulations and the experimental results [144, 146]. This could be explained as in the current FEM study, the perforated section of the heatsink was neglected to reduce the required time for numerical computation. Another explanation could be due to the modelling of doped silicon beams as bimorph layers and thereby underestimating the actual resistivity (and so lower deflections and temperature.). In addition, FEM analysis assumes a constant resistivity for silicon beams but in reality the doping profile could vary with temperature and time.

2.1.5.2 Capacitive Sensing and Characterization

The displacements of capacitive sensors CS_1 and CS_2 are related to a change in capacitance, ΔC, based on the following parallel plate capacitance formula:

$$\Delta C = \alpha \varepsilon_0 n k \left(\frac{1}{d_1 - X} + \frac{1}{d_2 + X} \right) \tag{2-5}$$

where α is a calibration constant, $\varepsilon_0 = 8.854 \times 10^{-12}$ F/m is the permittivity of free space, k is the relative permittivity of the dielectric material ($k \sim 1$ for air), A is the overlapping area of a comb structure, n is the number of comb structures, d_1 and d_2 are the initial gaps between the comb structure ($d_1 = 4$ μm, $d_2 = 9$ μm; see Figure 2.2 (a)), and X is the displacement of CS_1 (X_{CS1}) or CS_2 (X_{CS2}). The precision in capacitance measurements is better than 0.1-0.2 fF, which corresponds to a precision in displacement of approximately 1-5 nm (see section 2.1.6.5). This level of precision can be used to measure the mechanical properties of nanospecimens without requiring high magnification images. However, the accuracy of the displacement calculation relies on the accuracy of the simplified Eq. (2-5) which, for example, ignores the fringing field effects. More importantly, parasitic capacitance can affect the measurements given the very low ΔC values (fF level). Hence a calibration is performed for each MEMS device and consists of accurately measuring the displacement of CS_1 for large values (~ 1.6 μm, corresponding to $V_{in} = 4$ V) based on high magnification images (either optical for *ex situ* tests, or electron images for *in situ* SEM or TEM tests). The procedure to measure displacement with pixel accuracy was explained in section 2.1.5.3. The ratio between the measured displacement at 4 V and the calculated displacement at 4 V using Eq.(2-5)(assuming $\alpha = 1$) is used as the calibration constant, α.

2.1.5.3 *In situ* TEM MEMS Calibration

As explained in section 2.1.2.3 and 2.1.5.2, each MEMS device is calibrated to ensure accurate measurements of the various MEMS components' displacement (X_A, X_S, X_{LS}). The parallel plate capacitance formula (see Eq.(2-5)) is calibrated by measuring actual displacement of the capacitive sensor 1 (CS_1) at $V_{in} = 4$ V using either optical or electron images. Figure 2.16 shows a selection of the bright field TEM images that were used to measure the displacements of the thermal actuator (based on the displacement of the capacitive sensor 1, since $X_A = X_{CS1}$; see Figure 2.16 (a)) and the load sensor (based on the displacement of the capacitive sensor 2, X_{LS}; see Figure 2.16 (b)) for selected V_{in} values. The dark areas correspond to the beams of the MEMS device (see Figure 2.2), while the bright areas correspond to the gaps between the beams (through-hole MEMS device). The displacements are measured by comparing the images at a given V_{in} to the reference image at $V_{in} = 0$ V, using a MATLAB routine. Specifically, the TEM images were overlapped to their reference images ($V_{in} = 0$ V), and the relative displacement was measured with an approximate precision of 40 nm for Figure 2.16 (a) and (b).

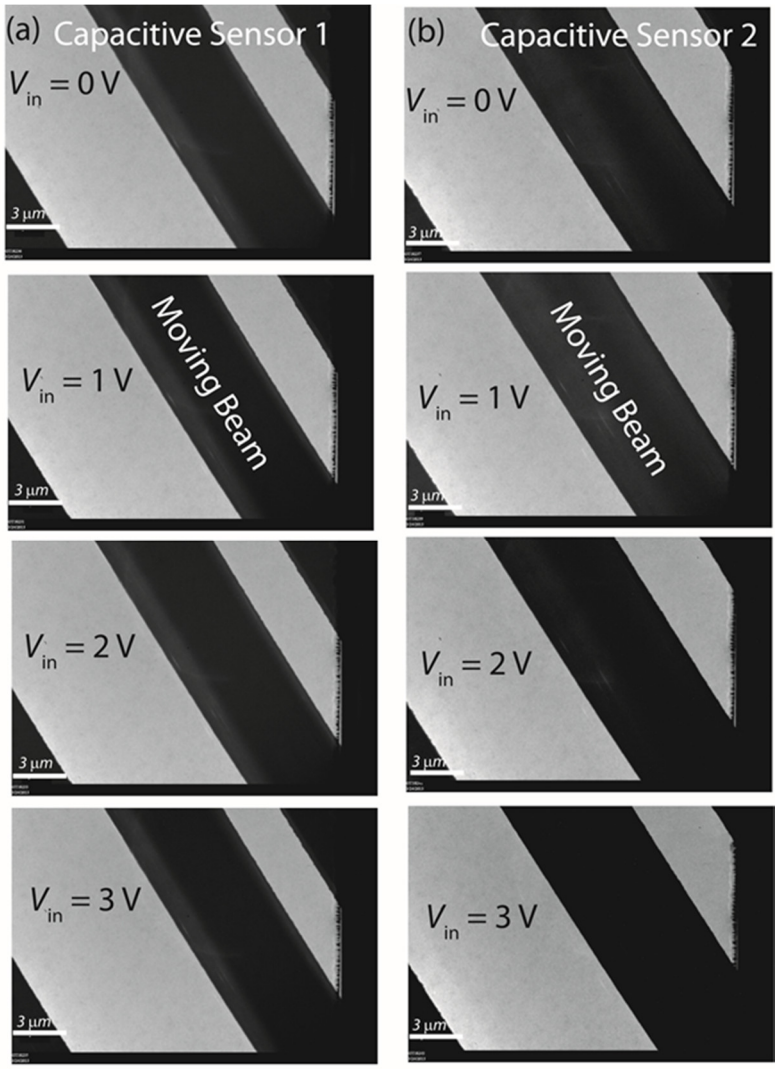

Figure 2.16 (a) Series of TEM images of capacitive sensor *1* during a fatigue test, at four different V_{in} values (0, 1, 2, and 3 V). (b) Series of TEM images of capacitive sensor 2 during the same fatigue test, at four different V_{in} values (0, 1, 2, and 3 V).

Figure 2.17 (a)-(c) shows excellent agreement, for 3 different MEMS devices without any specimen, between the calculated X_A values based on electrical measurements and Eq.(2-5), and the measured X_A values at lower V_{in} values, using also either optical or electron images.

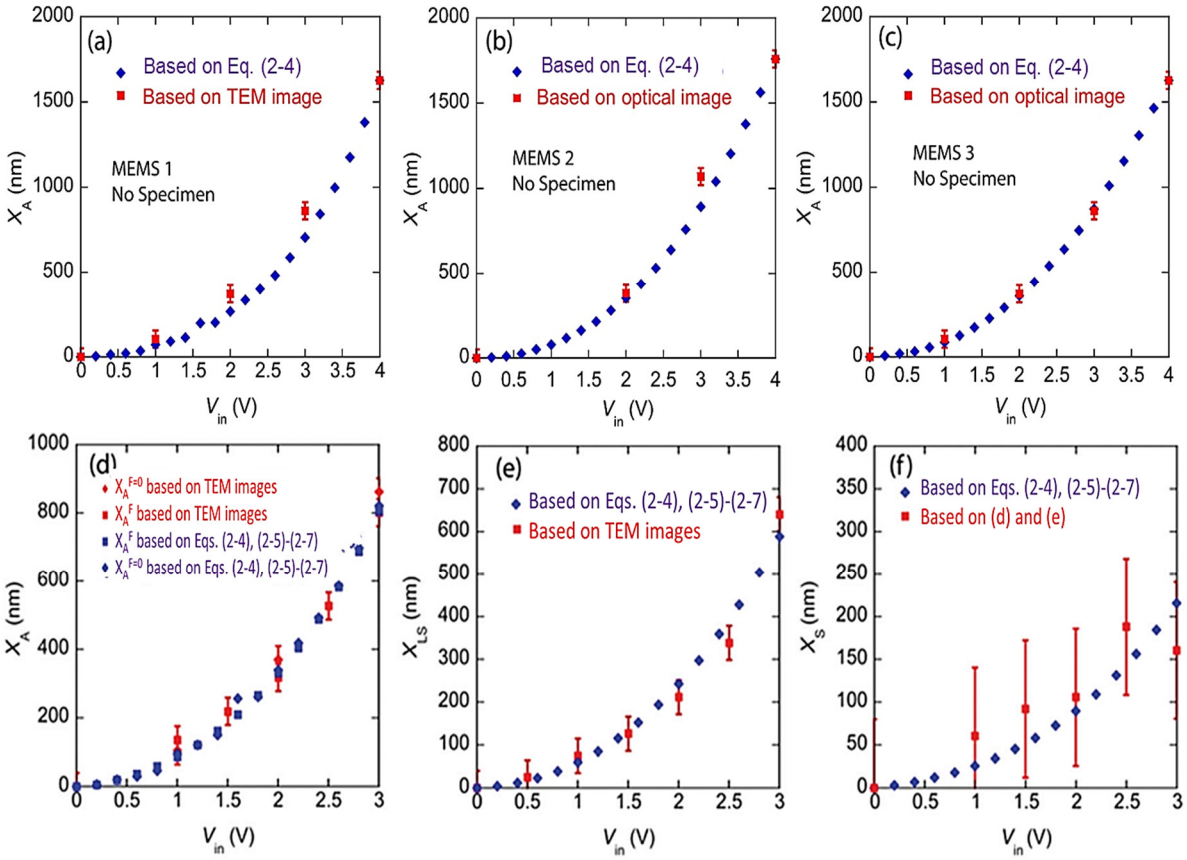

Figure 2.17 (a)-(c) Comparison of the calculated (based on electrical measurements) and measured (based on TEM or optical images) displacement of the thermal actuator for three different MEMS devices without a specimen. (d) Comparison of the calculated and measured thermal actuator displacement for an *in situ* TEM test with a specimen, along with the same data without a specimen. (e) Comparison of the calculated and measured load sensor displacement for the same *in situ* TEM test as (d). (f) Comparison of the calculated and measured specimen elongation for the same *in situ* TEM test as (d)-(e).

Figure 2.17 (d)-(f) also show excellent agreement between the calculated X_A, X_{LS} and X_S values for an actual *in situ* TEM test of an NC Au specimen based on electrical measurements and Eqs. (2-5), (2-6)-(2-8) and the measured values based on TEM images. In addition to providing accurate measurements, this experimental setup is also very precise with a noise floor in the electrical signal of about 0.1-0.2 fF (see section 2.1.6.5), which corresponds to 1-5 nm in displacement depending on the actual deformation of the capacitive sensors (see Eq.(2-5)).

2.1.6 Quantification of Mechanical Properties

As explained in section 2.1.4.1 the sensing circuit measures the capacitance change $\Delta C_1 - \Delta C_2$ as a function of V_{in}. Hence, a procedure is required to calculate mechanical properties such as stress, strain and plastic strain rate from the capacitance changes which is presented in this section.

2.1.6.1 Calculation of Stress and Strain

The force F applied onto the specimen (and therefore the applied stress, knowing the specimen cross-sectional area) can be calculated if the load sensor displacement, X_{LS} is known, using:

$$F = K_{LS} \times X_{LS} \tag{2-6}$$

During a test, the difference in capacitance between CS_1 and CS_2, ΔC_1-ΔC_2, is measured with a MS3110 chip (Irvine Sensor) (see section 2.1.4.1), which is related to the elongation of the specimen, X_S. The stress and strain of the specimen can be calculated if both X_{LS} and X_S and specimen dimensions, measured accurately with SEM/TEM, are known with the assumption that the clamps do not deform (see section 2.3.1). Therefore, two independent sets of measurements are required to calculate the stress-strain curve: ΔC_1-ΔC_2, vs V_{in} (measured during the test) and ΔC_1 vs V_{in} (measured after the specimen is broken or before it is fixed onto the MEMS). The former essentially gives X_S and the latter gives X_A, from which X_{LS} can be calculated using:

$$X_A = X_S + X_{LS} \tag{2-7}$$

However, for a given V_{in}, the thermal actuator displacement without a specimen (i.e., no applied force F onto the actuator), $X_A^{F=0}$ is different from the displacement with a deformed specimen (i.e., a force F is applied onto the actuator), X_A^F. Both quantities can be related via the following equation [44]:

$$\frac{X_A^F}{X_A^{F=0}} = \frac{1}{1+\frac{K_{LS}}{K_S}+\frac{K_{LS}}{K_A}} + \frac{1}{1+\frac{K_S}{K_{LS}}+\frac{K_S}{K_A}} \tag{2-8}$$

Where K_S is the stiffness of the specimen, and K_A is the thermal actuator stiffness (K_A of ~3975 N/m has been used which is calculated based upon nominal dimensions. The ratio of $\frac{X_A^F}{X_A^{F=0}}$ would change negligibly if the actual dimensions were used; For details see section 2.1.5.1.1). This equation can be used to predict X_A^F based on the calculated $X_A^{F=0}$ from the measured ΔC_1 vs V_{in}. Once X_A^F is known, both X_S and X_{LS} can be calculated based on the measured ΔC_1-ΔC_2 vs V_{in}. Eq.(2-8) requires knowledge of K_S, which depends on the specimen's elastic modulus E ($K_S = EA/L$, with A and L cross-section area and length of the specimen, respectively) and is typically unknown. In that case, an iterative procedure based on the calculated E value is used to calculate stress and strain.

2.1.6.2 Image-based Stress and Strain Calculations

For a portion of the tensile tests the electronic sensing was not operational during the *in situ* TEM experiments, performed inside JEOL microscope. Hence an indirect approach was used to estimate stress and strain. Figure 2.18 (a) shows a selection of bright field TEM images that were used to measure the displacements

of the load sensor (based on the displacement of the capacitive sensor 2) for selected V_{in} values. The displacements are measured by comparing the images at a given V_{in} to the reference image at $V_{in} = 0$ V. The features of interest were a fixed comb, an adjacent moving comb of CS_2, and the gap in between. A MATLAB routine was created to measure the gaps from these images, from which the displacement of load sensor (X_{LS}) can be obtained. In addition, the specimen elongation (X_S) was directly measured using bright field TEM images of the gauge section at magnifications of 10 or 12 K, with a resolution of ~30 nm (see Figure 2.18 (b)).

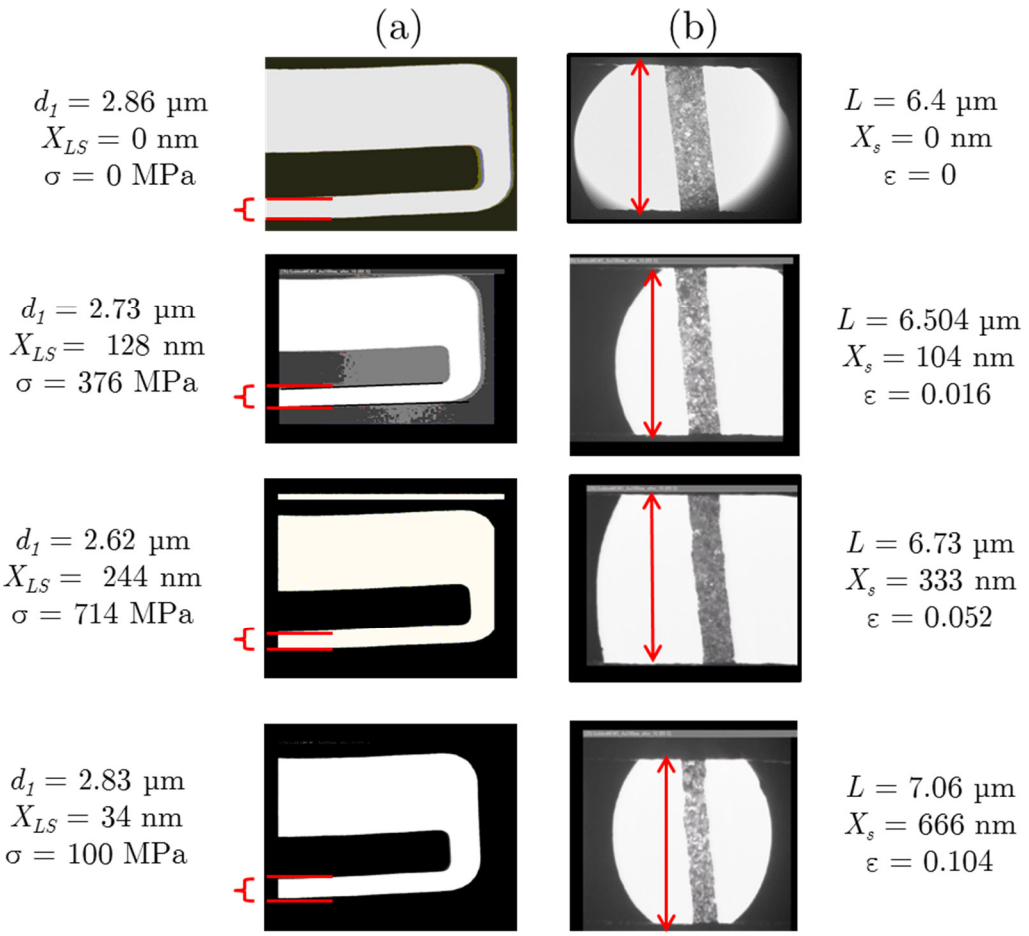

Figure 2.18 (a) Series of TEM images of capacitive sensor 2 during a relaxation test (see chapter 4), at four different V_{in} values (0, 1.8, 2, and 2.4 V), to measure stress. (b) Corresponding TEM images of gauge length to measure strain.

2.1.6.3 Calculation of Fatigue Properties

Fatigue properties are calculated similarly to the monotonic properties. An iterative procedure is used based on the calculated E value from the unloading of the very first cycle to calculate stress and strain in each cycle. This procedure has been intentionally applied to reduce the computational time, required to calculate stress, total strain and plastic strain for each cycle.

2.1.6.4 Calculation of Relaxation Properties

Relaxation experiments consist of keeping V_{in} constant, and measuring the specimen's answer over time. Under these conditions, the displacement of the thermal actuator (X_A) is constant, and is equal to the specimen's plastic elongation ($X_{S,pl}$) plus the elastic deformation of the specimen / load sensor assembly ($X_{S,el} + X_{LS}$). The elastic term is equal to the applied force (F) divided by the equivalent stiffness (K_{eq}) of the specimen (cross section area A, length L) / load sensor assembly (of modulus M). Hence, we have:

$$X_A = X_S + X_{LS} = X_{S,pl} + X_{S,el} + X_{LS} = X_{S,pl} + \frac{F}{K_S} + \frac{F}{K_{LS}} = X_{S,pl} + \frac{F}{K_{eq}} \tag{2-9}$$

With:

$$K_{eq} = \frac{K_S K_{LS}}{K_S + K_{LS}} = \frac{MA}{L} \tag{2-10}$$

The viscoplastic deformation of the specimen results in an increase in plastic strain ($\Delta\varepsilon_{pl}$) which is accompanied by a stress relaxation ($\Delta\sigma$) [147]:

$$\Delta X_A = 0 = \Delta X_{S,pl} + \frac{\Delta F}{K_{eq}} = \Delta\varepsilon_{pl} L + \frac{\Delta\sigma A}{K_{eq}} \Rightarrow \Delta\varepsilon_{pl} = \frac{-\Delta\sigma}{M} \tag{2-11}$$

Both quantities (ε_{pl} and σ) are independently measured over time, from which plastic strain rates can be calculated as a function of applied stress during relaxation. The following procedure has been used to plot plastic strain rate versus stress and n versus time:

First, a logarithmic function of the form $a\, ln(1+\frac{t}{c})$, is used for the fitting of stress and plastic strain with time (see Figure 2.19). From the fits, the derivative of

plastic strain is calculated to obtain plastic strain rate. To obtain n versus time (n being the power law describing the creep behavior ($n = \frac{\partial \ln \dot{\varepsilon}_p}{\partial \ln \sigma}$)), power fits are used for successive segments of the plastic strain rate versus stress plots. The same function also has been used for small time intervals to calculate the evolution of n exponent with time (for more details see chapter 4)

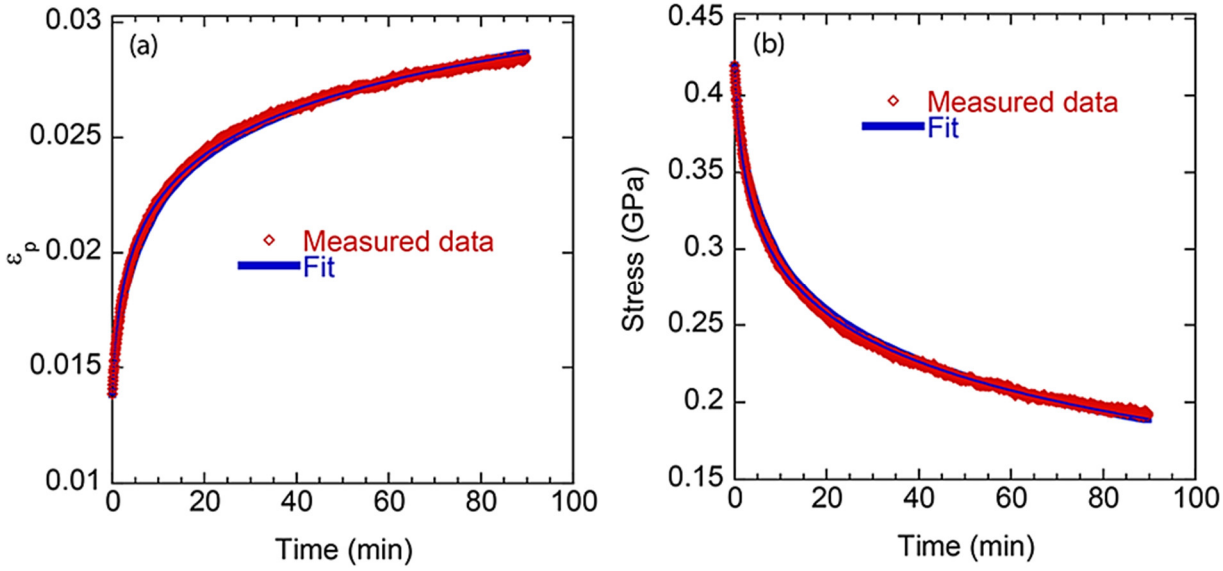

Figure 2.19 Example of fitting of the measured (a) plastic strain and (b) stress evolution during a relaxation segment, from which the evolution of plastic strain rate with stress and the evolution of n with time can be calculated. This example corresponds to S1R1 in Figure 4.5(b) and (d).

2.1.6.5 Drift

The long-term stability of the MEMS setup was characterized by monitoring the evolution of the measured capacitance changes for CS_1 (i.e., no specimen attached onto the MEMS device) over large numbers of cycles. Figure 2.20 (a) shows the typical evolution of the change in measured capacitance at $V_{in} = 0$ with respect to $N = 0$, for more than 6000 cycles. The signal is stable (except for a few cycles between $N = 500$ and $N = 1000$ cycles) with a noise of about 0.2 fF. Figure 2.20 (b) shows

the repeatability of the measured ΔC_1 vs V_{in} for 100 cycles, also highlighting the precision of these electrical measurements.

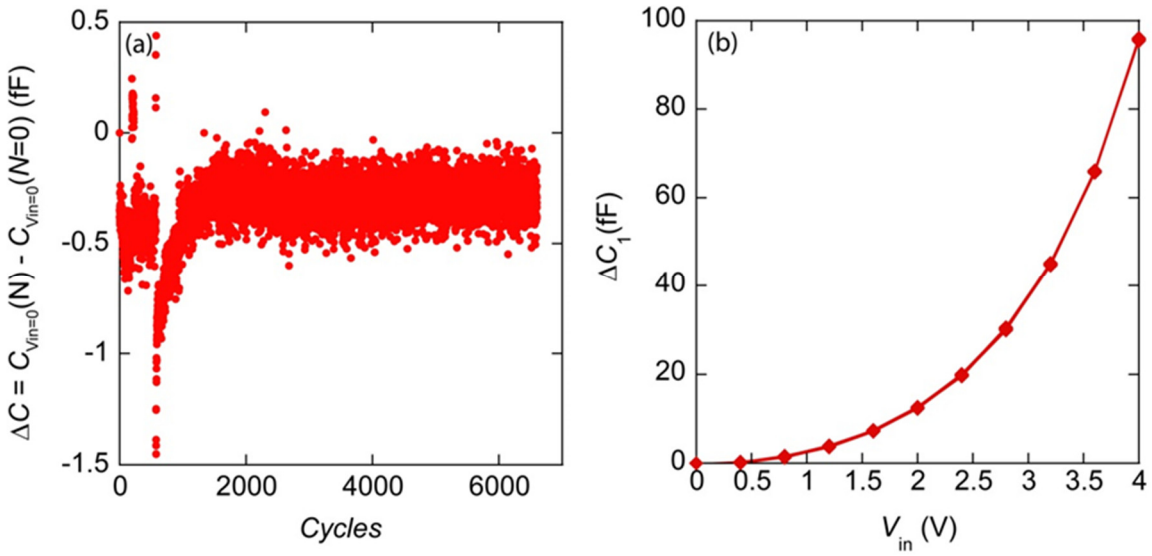

Figure 2.20 (a) Evolution of capacitance measurement at $V_{in} = 0$ V for the MEMS setup without a specimen, as a function of cycling (between 0 and 4 V). (b) ΔC_1 vs V_{in} measured for 100 consecutive cycles (without a specimen), highlighting the precision and repeatabily.

Similar to fatigue tests, the relaxation experiments also require proper stability of the MEMS setup to enable accurate calculation of the plastic strain and stress evolutions with time. The mechanical stability of the thermal actuator was checked by applying $V_{in} = 3$ V for 1 hour inside the TEM. No drift in the thermal actuator displacement X_A (without any specimen) could be detected by comparing TEM images. In addition, for *ex situ* experiments, no visible signs of thermal degradation was observed on the actuator surface after multiple device use at $V_{in} =$ 3 V for several days. The electrical stability of the MEMS setup was also characterized by monitoring the changes in ΔC_1 at a given V_{in} (when no specimen is attached) before and after long *ex situ* tests. Figure 2.21 shows these changes for 4 different specimens, which vary between -3 and +1 fF (specimens 3 and 4, with

lower amount of drifts, correspond to shorter tests; for more details see chapter 1). These changes suggest electrical drift, also evidenced when measuring the evolution of ΔC_1 as a function of time without any specimen. However, the measured total changes in ΔC_1-ΔC_2 during the relaxation experiments, also shown in Figure 2.21, are at least three times more than the measured drift, and always positive values (consistent with relaxation). Therefore, while the occurrence of electrical drift during these tests cannot be ruled out, the measured signal for the relaxation experiments is most likely related to the viscoplastic deformation of the Au specimens. This is also confirmed in the stress-strain curves shown in Figure 4.1 and Figure 4.3.

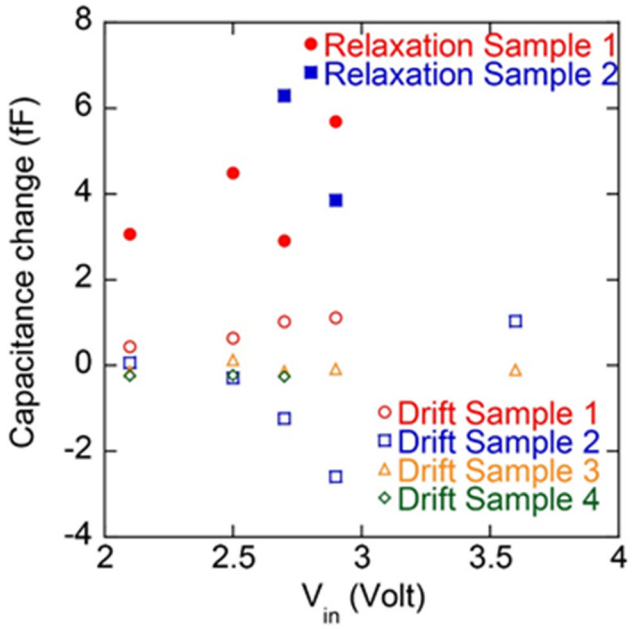

Figure 2.21 Comparison of ΔCS measurements for the MEMS setup for the relaxation tests (MEMS with specimen) and drift experiments (MEMS without any specimen) in different applied V_{in}.

2.2 Fabrication and Characterization of NC Ultrathin Films

This section discusses the design, fabrication and characterization of ultrathin specimens of different FCC metals.

2.2.1 Specimen Geometry

The geometry of the thin-film specimens were modified from a simple nanobeam to a dogbone-shaped specimens to develop a "FIB-less" method to manipulate and clamp the specimen onto the MEMS device. This would allow manipulation of the specimens while removing several drawbacks of FIB-based techniques (For further details see section 2.3).

This specimen consists of a nanobeam in the center (width ~1.5 μm, length ~20 μm, thickness t), with two large pads (~50 by 50 μm^2) on each ends as show in Figure 2.22. The thickness t of the specimen should not exceed 150-200 nm to provide adequate TEM imaging. The length (~20 μm, depending on the exact location of the glue, which can be measured accurately with SEM images) and width (~1.5 μm) were chosen such that K_S is commensurate with K_{LS} to enable its testing to failure (which cannot occur if $K_S >> K_{LS}$). As such, the volume of material that is tested under tension is approximately 1 μm^3, resulting in the ability to perform *in situ* TEM experiments on NC thin films made of a large number of grains ranging from ~10^4 to ~10^6 grains.

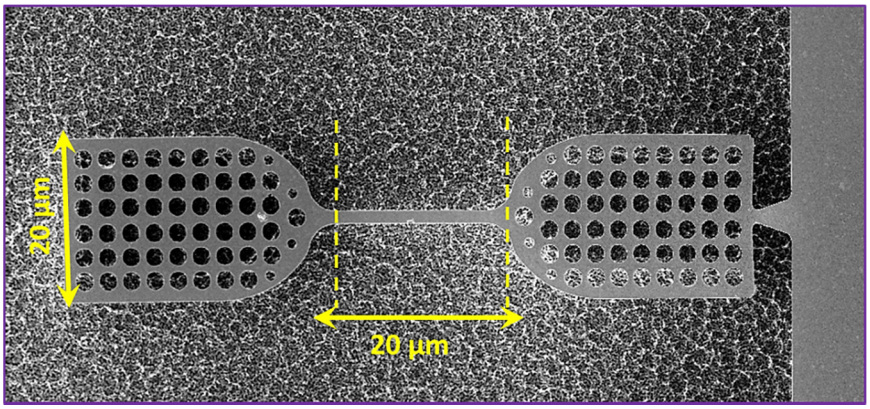

Figure 2.22 SEM image, showing the geometry and dimensions of the dogbone freestanding cantilever, designed for easy specimen manipulation and clamping

2.2.2 Fabrication Process Flow

Figure 2.23 is a schematic of the fabrication process for the ultrathin Au specimens on (100) Si substrates. First, photo-lithography (using Karl Suss MA-6 Mask Aligner with 365 nm wavelength) was performed on a 1.5-μm thick negative resist (NR9-1500PY) film that is spin coated on the substrate (see Figure 2.23 (b) and (c)). After a 20-minute post-baking, the pattern was developed by immersing in a resist developer, RD6. It was then exposed to 90-second descum in a Vision Reactive Ion Etching (RIE) tool to remove any residual resist from the developed areas. High-purity NC metallic thin films were then deposited using a Denton Ebeam Evaporator with selection of the respective crucible in high vacuum and a rate of 0.5 Å/sec (see Figure 2.23 (d)). Then, a lift-off technique was used by acoustic agitation in an acetone solution (see Figure 2.23 (e)). Finally, the specimens were released from the substrate using XeF_2 as an isotropic etchant of Si (using a Xactix XeF_2 etcher); see Figure 2.23 (e). The main issue in the fabrication is to get flat residual-stress free films. The etch time was chosen so that the specimens were free-standing

(due to XeF_2 partial etching of Si substrate), and connected on one side to a large anchor pad through a small strip for easier manipulation/placement onto the MEMS device (see Figure 2.22).

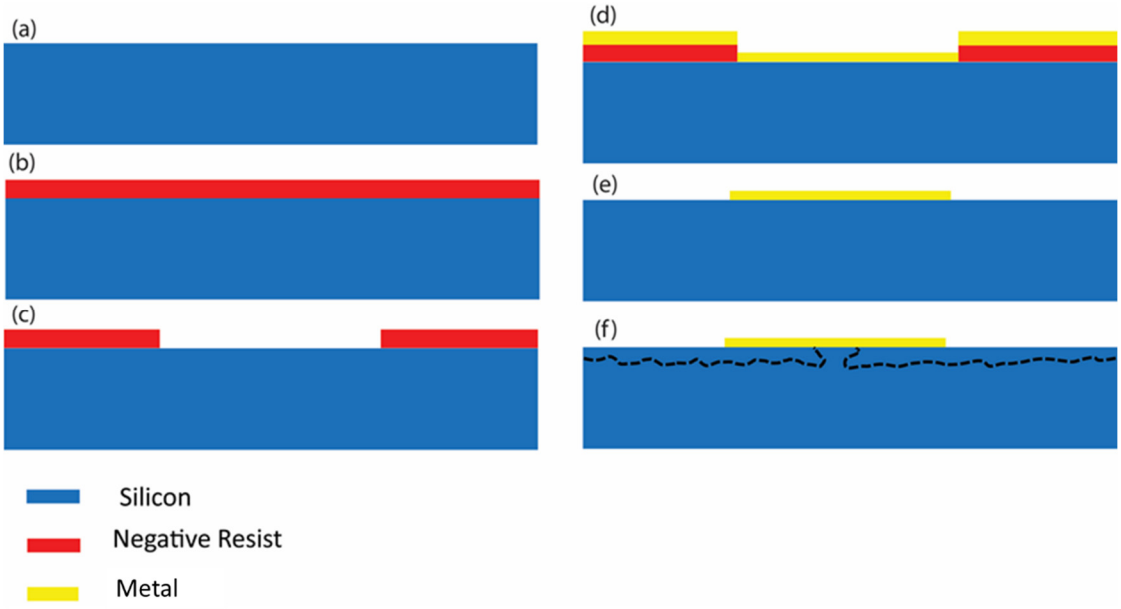

Figure 2.23 Schematic of the ultrathin metallic film fabrication process. See text for details.

NC gold thin films were deposited at a pressure of 8×10^{-7} Torr and a rate of 0.5 Å/sec with a 99.995% purity target. The deposition was interrupted for 15 min after depositing half of the final thickness to minimize the growth of columnar grains. Gold specimens were fabricated with two different thicknesses of 100 nm and 30 nm. The critical step to minimize the line edge roughness of the specimens is the patterning of the photoresist used for the lift-off technique. Figure 2.24 (b) shows specimens with very smooth edge features. In contrast, the tested specimens for cyclic loading, shown in chapter 3, were from a fabrication batch that had rougher edge features (see for example, Figure 3.8).

Similarly, thin film cantilevers of other FCC metals including, aluminum, nickel, platinum and copper were deposited and released. Table 2.3 summarizes the deposition parameters of the fabricated specimens.

Table 2.3 Deposition parameters of thin film specimens for five different FCC metals

Metal	Thickness (nm)	Pressure (Torr)	Purity (%)	Deposition rate (Å/sec)
Au	100/30	8×10^{-7}	99.995	0.5
Al	50	1.4×10^{-6}	99.99	0.5
Ni	50	6×10^{-6}	99.995	1
Pt	30	2.2×10^{-6}	99.99	1
Cu	50	2.1×10^{-6}	99.99	1

2.2.3 Microstructural Characterization of Thin Films

Figure 2.24 shows SEM (Figure 2.24 (a)-(f)) and TEM (Figure 2.24 (g)-(i)) images of the NC gold (Au) thin film specimens with thickness of 100 nm. These images show a NC microstructure for the 100-nm-thick Au films with a wide distribution of grain size ranging from 20 to 350 nm. Selected area electron diffraction patterns (see example in inset of Figure 2.24 (g) reveal a heterogeneous microstructure without any strong out-of-plane or in-plane texture. The lack of a strong <111> out-of-plane texture (which is typically observed for thin Au films) may result from the deposition of the film on a Si substrate with the presence of a thin native oxide. A representative SEM and HRTEM image of an as-released specimen are shown in Figure 2.25 (a)-(c). SEM, TEM and STEM images of

specimens with thickness of 30 nm. These images confirm that the specimens are nanocrystalline uniform films with no in-plane texture. Flatness of the Au cantilevers implies that the films are free of residual stress. Although the gold specimens (both 100 nm and 30 nm) were fabricated by a similar fabrication recipe the films with the thickness of 30 nm differs significantly in nanostructure from its thicker counterparts (100 nm). For example, 30 nm-thick films have a narrow grain size distribution compared to 100 nm films with a wide distribution (see Figure 2.25 (c) and (d)). This provides a unique opportunity to study how the film thickness and grain size distribution of nano-grains affects the plastic deformation mechanisms (for more details see chapter 5).

Similar to Au films, the other fabricated FCC metals were characterized by TEM/ SEM imaging. Figure 2.26- Figure 2.29 present the nanostructure of Al, Ni, Pt and Cu respectively. Selected area electron diffraction patterns in all of these metallic films reveal a heterogeneous microstructure without any strong in-plane texture. Each metal has a different average grain size. TEM images for Al shows a narrow distribution of grain size ranging from 10 to 50 nm (see Figure 2.26) and more than one grain through the thickness of the film. In Ni and Pt the grain size is much smaller and both have a uniform grain size between 5 to 10 nm.

All of the abovementioned metals are flat cantilevers and hence free of residual stresses. However, Figure 2.29 (a) reveals that for Cu films there is a significant residual stress which made most of the specimens bent therefore extremely difficult to manipulate the specimens. The high residual stress for Cu could have been

generated by the grain growth in the deposition stage. Growth of discrete islands of crystals would eventually make them as neighboring grains and hence normally drive lateral contraction of the film; however contraction is constrained by the underlying substrate. This could add tensile stress in the Cu films but the details of relationship between deposition parameters of evaporated film and residual stress is unknown [148].

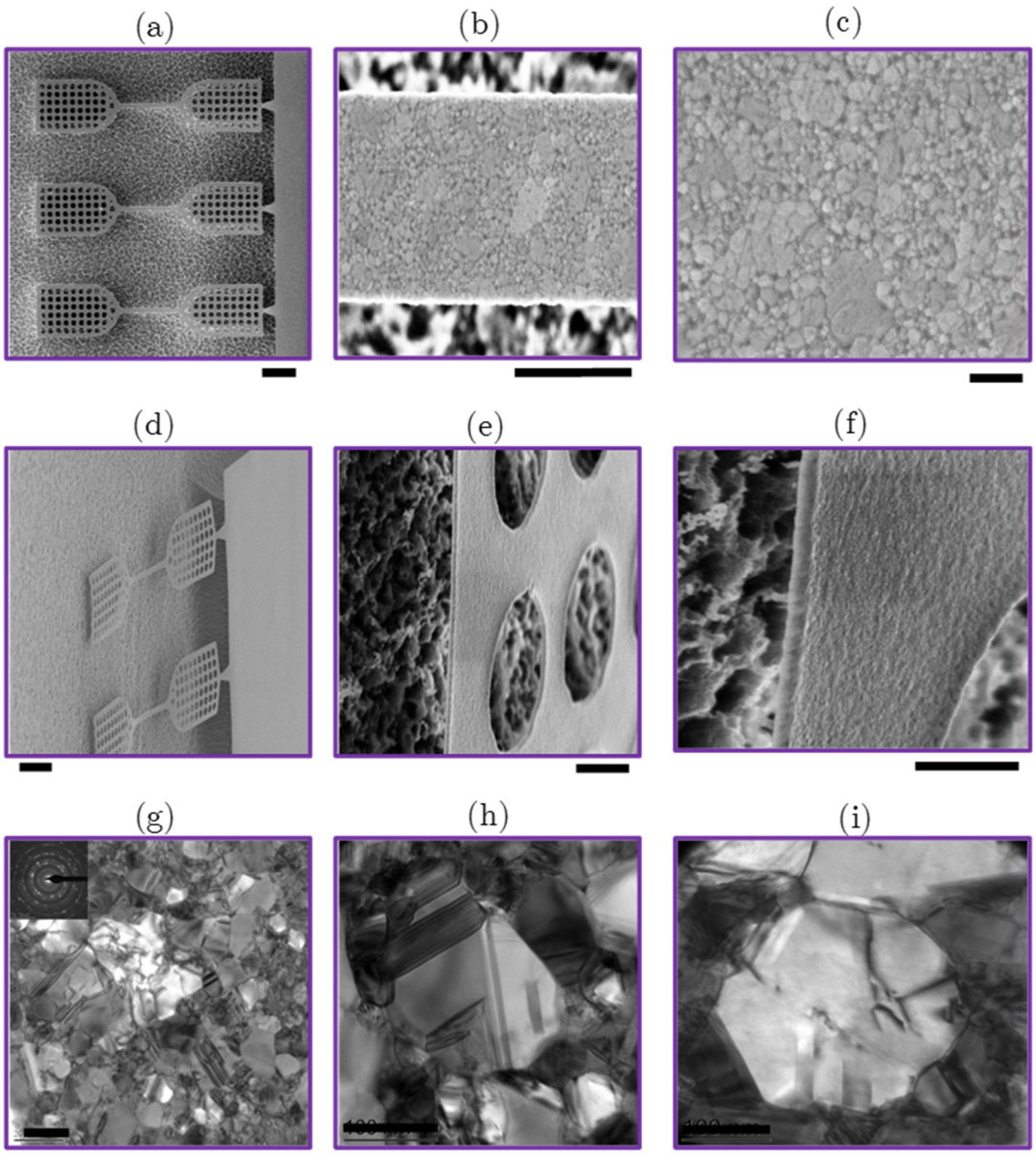

Figure 2.24 (a),(b),(c): Top-down SEM images of Au thin film specimens with large pads on each end for FIB-less manipulation and clamping onto a MEMS device (Scale bar: 1μm, 2 μm and 100 nm, respectively). (d), (e), (f): Inclined SEM images showing 100-nm-thick freestanding Au specimens attached on one side to large island of material. (Scale bar: 1 μm). (g), (h), (i): TEM images of the Au specimens and selected area electron diffraction patterns showing no strong texture. (Scale bar: 100 nm)

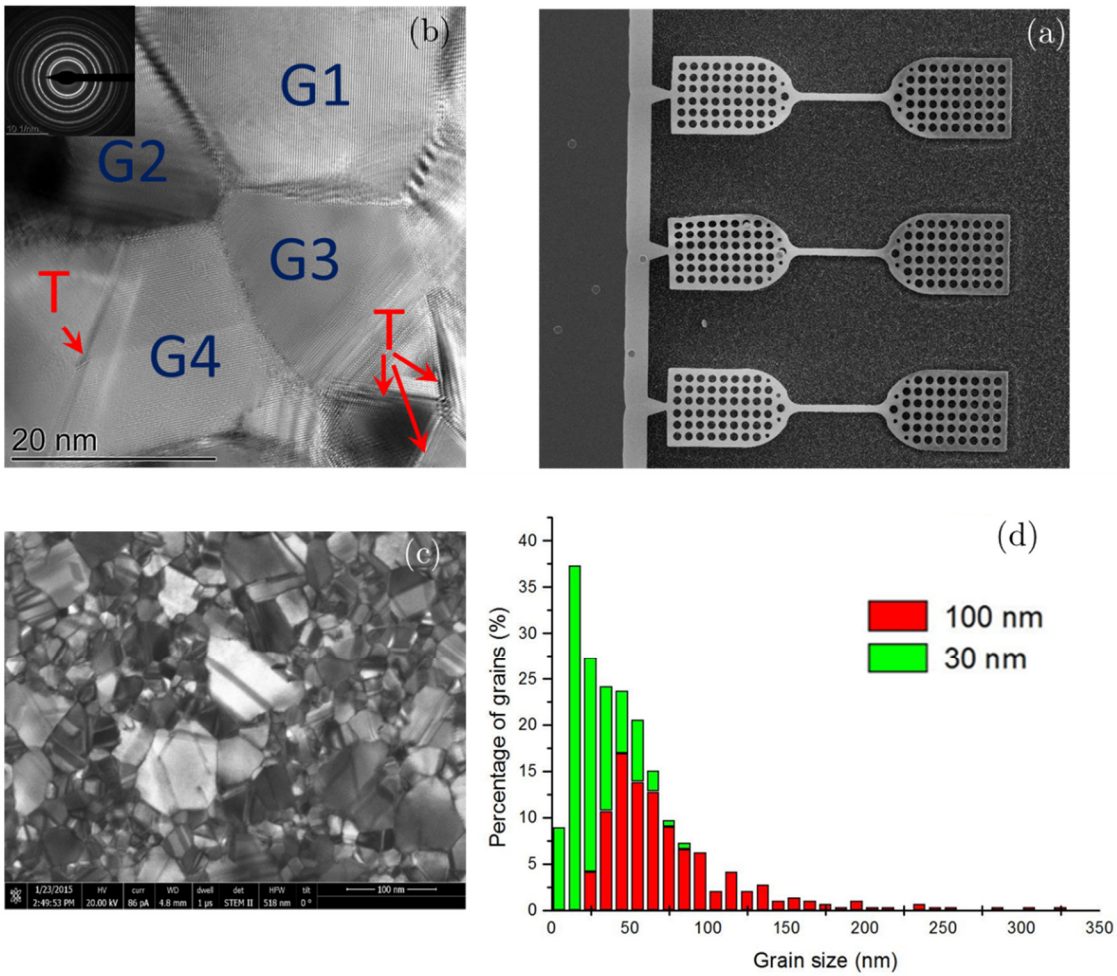

Figure 2.25 (a) SEM image of dogbone 30 nm thick Au specimens (b) High-resolution TEM micrograph of the surface morphology of grains for 30 nm-thick films and diffraction pattern, shown as inset. (c) STEM micrograph of 30 nm-thick film [image courtesy of Jan Philipp Liebig] (d) Histogram of the grain size distribution of the specimens with 30 nm and 100 nm thickness.

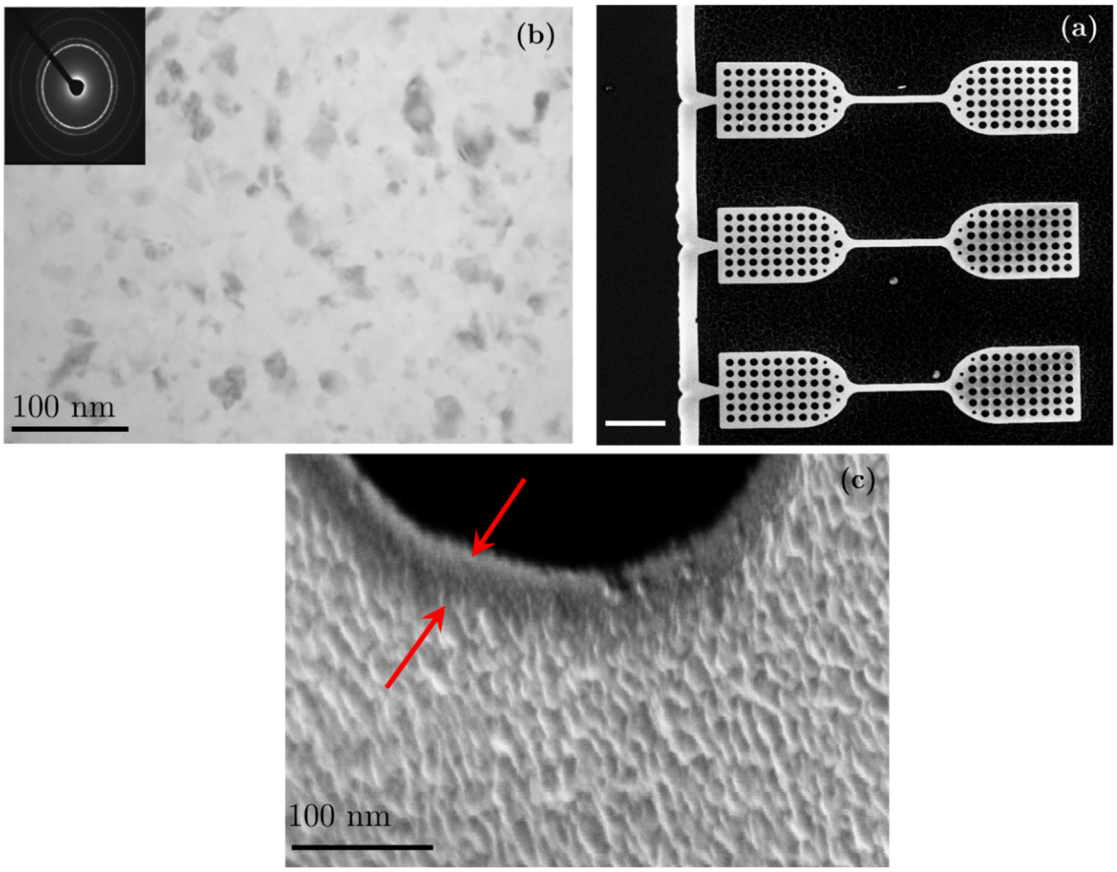

Figure 2.26 (a) SEM image of dogbone 50 nm thick Al specimens (b) Bright field TEM micrograph of the surface morphology of grains for 50 nm-thick films and diffraction pattern, shown as inset. (c) Inclined SEM micrograph of film, showing through the thickness of the specimen close to a hole in the clamp area.

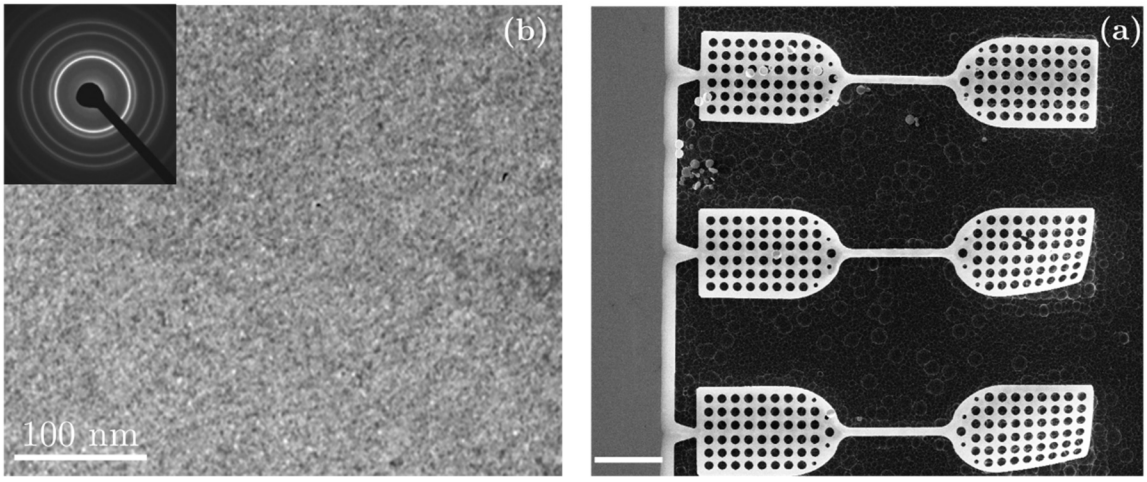

Figure 2.27 (a) SEM image of dogbone 50 nm thick Ni specimens (b) Bright field TEM micrograph of the surface morphology of grains for 50 nm-thick films and diffraction pattern, shown as inset.

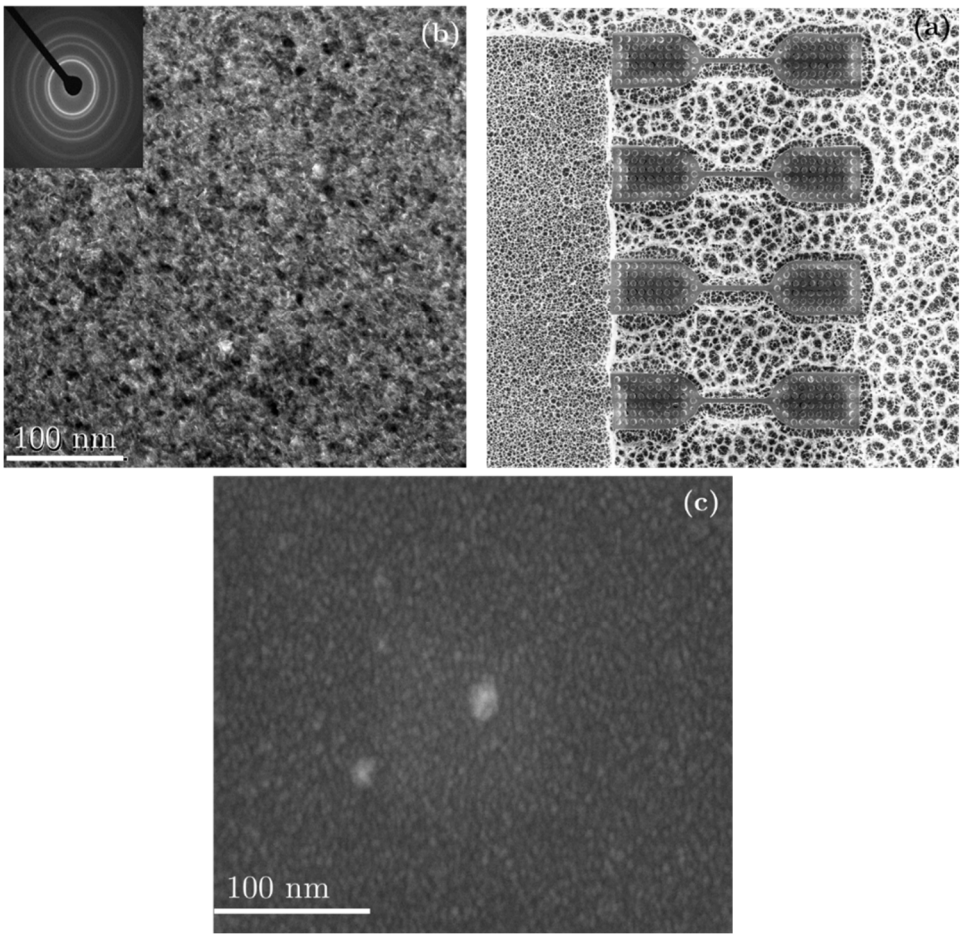

Figure 2.28 (a) SEM image of dogbone 30 nm thick Pt specimens. The large island has been removed during the etching and the cantilevers are not fully released. However, they could be detached from the specimen die by pushing the strip with a probe tip. (b) Bright field TEM micrograph of the surface morphology of grains for 30 nm-thick films and diffraction pattern, shown as inset. (c) SEM micrograph of 30 nm-thick film.

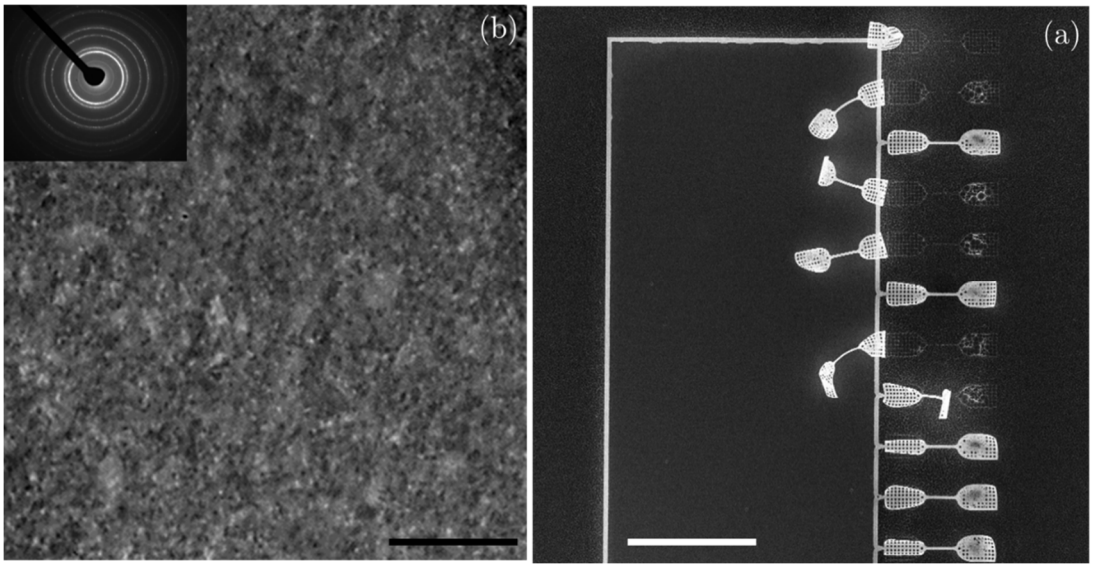

Figure 2.29 (a) SEM image of dogbone 50 nm thick Cu specimens. Scale bar is 100 nm (b) Bright field TEM micrograph of the surface morphology of grains for 50 nm-thick films and diffraction pattern, shown as inset.

2.3 Manipulation and Clamping of Nanospecimens onto MEMS

The manipulation and clamping of small scale specimens, including ultrathin films, is a notorious challenge in experimental nanomechanics [40]. One previously employed approach to circumvent these issues is the co-fabrication of the thin film specimen along with the MEMS tensile machine [43, 149, 150]. Such an approach limits the MEMS device to a single use as well as the choice of materials to be tested. Another approach often employed for the testing of nanowires relies on the use of a micromanipulator inside a dual focused ion beam scanning electron microscope (FIB/SEM) to manipulate the nanowire onto the testing platform. In that case, clamping of the nanospecimen is performed with electron or ion beam induced deposition of platinum (Pt). This technique also suffers several drawbacks, including possible compliance of the Pt clamps, Pt overspray covering the surface of the specimen, and ion-beam damage of the specimen's surface (See Figure 3.8). While

the compliance of the Pt clamps can be accounted for if strains are measured based on digital image correlation of high magnification images [151], the issues of Pt overspray on the specimen and Ga implantation damage associated with the FIB manipulation may result in surface damage which can significantly affect the fatigue results.

2.3.1 Overview of the Procedure

Based on the above considerations, we developed a "FIB-less" method to manipulate and clamp the ultrathin film specimens onto the MEMS device. Specifically, we modified the geometry of the ultrathin film specimen from a simple nanobeam to a dogbone-shaped specimen (See Figure 2.22). The large pads allow manipulation of the specimens under a probe station and can be attached to the MEMS device with a UV-curable adhesive Dymax Light Weld 425, thereby eliminating the FIB manipulation step and providing stiff clamps (given the large contact area for gluing).

Briefly, the small strip of material connecting the specimen to the substrate (See Figure 2.22) is detached using a probe tip fitted to a micromanipulator, under a probe station. The specimen, whose large pad is in contact with the probe tip, is then transferred to the MEMS' gap, where UV curable epoxy has been dispensed (but not cured) on each side. The micromanipulator allows proper in-plane alignment of the specimen with respect to the MEMS' gap, after which the specimen is lowered until it touches the epoxy. The epoxy is then cured using a UV light. Overall, the yield associated with this procedure is acceptable, and specimen misalignment (such

as the specimen shown in Figure 3.3, one of the earlier specimens manipulated with this technique) can be minimized with proper experience.

2.3.2 *In situ* SEM Test

A series of *in situ* SEM experiments was performed to observe MEMS device and the deformed Au specimen during operation, especially at the location of the clamps which cannot be observed inside a TEM. The MEMS device was mounted on a prototype electrical biasing SEM holder (Hummingbird) inside a FEI Nova NanoLab 200 dual-beam microscope as shown in Figure 2.30. A cyclic test was carried out on one Au specimen before performing a monotonic test to failure. First, cyclic loading was applied by varying V_{in} between 0 and 2 V for approximately 200 cycles. The deformation of the specimen shows no apparent permanent deformation of the Au specimen's clamps, confirming the previous results. The specimen was then elongated to failure by increasing V_{in} from 0 to 4 V. Failure occurred along the specimen gauge length, away from the clamps.

Therefore, this *in situ* test highlight the apparent effectiveness of the FIB-less specimen manipulation and clamping onto the MEMS device, as well as of the electrical sensing scheme for stress and strain calculation.

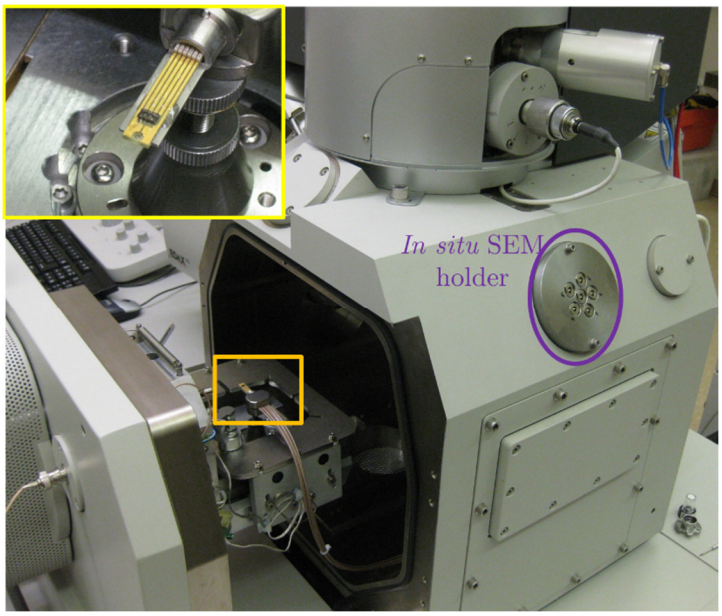

Figure 2.30 Experimental setup for *in situ* SEM experiment with Hummingbird electrical biasing holder with specimen carrier the an inset, mounted inside Nova NanoLab 200 FIB dual-beam microscope.

2.4 Advantages of the Experimental Technique

This experimental technique represents a significant advance in the state-of-the-art of the MEMS-based nanomechanical testing techniques. The major advantage of the experimental technique is its capability to use TEM imaging solely for high magnification microstructural observations while the MEMS device provides continuous tracking of the material's response, thereby expanding the capabilities of MEMS-based techniques towards more complex *in situ* TEM nanomechanical tests, such as stress relaxation and fatigue tests. In essence, the presence of the two capacitive sensors eliminates the constraint of the existing techniques to measure the evolution of the specimen gap to calculate strain [43, 45, 152, 153](as well as stress) [149, 154, 155] or the deformation of the stiffness beams using relatively low-magnification electron images.

The quantitative nature of the technique allows investigation of important governing parameters on the material's time-dependent response such as evolution of the stress-strain curves, crack initiation lives, maximum applied stresses and plastic strains, and load ratio R in a range of frequencies up to 0.5 Hz. Another critical aspect of the technique is its ability to perform *ex situ* tests and interrupt them with *in situ* TEM observations, such that the environmental effects (including the effects of the native surface oxide for reactive NC metals) on plasticity and fracture can be quantified. Moreover, A FIB-less manipulation and clamping technique was developed to secure the specimens onto the MEMS device without inducing ion-beam-related damage.

2.5 Challenges of the Experimental Technique

Although this experimental technique represents some crucial advance in nanomechanical testing there are still some challenges that needs to be considered and addressed, as listed below:

2.5.1 Charging

Charging of the specimen inside SEM/TEM could result in rupture of in the gauge section. It could also induce electrical force, and consequently repulsion of the broken facets as shown in Figure 2.31. This could make it difficult to measure the plastic overlap in the thin film. Additionally, charging could deviate the direction of electron beam in TEM column, add stigmation and hinder focusing on the specimen.

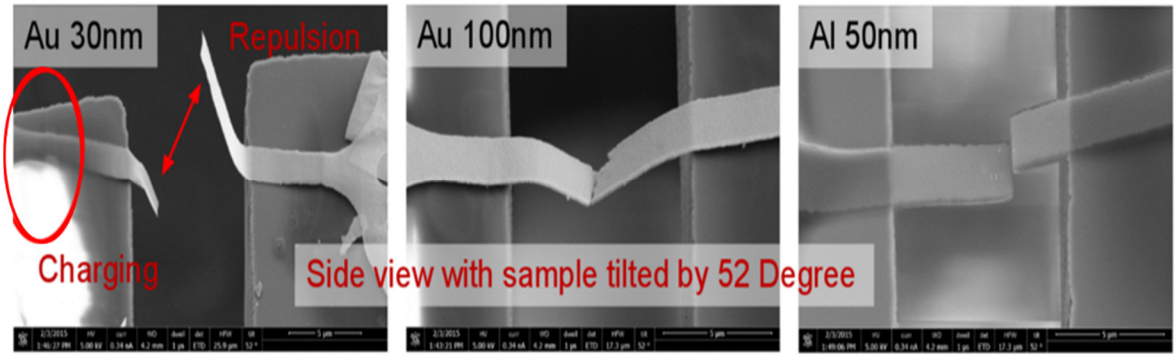

Figure 2.31 Bent samples and charging of the specimen [images courtesy of Jan Philipp Liebig]

2.5.2 Misalignment

While the developed specimen manipulation procedure circumvents the need to use FIB and removes altogether the damage associated with FIB, it is still a challenge to clamp a specimen with minimum bending and/or misalignment with respect to the tensile direction (see Figure 3.3). As such, bending stress may not be ignored as it could insert stress on the order of axial stress. This could affect the accuracy of strain and stress measurements in the film as the specimen is inherently assumed to be stress-free before the test.

2.5.3 Strength of the Clamps

Strong and stiff clamps that properly secure the specimen to the testing stage, is another important issue that still remains a big challenge for nanomechanical testing. In particular, stiffness of the two clamps are crucial since the elongation X_S of the specimen is assumed to be equal to change in the specimen gap. This is only true when there is no slip or deformation at the two grips. This could be even more important as the clamping material is a UV curable epoxy with elastic modulus of

2.7 GPa. While this value of modulus should be more than enough given the area of the clamps [156], there still exists issues with low measured elastic modulus of the specimen. For example, a wide range of E values from 15 to 70 GPa were obtained for 100 nm Au specimens. This could be related to the poor curing of the glue underneath the specimen [156]. Hence, the manipulation process should be carried out with scrupulous attention to details such as transferring the precise volume of the glue from the probe tip to the right area of the specimen grip. In addition, the glue underneath is not enough to provide the required clamping [156]. It is possible that the glue underneath the specimen is not getting cured under UV light, which is possible since the specimen is not transparent. In fact, having glue on top of the sample helps to get larger E value [156]. Determination of the specimen's length, to be used in strain calculation, is also an issue especially in cases which no glue is placed on top of the clamps.

2.5.4 Post-processing

Sensing circuit suffers from a limitation that only $\Delta C_1 - \Delta C_2$ is measured and therefore the calculation of load and displacement involves an underlying assumption of elastic behavior of the thin film under tension. Further refinements in the sensing technique have already been implemented [156]. For example, it would be more straightforward to directly measure ΔC_1 and ΔC_2 (i.e. ${X_A}^F$ and X_{LS}) during the test to calculate stress and strain, instead of the current sensing scheme ($\Delta C_1 - \Delta C_2$ with and without a specimen; see section 2.1.6.1 for further details) which requires an iterative procedure to accurately calculate ${X_A}^F$ and X_{LS}. Appropriate modifications

in the sensing circuit allows more straightforward measurements, which in turn facilitates the development of force-controlled mechanical testing schemes with closed feedback control [156].

CHAPTER III

MONOTONIC AND FATIGUE FAILURE OF NC ULTRATHIN AU FILMS

3.1 Introduction

This chapter presents the experimental results on fatigue testing of NC ultrathin films. These challenging tests are performed for the first time, thanks to our unique MEMS-based technique that relies solely on capacitive sensing of both applied force and specimen elongation (for more details of the experimental setup see chapter 2). In section 3.2-3.4 the MEMS-based tensile testing setup is employed to measure the monotonic and fatigue properties of ultrathin NC Au thin film specimens. The results also include TEM and SEM analysis of nucleated nanocracks and evolution of microstructure. This chapter continues with the results of a fatigue test on NC nickel nanobeam to highlight some practical issues associated with the nanobeam manipulation/clamping procedure in the FIB that motivated us to fabricate the dog-bone shaped specimens that could be manipulated in a "FIB-less" manner (see section 3.5).

3.2 Monotonic Tests

Figure 3.1(a) and (b) show the measured $\Delta C_1 - \Delta C_2$ vs. V_{in} for two *ex situ* monotonic tests to failure of our Au specimens in laboratory air (K_{LS} = 480 N/m for these experiments). The data are divided into the loading section (from 0 to 4 V for specimen 1 and from 0 to 3 V for specimen 2), and the unloading section (going back to 0 V), along with the same data before the specimen is attached to the MEMS device (representing ΔC_1 vs. V_{in}). Both specimens failed at V_{in} = 3 V, as indicated by the sudden jump in $\Delta C_1 - \Delta C_2$ value resulting from the second capacitive sensor going back to its original position at the specimen's failure. Once the specimen is failed, the measured $\Delta C_1 - \Delta C_2$ vs. V_{in} coincides with the previously measured ΔC_1 vs. V_{in} data. The corresponding stress strain curves are shown in Figure 3.1. The ultimate tensile strengths of the two specimens are about 1 and 1.13 GPa, for a total strain to failure of 2.8 and 5%, and an estimated plastic strain to failure of 1.22% and 0.8%, respectively. The E values for the two specimens are 34 GPa and 30 GPa respectively, based on a linear fit for strains below 0.2%. Figure 3.1(d) and (e) show SEM images of specimens 1 and 2, respectively, before and after testing, including high magnification images of the fracture surfaces. Both specimens failed along the gauge length, away from the clamps. There could be elastic deformation in the specimen grips and low value of elastic modulus might be a clue for this. Nonetheless no apparent permanent deformation of the epoxy clamps could be observed. The fracture surfaces suggest intergranular failure. The approximate amount of plastic elongation (based on SEM images) was 90 nm for specimen 1, which compares well

with the calculated plastic elongation to failure (81 nm using E = 30 GPa). The measured plastic overlap may be larger than the calculated value given that the last calculated stress and strain values are for V_{in} = 2.8 V (for which X_{LS} = 529 nm, corresponding to F = 255 μN, and X_S = 164 nm), while the specimen may actually be further deformed at V_{in} = 3V before it fails. This discrepancy can be minimized by reducing the increments in V_{in}. In any case, the fact that the calculated plastic elongation (based on the stress strain curve that relies on specimen's crosshead displacement) does not overestimate the measured plastic elongation suggests that the epoxy clamps do not have permanent deformation while elastic deformation might be existent. Our measured properties are also consistent with previous studies on NC Au thin films [43, 92, 122, 149, 157, 158]. For example, Yilmaz and Kysar measured E = 53 GPa, a tensile strength of 0.94 GPa, and plastic strain of 2.5% for similar evaporated Au ultrathin films (thickness: 40 nm, width: 350 nm, length: 7 μm) [149]. Our similar tensile strengths are larger than that measured on specimens with much larger widths or length (hundreds of μm), suggesting the possibility of a geometric size effect governing the failure of these NC small-scale specimens. The calculated elastic modulus, E, of the Au specimens is ~25–50 GPa, which is lower than the values of other reports, ranging from 50 to 70 GPa [43, 92, 122, 149, 157, 158], highlighting the compliance issues of the glue.

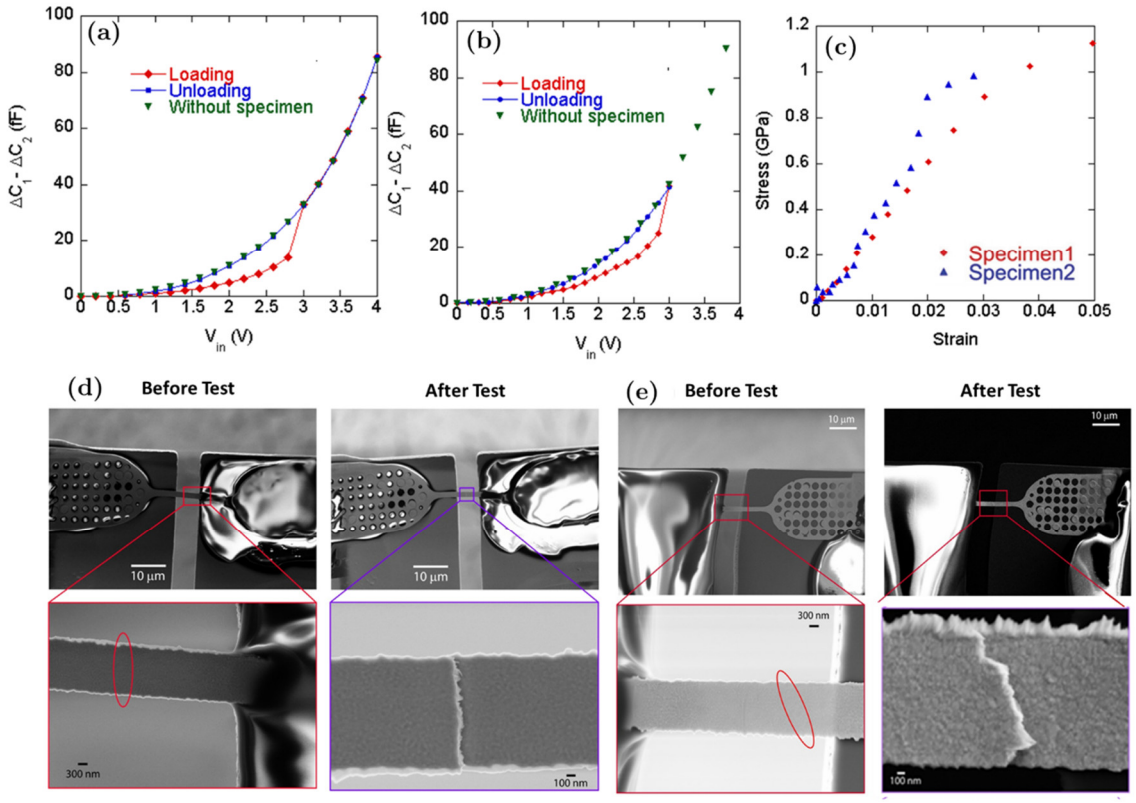

Figure 3.1 (a) Electrical raw data for monotonic test to failure of specimen 1. (b) Electrical raw data for monotonic test to failure of specimen 2. (c) Corresponding stress-strain curves of specimens 1 and 2. (d) Low and high magnification SEM images of specimen

3.3 *Ex situ* Fatigue Test of a NC Au Specimen

Figure 3.2 and Figure 3.3 show the results of an *ex situ* fatigue test of another NC Au specimen performed in laboratory air (K_{LS} = 480 N/m for this experiment). The driving voltage V_{in} was cyclically varied from 0.4 to 1.8 Volt in increments of 0.1 Volt for 11,125 cycles, after which the test was interrupted. This corresponds to a fatigue test with a load ratio $R = \sigma_{min} / \sigma_{max}$ ~0, and a maximum applied stress of ~0.6 GPa, at a frequency of 0.07 Hz. Continuous acquisition of the ΔC_1-ΔC_2 vs. V_{in} data was performed throughout the entire test, which allows the calculation of

the stress-strain curves for all cycles (using an automated procedure, explained in section 2.1.6.3).

Figure 3.2 (a) shows five stress-strain curves for selected cycles, while Figure 3.2 (b)-(c) show the evolution throughout the fatigue test of the maximum applied stress, σ_{max}, permanent strain under no applied stress, $\varepsilon_{\sigma=0}$, respectively. E remains constant during the test ($\sim$47 GPa) and is calculated based on the initial portion of the unloading curves. A ratcheting behavior is observed, with the maximum applied strain, ε_{max}, increasing from 1.3 to 1.9% throughout the test (see Figure 3.2 (a)) and a slight decrease in σ_{max} (from 0.62 to 0.54 GPa). Also, $\varepsilon_{\sigma=0}$ increases from $\sim$0% to 0.6%, with a sudden increase after 6000 cycles. Positive $\varepsilon_{\sigma=0}$ values mean that the specimen is under compression below these values, as shown in Figure 3.2 (a), which is a result of specimen elongation. While some amount of buckling may occur due to the thinness of the specimens (see for example section 3.5), the elongated specimens (with stiffness ranging from 500 to 1500 N/m depending on the actual specimen dimensions) may "push" the load sensing beams (K_{LS} = 100 or 480 N/m), resulting in measured negative stresses.

It is important to note that this evolution is not an artifact of the MEMS device, given that the corresponding changes in the MEMS' output signal are about 5-10 times larger than the noise level, and given the measured long-term stability of the MEMS device over long periods of time (see section 2.1.6.5). This technique can therefore be used to probe minute changes in the material's response that may be indicative of fatigue-related microstructural changes. Figure 3.3 shows SEM images

of the specimen and after interruption of the test ($N = 11{,}125$ cycles). No significant changes in the microstructure (such as grain coarsening) were observed, as illustrated with the high magnification images of the same area before and after the fatigue test. However, the use of post mortem SEM images can only give limited information regarding the development of fatigue damage. Instead, quantitative *in situ* TEM fatigue tests provide the opportunity to observe fatigue-related microstructural evolution, as demonstrated next.

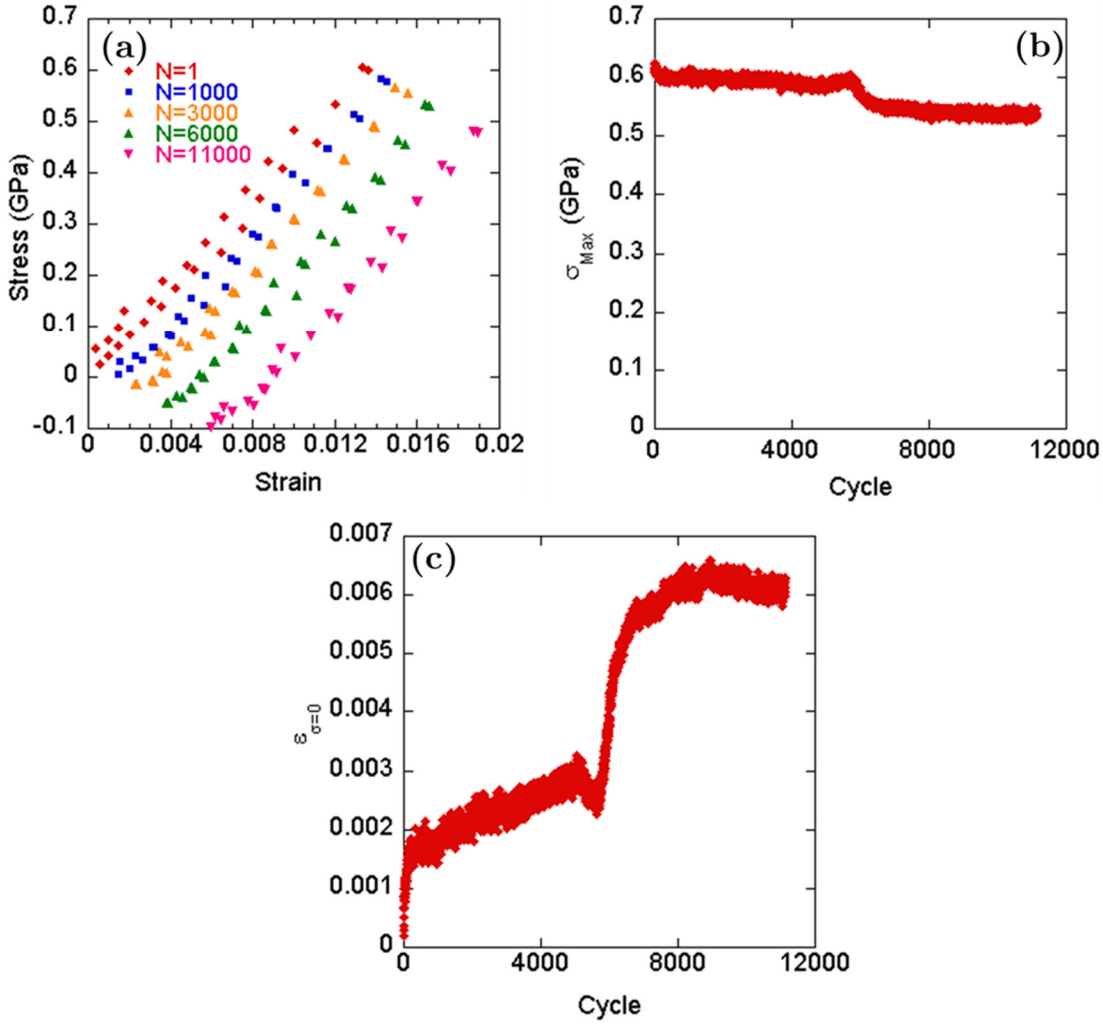

Figure 3.2 (a) Selected stress-strain curves for an *ex situ* fatigue test for five different cycles ($N =$ 1, 1000, 3000, 6000, and 11,000). (b) Evolution of the maximum applied stress, $\sigma_{\max}$, as a function of cycles. (c) Evolution of the permanent strain under no applied stress, $\varepsilon_{\sigma=0}$, as a function of cycles.

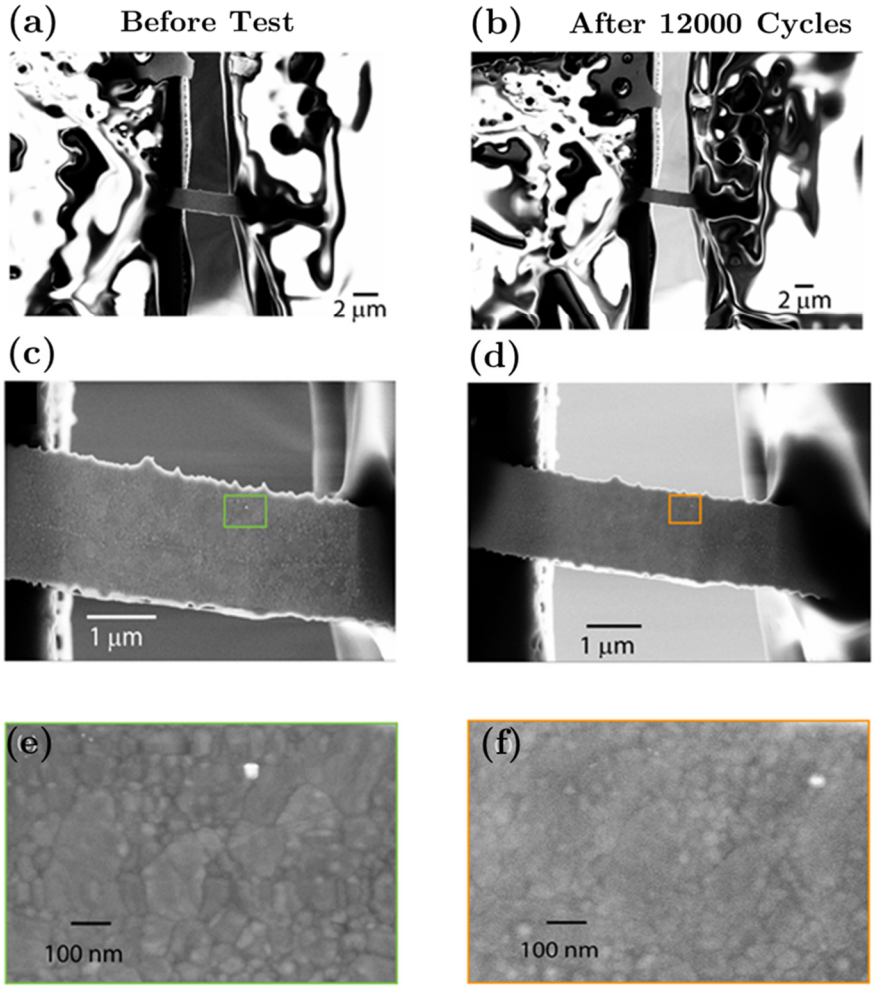

Figure 3.3 SEM images of the specimen before and after fatigue test, respectively. (a) and (b) Low magnification images. (c) and (d) Medium magnification SEM images. (e) and (f) High magnification images of the same area (see same white spot for both images) showing no apparent grain growth after 12,000 cycles at a maximum stress of 550 MPa.

3.4 *In situ* Fatigue Test of a NC Au Specimen

A fatigue experiment was carried out inside a HF 2000 TEM (acceleration voltage: 150 kV), using a Hummingbird electrical biasing holder with 6 leads (see section 2.1.4.3 for more details). The driving voltage V_{in} was cyclically varied from 0 and 4 Volt in increments of 0.4 Volt. This corresponds to a fatigue test with a load ratio R ~0, and σ_{max} ~0.8 GPa, at a frequency of 0.25 Hz (K_{LS} = 100 N/m for this

experiment). The specimen failed after 6995 cycles. TEM observations were performed during the first 500 cycles, after which the electron beam was turned off (the specimen was kept in the TEM chamber for the entire duration of the test). No effect of the beam on the material's response was observed. Figure 3.4 (a) shows five stress-strain curves for selected cycles, while Figure 3.4 (b)-(d) show the evolution throughout the fatigue test of σ_{max}, $\varepsilon_{\sigma=0}$, and E, respectively. A ratcheting behavior is also observed (see Figure 3.4 (a) and Figure 3.4 (c)), with ε_{max} increasing from 5 to ~7% (similar to the fracture strain measured for the monotonic tests shown in Figure 3.1) and $\varepsilon_{\sigma=0}$ increasing from 0 to ~2%. TEM and SEM images of the specimen after fatigue failure (see Figure 3.5 (b)-(g)) reveal the formation of a fatigue nanocrack (~300 nm long) near the fracture surface. A large amount of dislocation-based plastic deformation at the tip of this fatigue crack is observed in Figure 3.5. (e) and (f). Figure 3.5 (g) also reveals embryos of surface cracks near the fatigue nanocrack. The area near the fracture surface is also associated with large densities of dislocations (see Figure 3.5(c)-(d)). A comparison of the SAED patterns away from the fracture surface and near the fracture surface (see Figure 3.5 (h) and (i)) suggests that near the fracture region a number of neighboring grains rotated into strong diffracting conditions for either the (111), (200) or (220) planes.

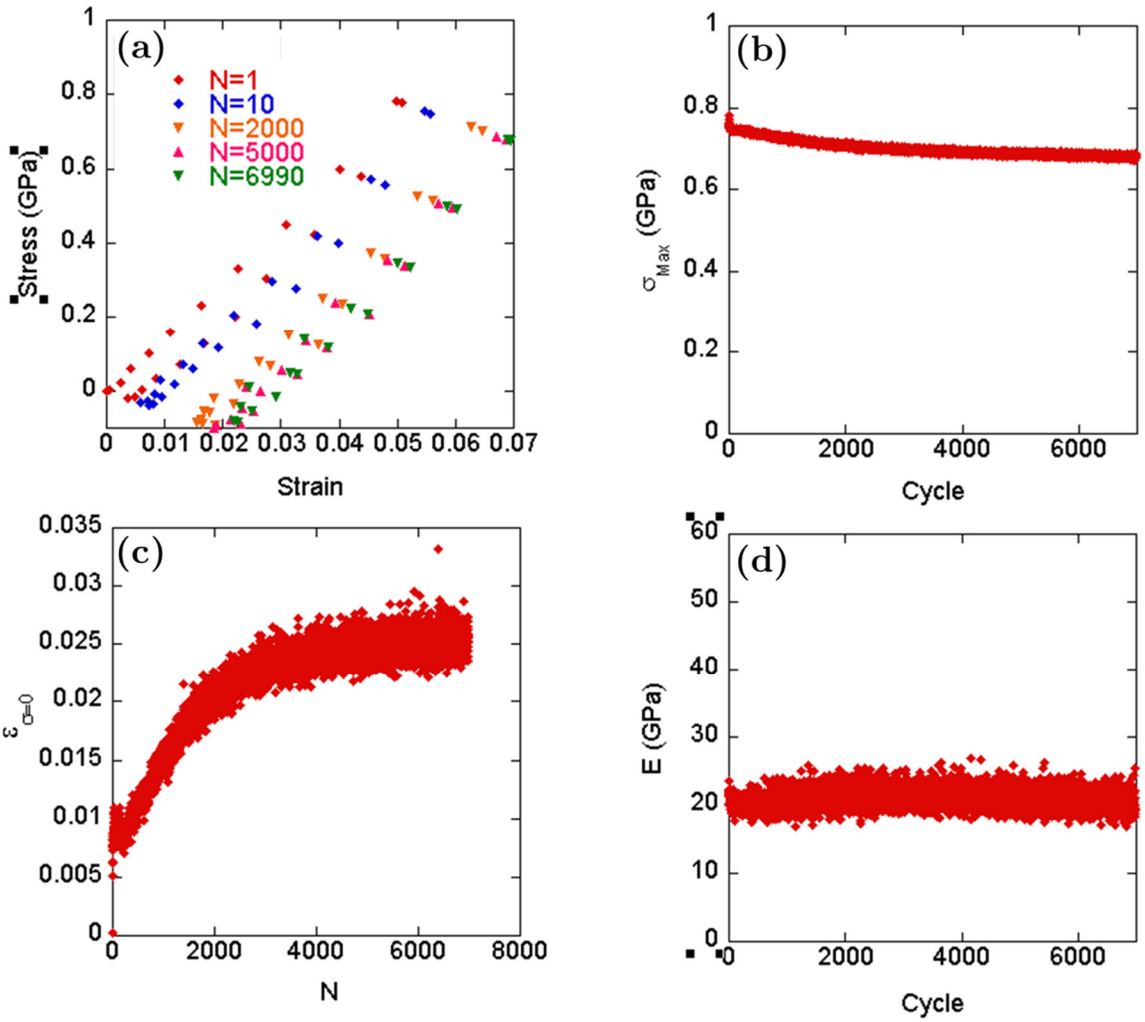

Figure 3.4 Selected stress-strain curves for an *in situ* TEM fatigue test for five different cycles (N = 1, 10, 2000, 5000, and 6990). (b) Evolution of the maximum applied stress, σ_{max}, as a function of cycles. (c) Evolution of the permanent strain under no applied stress, $\varepsilon_{\sigma=0}$, as a function of cycles. (d) Evolution of elastic modulus, E, as a function of cycles.

The fatigue-related microstructural events leading to the formation of this nanocrack and fracture of the specimen were not captured given that the beam was turned off when failure occurred. However, the microstructure evolution was observed during the first 500 cycles. Figure 3.6 shows a series of bright-field TEM images of a small portion of the specimen at different applied stresses at $N = 400$ cycles, along with a comparison of the same portion at the beginning of the fatigue

test. Continuous changes in contrast could be observed for many grains during cyclic loading in bright-field TEM observations, implying that dislocation-mediated processes are active in this grain-size regime [122, 159]. Dislocations can also be observed in a large grain in the center, as highlighted with the zoomed area in Figure 3.6 (f). Figure 3.6 also shows twins and stacking faults (see red arrows in Figure 3.6 (a) and (b)). The occurrence of stacking fault formation and mechanical twinning can be expected for a material like NC Au [160, 161], given its relatively large ratio $\gamma_{usf}/\gamma_{sf} = 2.2$ (unstable stacking fault energy for Au, $\gamma_{usf} = 92$ mJ/m^2, stacking fault energy $\gamma_{sf} = 41.6$ mJ/m^2) [162] and its low ratio $\gamma_{utf}/\gamma_{usf} = 1.09$ (unstable twin fault energy, $\gamma_{utf} = 100.6$).

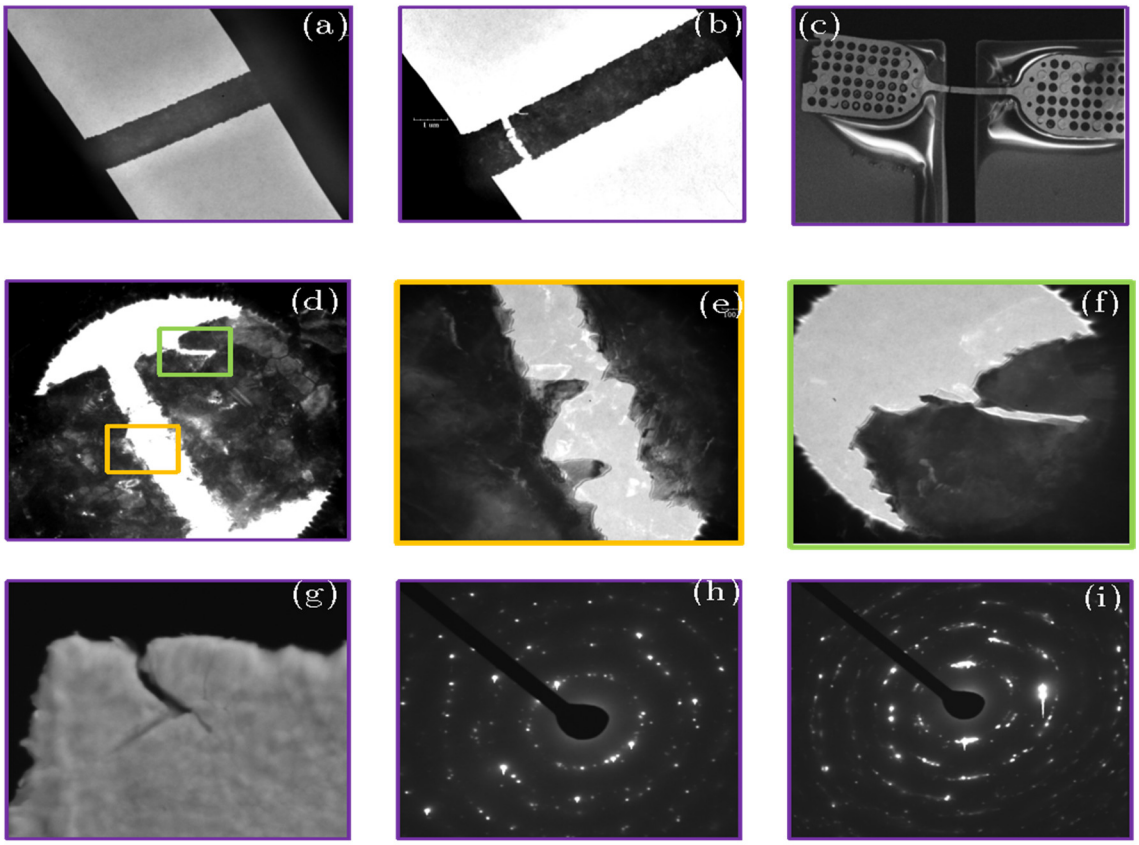

Figure 3.5 (a) Low magnification TEM image of the specimen before fatigue testing. (b) Low magnification TEM image of the same specimen after fatigue failure. (c)-(e) High magnification TEM images of the fracture surface and fatigue nanocrack. (f) SAED pattern of the specimen away from the fracture surface after fatigue testing. (g) SAED pattern of the specimen near the fracture surface after fatigue testing.

This *in situ* TEM fatigue test represents the first observation of the formation of nanoscale fatigue cracks in NC ultrathin films. A study by Kumar et al did not observe any fatigue crack formation in NC Al films (after more than 10 million cycles) under tension-tension fatigue for maximum applied strains of 0.4% (compared to ~2% strains to failure) [163]. In contrast, this Au specimen failed after less than 7000 cycles, which is likely due to the larger maximum applied strains (see Figure 3.4 (a)).

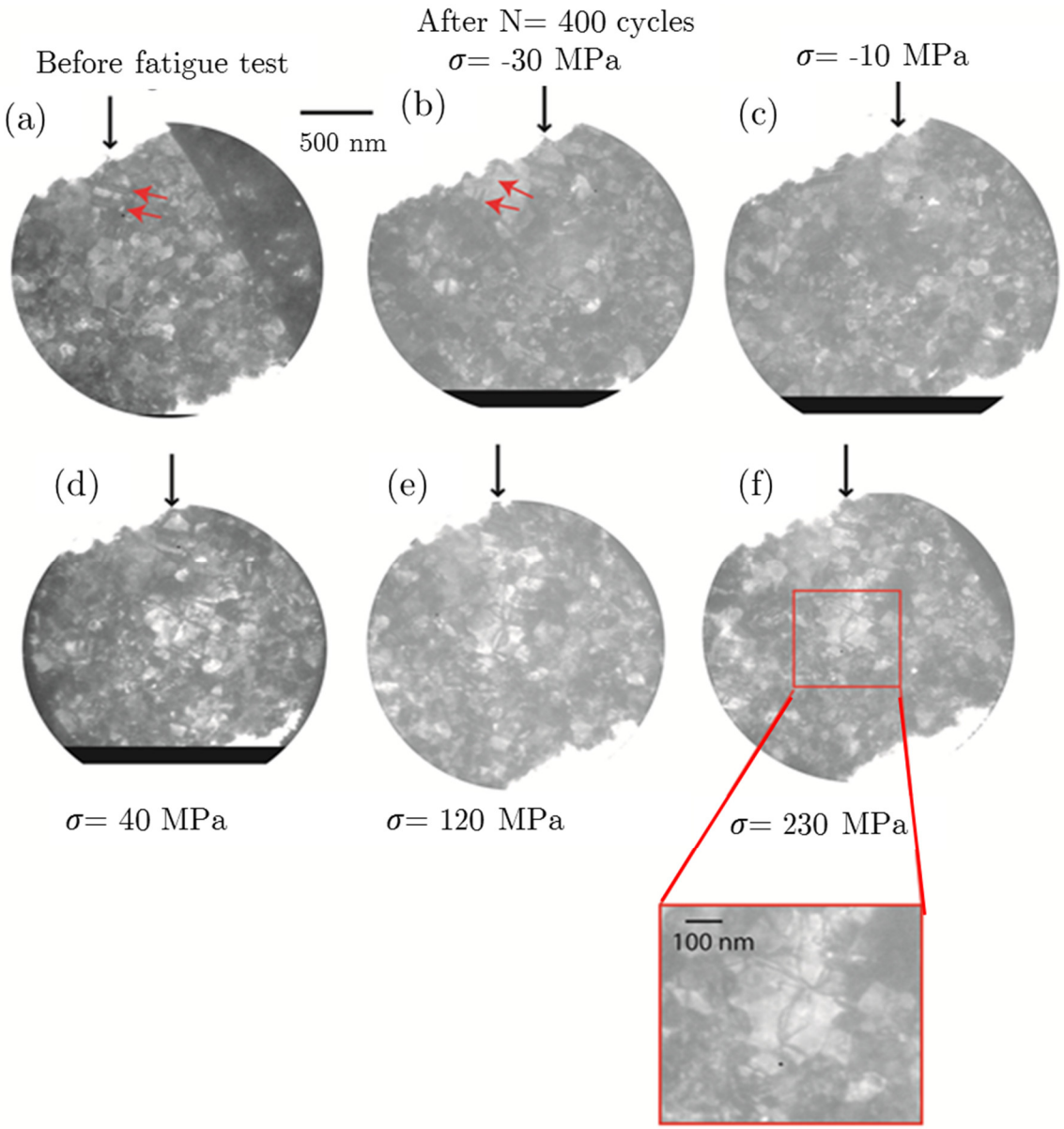

Figure 3.6 Bright field TEM images of the specimen's upper part (see Fig. 7(a)): (a) before fatigue testing. (b) After 400 cycles (σ ~-30 MPa). (c) After 400 cycles (σ = -10 MPa). (d) After 400 cycles (σ = 40 MPa). (e) After 400 cycles (σ = 120 MPa). (e) After 400 cycles (σ = 230 MPa). The black vertical arrows show the same location for all TEM images.

3.5 *Ex situ* Fatigue Test of a NC Ni Nanobeam

A fatigue test was performed on a Ni specimen (length: 14.5 μm, width: 690 nm, thickness: ~250 nm) that was manipulated and clamped with ion-beam deposited Pt inside a dual FIB/SEM microscope [144]. The test was performed in

laboratory air (*ex situ* test). The applied voltage, V_{in}, was varied from 0 to 4 V with increments of 0.2 V at a frequency of 0.006 Hz. After 2500 cycles, the test was interrupted for SEM inspection of the nanobeam. The test was then resumed at a higher frequency of 0.25 Hz. The specimen failed after N_f ~27,000 cycles. As explained in section 2.1.5.2, the change in capacitance between the two capacitive sensors located on each side of the specimen, ΔC_1–ΔC_2, was measured as a function of V_{in}, throughout the test, thereby allowing the monitoring of the specimen's response during cyclic loading. Figure 3.7(a) shows four stress-strain curves for selected cycles (N = 1, 1000, 2500, and 26,000), while Figure 3.7(b)-(d) show the evolution over the first 2500 cycles of the fatigue test of the maximum applied stress, σ_{max}, permanent strain under no applied stress, $\varepsilon_{\sigma=0}$, and E, respectively. Using the unloading portion of the stress strain curve, E was calculated to increase slightly from 120 to 140 GPa. These values are lower than the E value for bulk polycrystalline Ni (207 GPa) [164], or the value for <111> out-of-plane textured Ni films (232 GPa), [164] and lower than our previously measured E value for a similar Ni nanobeam (208 GPa) [165]. The low E values calculated in this experiment are likely the result of compliant Pt clamps. A ratcheting behavior is observed, with the maximum apparent applied strain, ε_{max}, increasing from 3.7 to 4.1% throughout the test (see Figure 3.7(a)) and a slight decrease in σ_{max} (from 2.8 to 2.6 GPa). Also, $\varepsilon_{\sigma=0}$ increases from ~0.3% to 0.7% over the first 2500 cycles. In addition, the decrease in the slope of the stress-strain curve for small strain values (see Figure 3.7(a)) is consistent with accumulation of plastic strains: as the specimen is elongated due to

plastic deformation, it undergoes buckling near the end of the unloading portion of the cycle, resulting in a lower apparent elastic slope. This result is further confirmed with SEM images of the specimen taken after 2500 cycles (see Figure 3.8). It was slightly buckled due to plastic strain accumulation and consequent compressive stress. Figure 3.8 also shows SEM images of the specimen after failure (N_f = 27,000 cycles), along with a high magnification of the fracture surface. The fracture surface occurs away from the Pt clamps and displays an intergranular crack path. In addition, the specimen overlaps by ~370 nm at the location of fracture, confirming the accumulation of plastic strains throughout the fatigue test. This value compares well with the calculated plastic overlap (based on the strain value at zero stress prior to fatigue failure) of 250 nm.

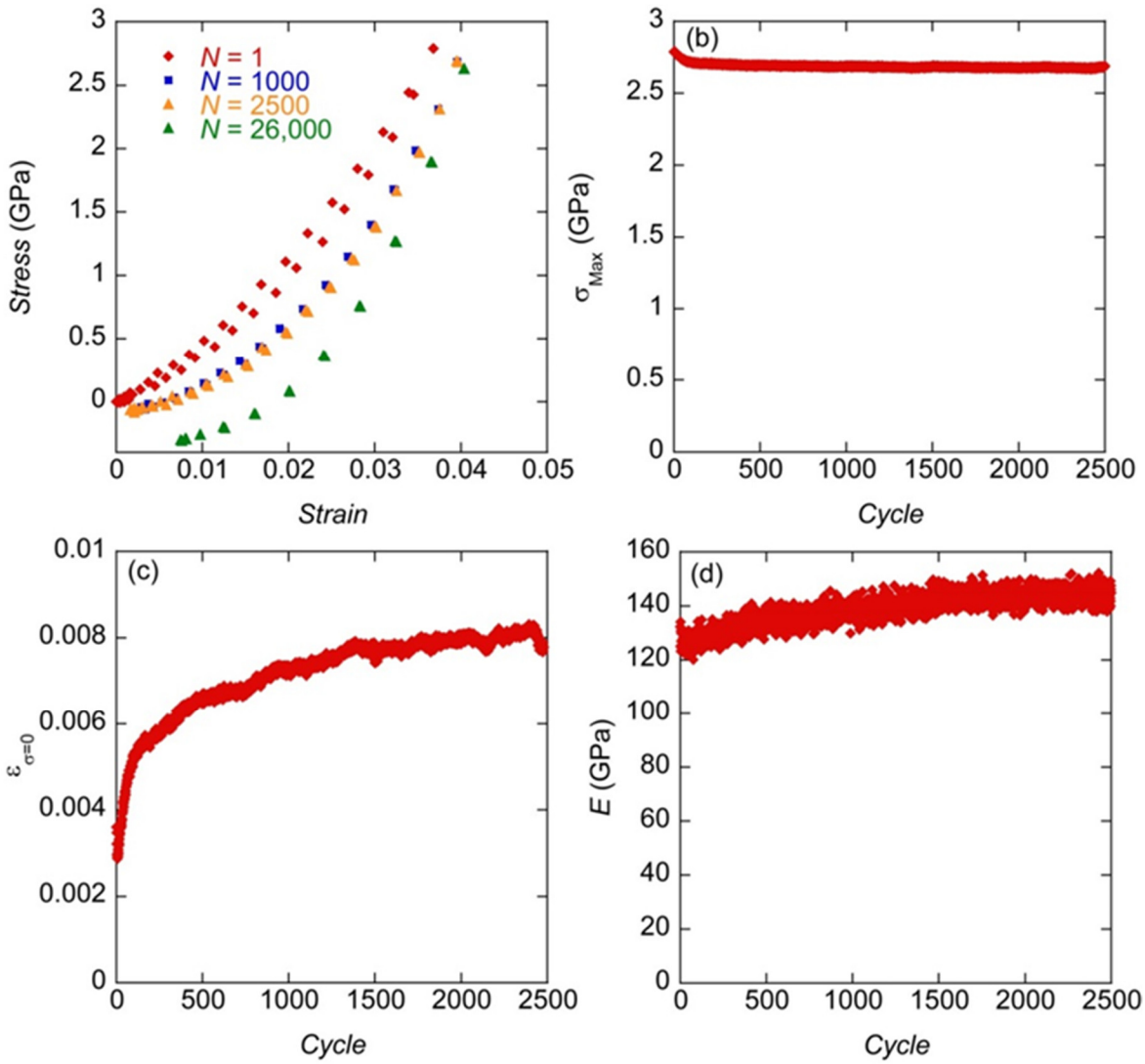

Figure 3.7 (a) Selected stress-strain curves (for loading and unloading portions of the cycles) at N = 1, 1000, 2500, and 26,000. (b) Evolution of the maximum applied stress, σ_{max}, for the first 2500 cycles. (c) Evolution of the permanent strain under no applied stress $\varepsilon_{\sigma=0}$ for the first 2500 cycles. (d) Evolution of elastic modulus, E, for the first 2500 cycles.

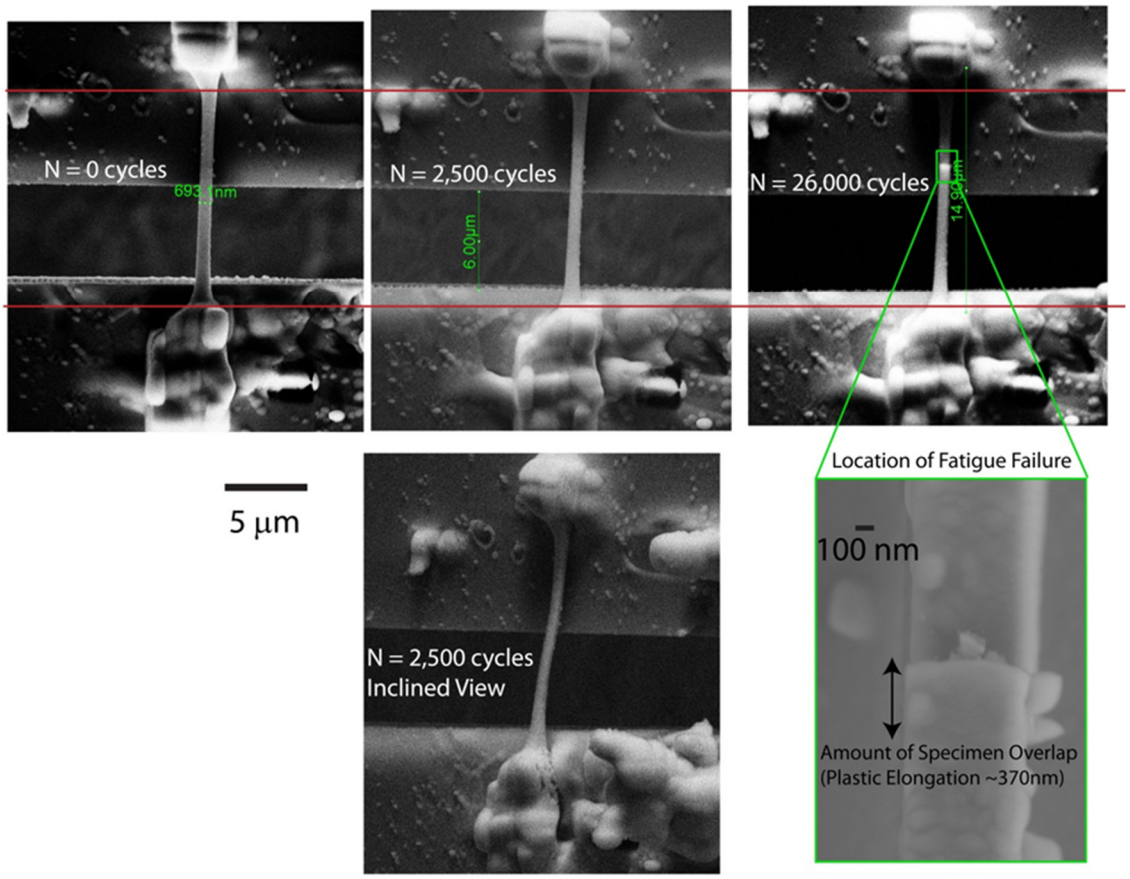

Figure 3.8 SEM images of the fatigued specimen before test, after 2500 cycles (including inclined view to show buckling effect due to accumulated plastic deformation), and after failure.

In addition to the issue of the compliant Pt clamps, the results of this fatigue test highlight some practical issues associated with the nanobeam manipulation/clamping procedure in the FIB. Specifically, Figure 3.8 clearly shows the presence of a halo of Pt coatings the entire Ni nanobeam. Also, Ga implantation damage cannot be completely eliminated during the FIB manipulation. This surface damage/modification due to the FIB manipulation can seriously affect the fatigue results and make the interpretation of the results cumbersome, which motivated the fabrication of the dog-bone shaped specimens that can be manipulated in a "FIB-less" manner (see section 2.2).

3.6 Conclusions

We employed the MEMS-based tensile testing setup to measure the monotonic and fatigue properties of ultrathin nanocrystalline Au thin film specimens. The 100-nm-thick, 1.5-μm-wide NC Au specimens have a tensile strength of ~1-1.15 GPa, and a total elongation to failure of ~2.8-5%. The specimens exhibit a ratcheting behavior under tension-tension cyclic loading in near stress-controlled conditions. Nanoscale fatigue cracks were observed after nearly 7000 cycles for σ_{max} ~0.8 GPa. It is important to note that during the fatigue tests, the unloading segment is not completely elastic and therefore plastic deformation in the unloading leads to the accumulation of cyclic damage. The quantitative *in situ* TEM technique is well suited to study the fatigue crack nucleation mechanisms in these NC ultrathin films. As evidenced with the above results, this experimental technique is well suited to investigate the fatigue properties of these NC ultrathin films, especially their fatigue crack nucleation properties. The quantitative nature of the technique allows investigation of important governing parameters on the material's fatigue response (evolution of the stress-strain curves, fatigue crack initiation lives), such as the maximum applied stresses and plastic strains, frequency, and load ratio R. Another critical aspect of the technique is its ability to perform *ex situ* fatigue tests and interrupt them with *in situ* TEM observations. Although the results of this chapter represent some advance in understanding the cyclic behavior of NC films there are still some difficulties involved on understanding fatigue response due to the large amount of ratchetting and possible fatigue-creep interactions. Therefore, stress

relaxation experiments with real time observation could help deconvolution of the time dependent and cycle dependent mechanisms.

CHAPTER IV

STRESS RELAXATION IN NC ULTRATHIN GOLD FILMS

4.1 Introduction

Fatigue tests in chapter 3 (with a load ratio $R \sim 0$) highlighted a ratcheting behavior, with in one instance fatigue failure occurring after an increase in plastic strain under no load from 1 to 2.5% [33]. This cyclic creep behavior has been observed in other NC metals, although its origin is unclear [49, 115]. In this chapter, a series of stress relaxation experiments, including *in situ* TEM stress relaxation, were performed in order to unveil the governing relaxation mechanisms under large applied stresses. MEMS-based experimental technique allowed us to clearly identify the governing primary creep mechanisms in NC metallic films. We haven't found any previous study providing such detailed understanding on this important phenomenon with parallel stress and strain measurements. Most studies either hypothesized the mechanism or infer it from measurements such as evolution of activation volume. For example, a paper by Suresh and co-workers [115], focusing on the fatigue properties in NC Ni, reports the occurrence of primary creep and its role on cyclic hardening. The authors could only speculate on the underlying mechanisms and hypothesized the exhaustion of dislocation sources at the grain

boundaries. Here, thanks to our *in situ* TEM technique, we provide a clear explanation for the observed decrease in power-law exponent, n, during our stress relaxation experiment. These observations are the first of their kinds and provide unambiguous understanding of the transient stress relaxation mechanisms in these NC films.

4.2 Stress Relaxation Results

Mechanical tests were performed on ultrathin (100 nm) NC Au nanobeams with a quantitative *in situ* TEM, MEMS-based nanomechanical testing setup (see Figure 2.24 and additional details in section 2.1.6.4). These relaxation experiments consist of keeping the actuation voltage constant across the thermal actuator, and measuring the specimen's response over time. The viscoplastic deformation of the specimen results in an increase in plastic strain which must be accompanied by a stress relaxation to keep the thermal actuator displacement constant. The evolution of the plastic strain rates as a function of stress can be calculated throughout the duration of the experiment (see section 2.1.6.4). The average grain size of the Au specimens is 75 nm, with a wide distribution of grains ranging from 20-30 nm to 200-300 nm (see Figure 2.25(d)). The measured ultimate tensile strength was ~1 GPa, with a ductility (plastic strain to failure) of ~1% (measurements performed at a strain rate of $\sim 10^{-4}$ s^{-1}).

Relaxation experiments were performed on eleven specimens (one specimen having a large pre-existing defect along the gauge length). Two specimens were tested *ex situ*, while the others were tested inside the TEM (with electronic sensing achieved

on three of them). For most specimens, several relaxation segments were carried out at increasing applied stresses, each ranging from several minutes to more than 1 day, as illustrated with the following two examples (one *in situ* TEM and one long *ex situ* test). Figure 4.1 shows the results of an *in situ* TEM test with the following loading history: 1) loading at 0.6 GPa, relaxation for 30 minutes, unloading; 2) loading at 0.8 GPa, relaxation for 20 minutes, unloading; 3) loading at 0.75 GPa, relaxation for 20 minutes, unloading; 4) loading at 0.7 GPa, relaxation for 30 minutes, unloading, and 5) loading to failure. Figure 4.1(a) shows the loading and unloading curves for the second relaxation segment, along with the evolution of plastic strain during that relaxation segment (Figure 4.1(b)). The plastic strain increases from ~1.1% to ~2.5% during the 20-minute-long relaxation segment, which is accompanied by a decrease in stress from 0.8 to 0.5 GPa. The unloading curve has a slope $E = 60$ GPa (a reasonable value for NC Au films) [92, 166], and reaches the unloaded state at ~2.4%, which is consistent with the total plastic strain accumulated at the end of the relaxation segment. Below 2.4%, the stress remains ~0, indicating buckling of the specimen (the compressive stress required for buckling is estimated at ~-20 MPa for the given specimen geometry). Figure 4.1(c) shows the loading and unloading curves for the fifth (last) relaxation segment, along with the evolution of plastic strain during that relaxation segment (Figure 4.1(d)). The accumulated plastic strain at the end of that relaxation segment is ~5.5%, which is again consistent with the unloading curve.

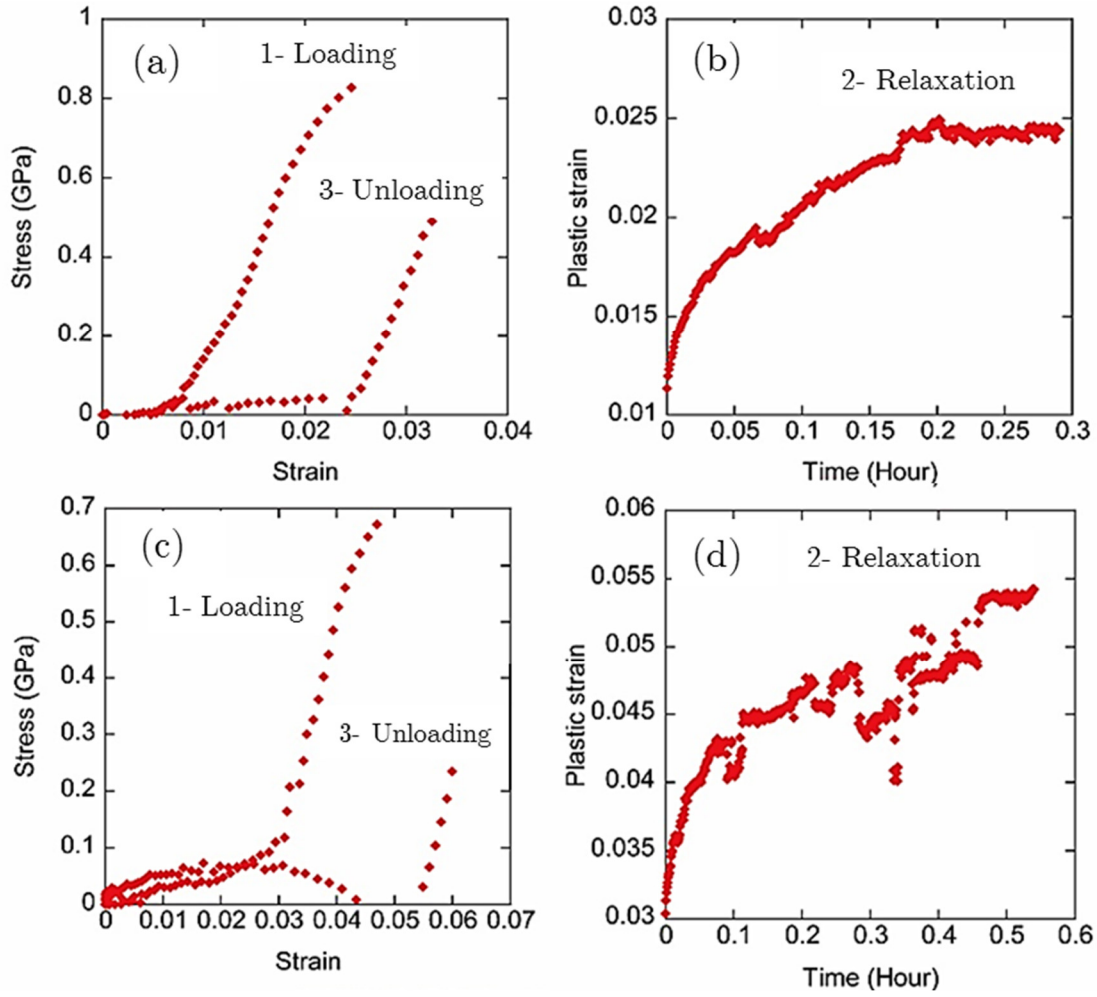

Figure 4.1 Results of an *in situ* TEM test; (a) Loading and unloading curves for the second relaxation segment (b) Evolution of plastic strain during that relaxation segment; (c) Loading and unloading curves for the fourth (last) relaxation segment (d) Evolution of plastic strain during that relaxation segment (High scattering in this plot is due to the electrical noise inside the microscope).

Figure 4.2(a)-(b) and Figure 4.2(c) show TEM images of the specimen before and after the test, respectively. These TEM images with low magnification does not show the details of microstructural evolution. However, the darker overlap region between the mating surfaces indicates the plastic stretch of the specimen, and is about 550 nm, corresponding to a ductility for that specimen of 4.6%, in good agreement with the calculated 5.5% based on the capacitance measurements. The

necking observed near the fracture surface also confirms plastic deformation of the specimen.

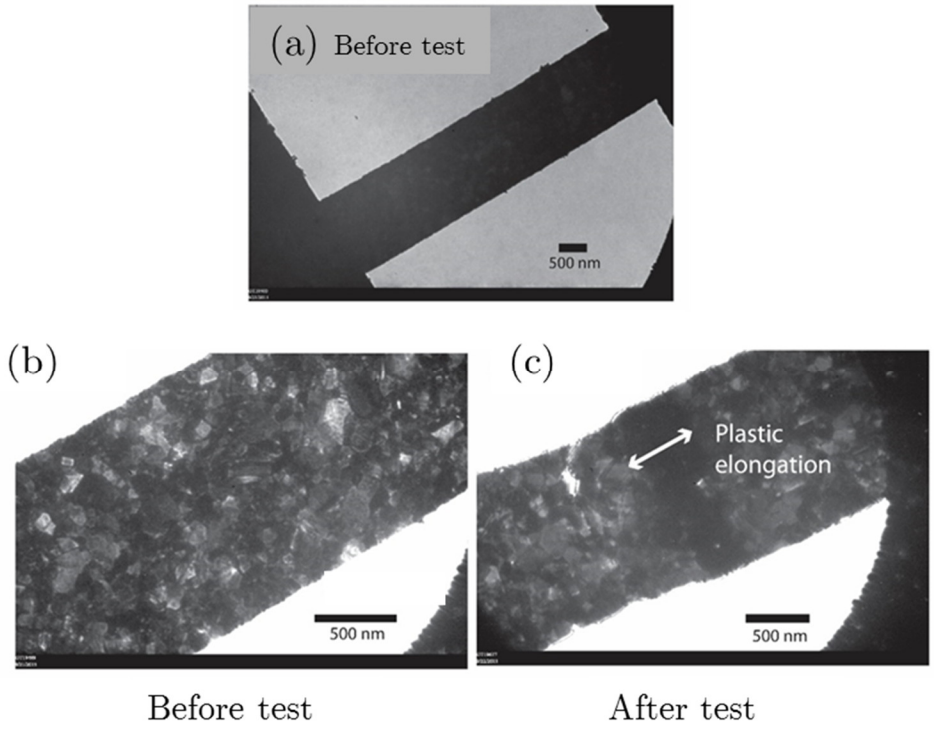

Figure 4.2 TEM images of the specimen before and after the test.

Figure 4.3 shows the results of an *ex situ* test with the following loading history: 1) loading at 0.45 GPa, relaxation for 1.5 hour, unloading; 2) loading at 0.5 GPa, relaxation for 20 hours, unloading; 3) loading at 0.275 GPa, relaxation for 6 hours, unloading; 4) loading at 0.3 GPa, relaxation for 30 minutes, unloading; and 5) loading to failure. During the fourth segment, the specimen quickly relaxed to ~0 MPa, indicative of extensive cracking. Figure 4.3(a) shows the loading and unloading curves for the third relaxation segment (left), along with the evolution of plastic strain during that relaxation segment (right). The loading curve remains at zero

stress[2] until a strain of ~4.5% as a result of the accumulated plastic strain from the previous two relaxation segments. The plastic strain increases from ~5.2 to 6.5% during that relaxation segment. The unloading curve shows a seemingly anomalous behavior with the stress reaching the minimum value of -0.125 GPa at an applied strain of 6.5%. As explained above, that minimum stress should be closer to zero due to buckling of the specimen. It is likely that this anomalous behavior results from the electrical drift (see section 2.1.6.5) over long periods of time. Nonetheless, the specimens accumulate large amounts of plastic deformation during these long *ex situ* relaxation tests, as shown in Figure 4.3(b). The significant necking observed near the fracture surface is consistent with the calculated 10% of plastic strain accumulation after the four relaxation segments for that test. The high magnification SEM image in Figure 4.3(b) shows numerous grain boundary voids near the fracture surface, suggesting grain-boundary-diffusion mediated deformation for these long relaxation tests.

[2] This artifact is similar to the example in page 94 and is the direct result of buckling in the specimen (The compressive stress came from the plastic elongation from the previous relaxation segments)

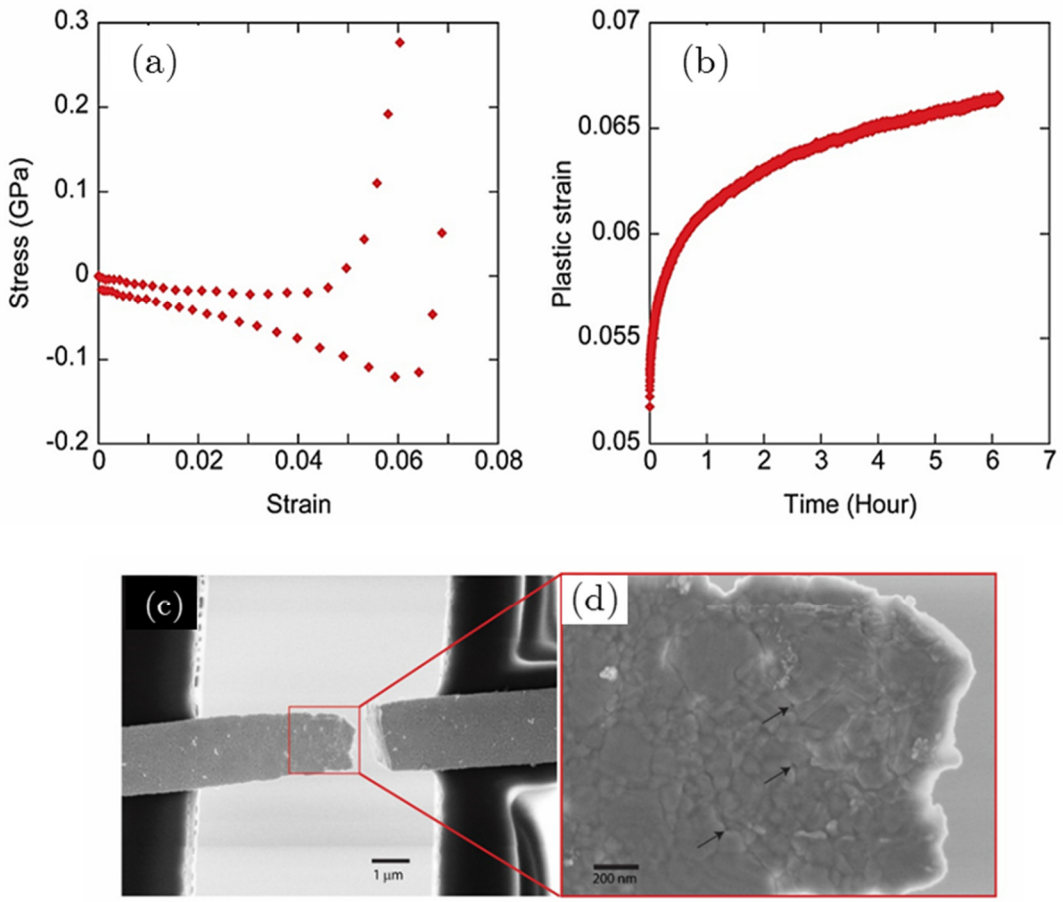

Figure 4.3 Results of *ex situ* test S1; (a) Loading and unloading curves for the third relaxation segment. (b) Evolution of plastic strain during that relaxation segment. (c) and (d) SEM image of the specimen after the specimen was ramped to failure after the relaxation segments. Arrows show preferential voiding at grain boundaries triple junctions.

Figure 4.4 shows a high magnification SEM image of another specimen relaxed for more than 30 hours (*ex situ* test). Numerous grain boundary voids, highlighted by the arrows, can also be observed.

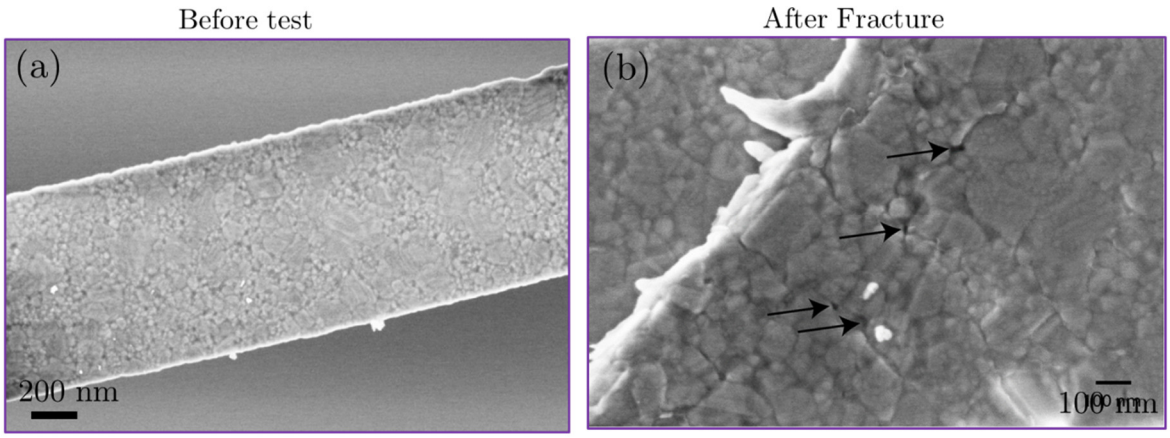

Figure 4.4 (a) Gauge length of the specimen S2 before test (b) SEM image of the same specimen, relaxed for more than 30 hours (*ex situ* test) and fractured. Arrows point at preferential voiding sites, located at grain boundaries' triple or multiple junctions.

The main results of these relaxation experiments are shown in Figure 4.5. As explained in section 2.1.6.4, fits of the evolutions of plastic strain and stress with time were used to plot the evolution of plastic strain rate, $\dot{\varepsilon}_p$, as a function of stress, σ, for all relaxation experiments for which electronic sensing was achieved. Figure 5(a) shows the results of the three *in situ* TEM specimens (two of them consisted of four relaxation segments), while Figure 4.5(b) shows the results of the two long *ex situ* specimens (four relaxation segments for the first specimen, and two for the second). S2R2 and S2R4 from Figure 4.5(a) correspond to the *in situ* TEM relaxation segments shown in Figure 4.1(a) and (b), respectively, while S1R3 from Figure 4.5(b) corresponds to the *ex situ* relaxation segment shown in Figure 3(a). Most of the relaxation segments have an initial plastic strain rate in the 10^{-4}-10^{-3} s^{-1} range. The plastic strain rates decrease down to $\sim 10^{-5}$ s^{-1} for the *in situ* TEM, short (5-30 minutes) relaxation segments, while they decrease even further for the long (several

hours) *ex situ* relaxation segments (below ~10^{-7} s^{-1}, S1R4 being an outlier given that it relaxed in a few minutes due to cracking).

The slopes of the log-log plots shown in Figure 4.5(a) and (b) correspond to the power law exponents, n, describing the creep behavior ($n = \partial \ln \dot{\varepsilon}_p / \partial \ln \sigma$), and are equal to the inverse of the strain rate sensitivity factor, m ($m = \partial \ln \sigma / \partial \ln \dot{\varepsilon}_p = 1/n$). The slopes n are therefore indicative of the governing viscoplastic deformation mechanisms during relaxation. Figure 4.5(c) and (d) show the evolution of the exponent n as a function of time during the corresponding relaxation segments shown in Figure 4.5(a) and (b), respectively. For the long *ex situ* relaxation tests (see Figure 4.5(d)), n continuously decreases from initial large values (n from 6 to 14 at $t = 0$) to low n values (n ~1-2) after several hours. The inset in Figure 5(d) shows that n decreases down to ~4-5 after 30 minutes, which is consistent with the short *in situ* TEM relaxation segments (see Figure 4.5(c)).

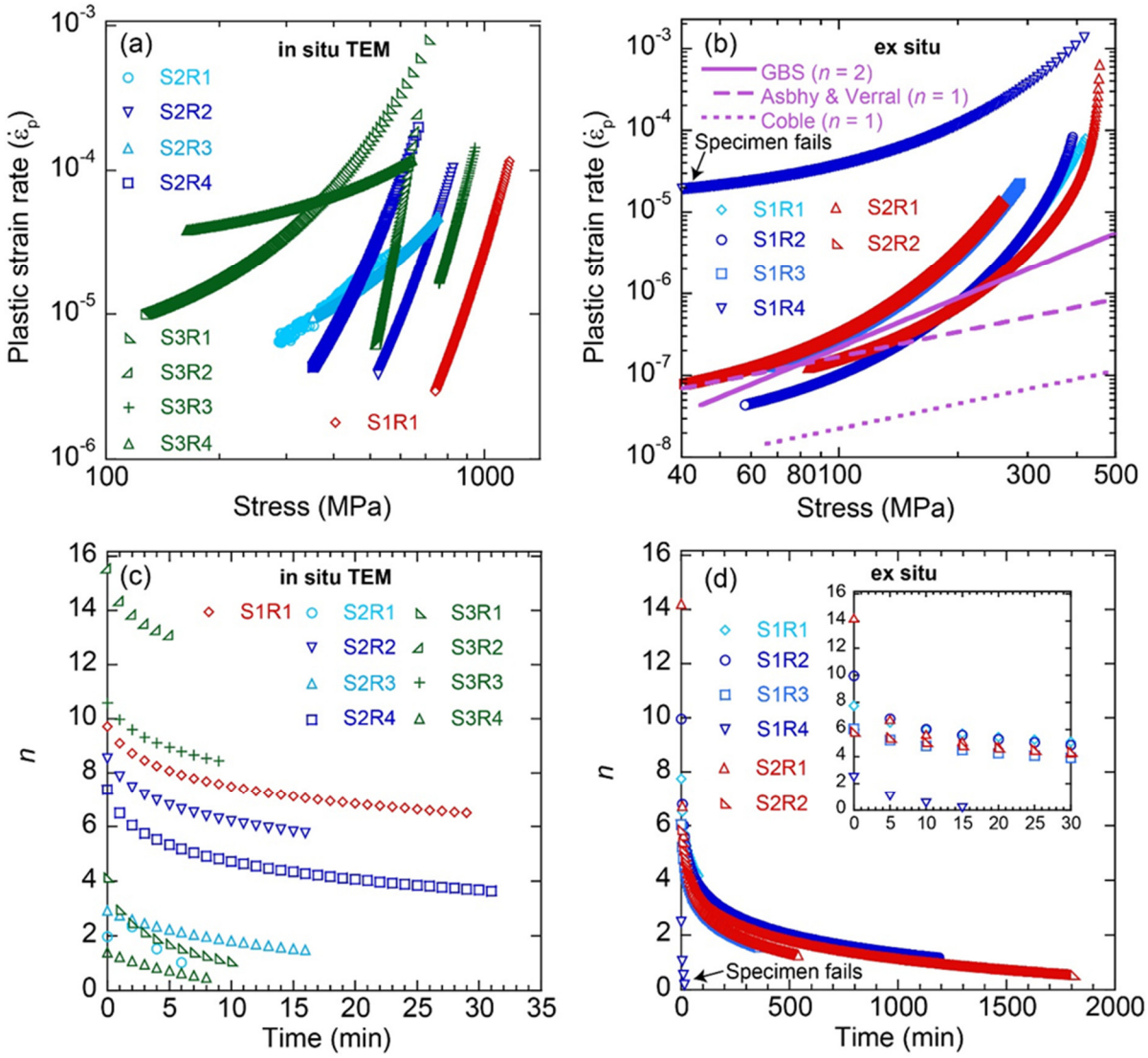

Figure 4.5 (a) and (b) Evolution of plastic strain rate as a function of stress for all relaxation segments, *in situ* TEM and *ex situ*, respectively. (c) and (d) Corresponding evolution of power exponent n with time.

The observed change of the n exponent over time indicates a transition in the dominant relaxation deformation mechanisms, from dislocation-mediated ($n > 4$; see *in situ* TEM observations below to explain the evolution of n over the first 30 minutes of the relaxation segments) towards deformation mechanisms based on diffusion ($n \sim$1-2) after several hours. The low strain rate regime (measured plastic strain rates $<10^{-6}$ s^{-1}) obtained after several hours of relaxation for the *ex situ* tests

is indeed commensurate with the following three mechanisms, as shown in Figure 4.5(b): grain boundary sliding controlled by grain boundary diffusion (GBS) [167], Coble creep (intergranular creep) [168], and the Asbhy-Verral mechanism [132] (another grain boundary sliding mechanism accommodated by diffusional flow); see Appendix A for Equations (8-1)-(8-3) and Table 8.1 [166] ($n = 2$ for GBS, and $n = 1$ for Coble creep and Ashby-Verral). Based on the uncertainties in the values of the numerous parameters in these equations, and the limited available experimental data, it is not possible to identify which specific mechanism is operative. However, post-mortem SEM images of the long *ex situ* tests (see Figure 4.3(b) and Figure 4.4) and a 48-hour-long *in situ* TEM relaxation experiment (see Figure 4.6) clearly reveal the formation of numerous voids along the grain boundaries, thereby confirming the occurrence of mechanisms based on grain boundary diffusion.

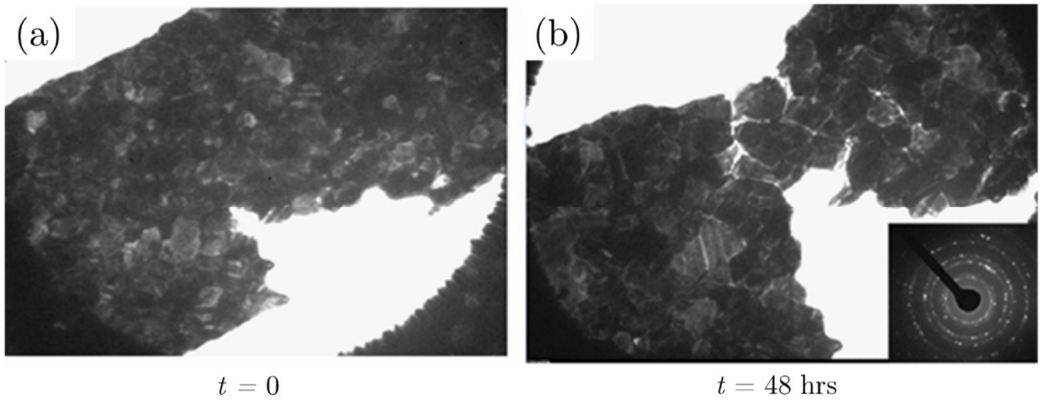

Figure 4.6 Evolution of microstructure and crack advance ahead of a pre-existing defect for a 2-day-long stress relaxation experiment performed inside the TEM. (a) Beginning of the test (b) After 48-hour stress relaxation. Numerous voids along the grain boundaries can be observed at $t = 48$ hours.

4.3 *In situ* TEM Observations during Stress Relaxation

In order to unveil the governing mechanisms responsible for the evolution of n over the first ~30 minutes of the relaxation segments, a series of *in situ* TEM stress relaxation tests were performed on 5 specimens, with videos recording the microstructural evolution during the entire length of the experiments (a few hours for each specimen). The electronic sensing was not operational during these *in situ* TEM tests (instead, stress and strain were intermittently measured based on TEM images, see 2.1.6.2). However similar relaxation results as shown in Figure 4.5 are expected given that the setup for these experiments was identical. Overall, the deformation was highly localized, leading to significant necking along the specimen's gauge length. Infrequent signs of grain growth were observed (disappearance of a few small grains; see Figure 4.7 which presents sequential snapshots from a movie recording at the beginning of a relaxation segment). Instead the stress relaxation segments were associated with inter- and intra-granular dislocations activities,

localized within or between a few grains only. This activity slowed down within a time scale of tens of minutes, as described in more details below for 2 specimens.

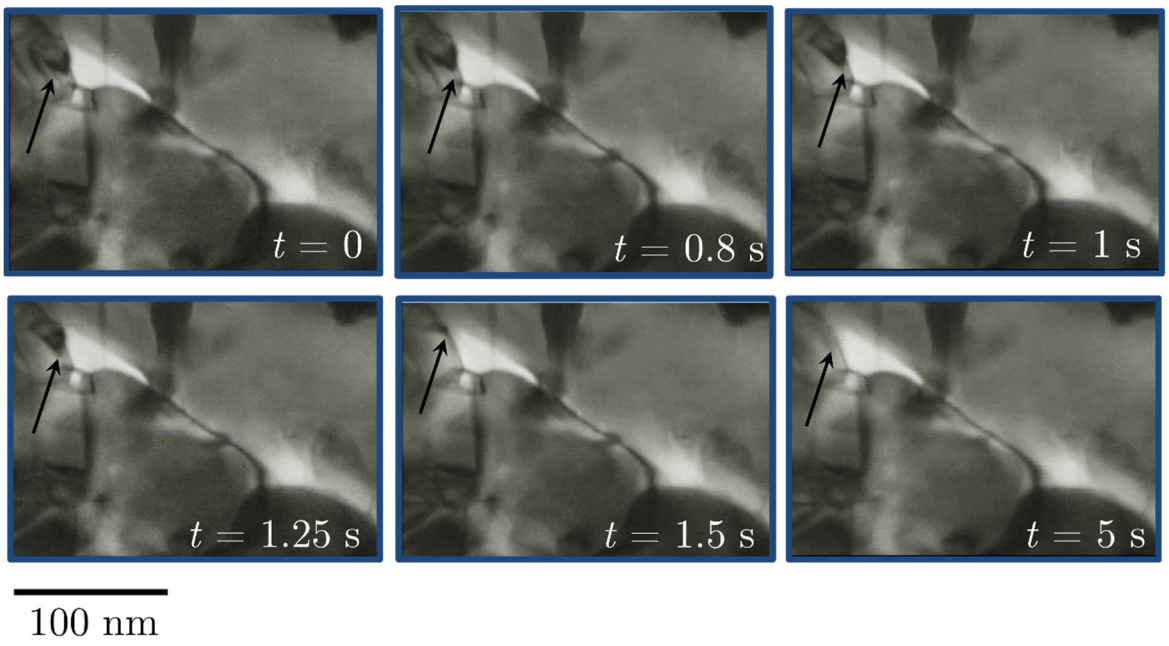

Figure 4.7 Snapshots extracted from a video[3] of a deforming specimen where there is a direct evidence of GB migration. The black arrow shows the disapperance of a small grain over time.

Specimen 1 underwent a series of 15 stress relaxation segments, each ranging between 2 and 12 minutes (total duration ~75 minutes). The first stress relaxation segment was performed at an applied strain < 1-2% (microplastic regime, in the beginning of relaxation in which dislocation activities can be observed in a few grains), while the last 5 relaxation segments were performed at applied strains above 16.7% with several intergranular cracks present in the gauge section. This applied strain is about ten times larger than the monotonic plastic strain to failure (~1%), due to these successive relaxation segments during which transient relaxation

[3] The movie could be found in online version of our paper [169] E. Hosseinian, M. Legros, O.N. Pierron, Quantifying and observing viscoplasticity at the nanoscale: highly localized deformation mechanisms in ultrathin nanocrystalline gold films, Nanoscale, 8(2016) 9234-44.

deformation is activated. From the very first relaxation segment, intergranular dislocation activities were observed along a large angle grain boundary (see Figure 4.13 in section 4.4 for orientation analysis) that is ~220 nm long and located in the center of the gauge section (corresponding to the *G1/G2* interface in Figure 4.9(a)). The orientation of the GB with respect to the loading direction (here 35°) is an important factor for strain localization. The grain boundary dislocations appear to nucleate at the triple junction delimiting the top of the boundary (see TJ in Figure 4.9(a)) and are observed during all relaxation segments (see Figure 4.8 for a later segment, where dislocations are seen to flow rapidly along the grain boundary). The shear along the *G1/G3* interface reaches 120 nm after 45 minutes, which corresponds to more than 55% of the grain size *G1* along this interface (and the passage of about 400 dislocations with a primary Burgers vector a/2<110>), further underlying the high strain concentration carried out by this mechanism. The strain incompatibility generated at triple junctions leads to the voiding observed in Figure 4.3 and Figure 4.4. Note that, in contrast, the shape change of both grains remains much smaller than the shear strain accommodated at the *G1/G2* interface and that only a few other locations carried some plastic deformation, based on either intergranular or transgranular dislocation motion; a few intergranular dislocations moving along the *G1/G3* grain boundary interface (see Figure 4.9(a)). The frequency/speed of these grain boundary dislocations moving along that boundary clearly decreased with time during a stress relaxation segment.

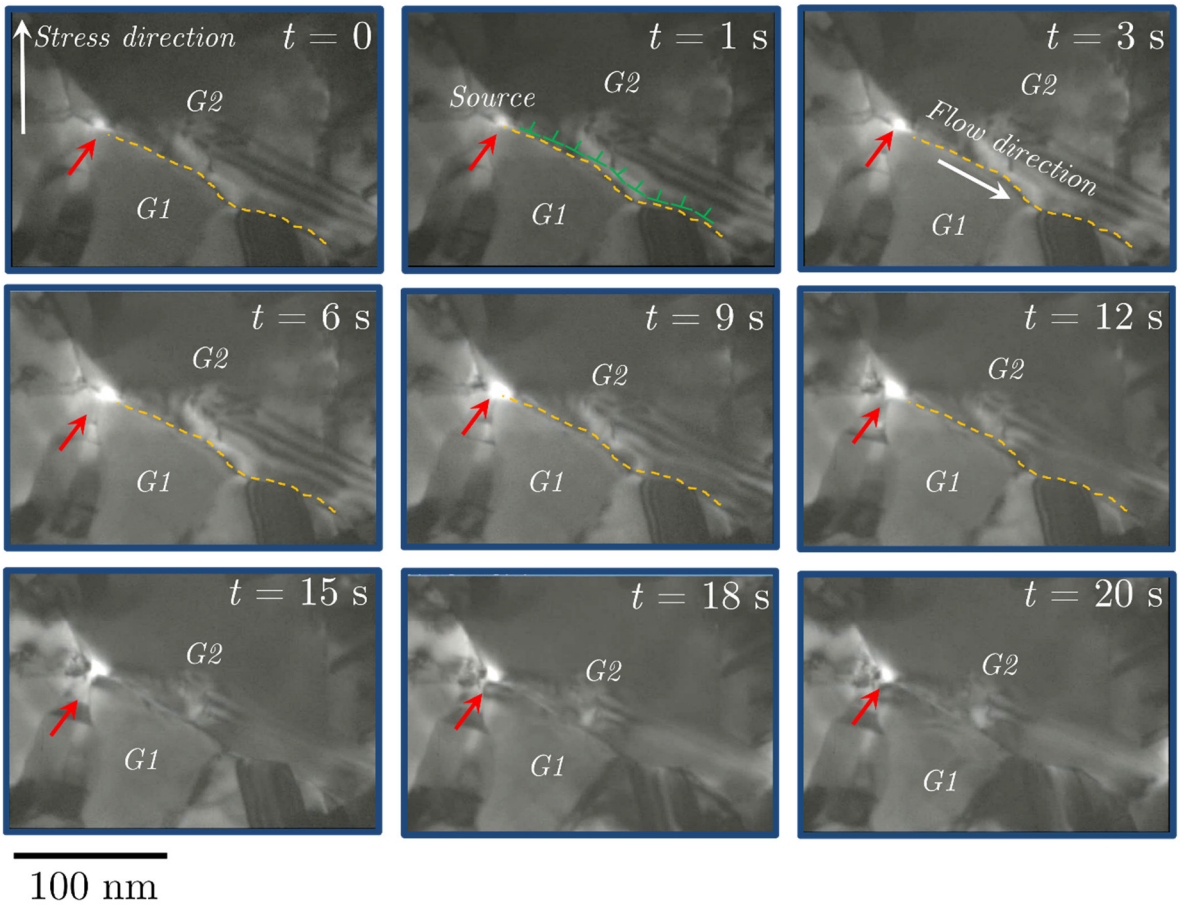

Figure 4.8 Snapshots extracted from a video[4] of deforming gold specimen 1 where there is a direct evidence of rapid GB dislocation flow where dislocations are observed to traverse along the grain boundary

The observed decrease in n over the first few minutes of each relaxation segment (see Figure 4.5(c) and (d)) and the accompanying decrease in plastic strain rate therefore likely results from the slowing down of these dislocation activities. As illustrated in Figure 4.14(a), the shear deformation carried out at the interface over the time period of 8 minutes amounts to 30 nm (3D nature of the sample is neglected here), which is ~13% of the *G1/G2* interface length. As stated above, the overall shear deformation carried out at the interface over a time period of 45 minutes

[4] The movie could be found in online version of our paper [169] ibid.

(consisting of several relaxation segments) amounts to 120 nm, which is ~55% of *G1/G2* interface length, and 70 nm in the loading direction. It is interesting to note that this intergranular shear does not concern the smaller grains (*G1* is about 200 nm large and *G2* more than twice larger), but an interface that is planar and adequately oriented with respect to the loading axis.

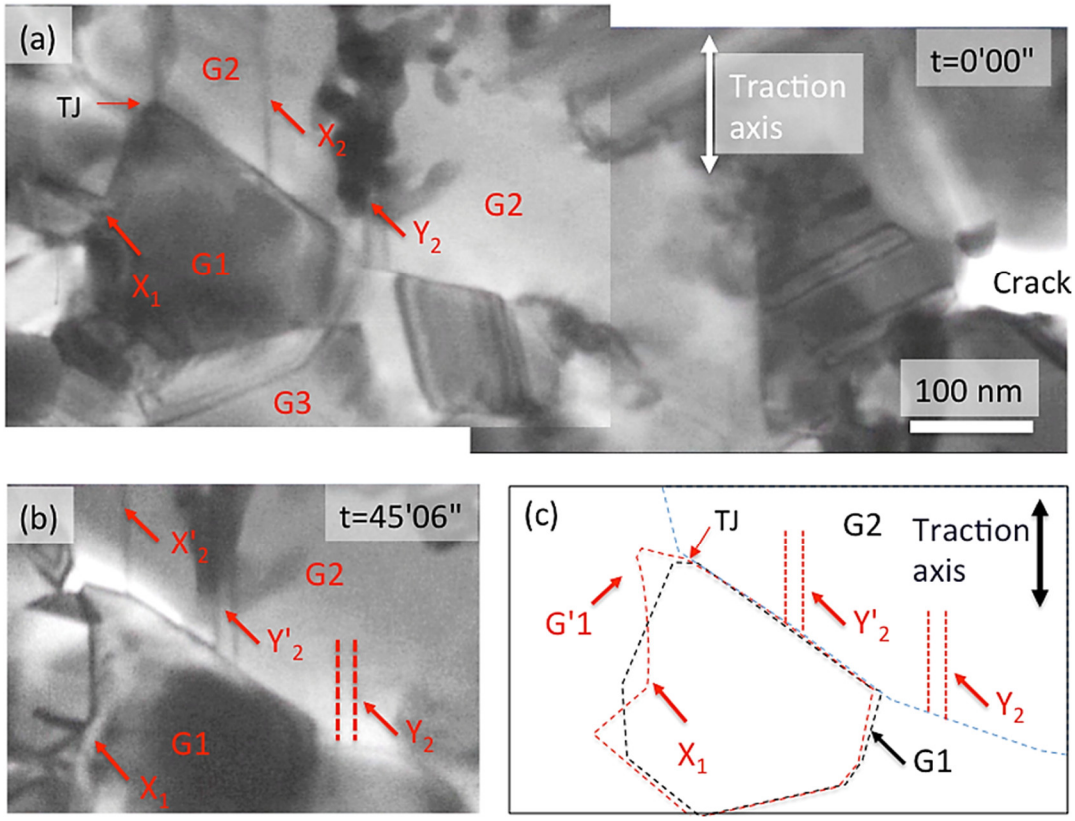

Figure 4.9 (a,b) Snapshots extracted from a video of a deforming specimen (specimen 1; see text) where the deformation concentrates between grain 1 and 2 (*G1* and *G2*). X2 and Y2 are fixed points in *G2* (i.e., the difference in location between X2, Y2 ($t = 0$) and X2', Y2' ($t = 45$ minutes) indicates the interface shear deformation); (c) Sketch of the shape of the grain 1 before (*G1*) and after (*G2*) deformation. Note that most of the grain shape distortion happens at triple junctions but that this distortion is much smaller than the shear accommodated at the *G1/G2* interface, that can be measured through the displacement of X2 and Y2 markers (immobile stacking faults in *G2*).

Specimen 2 also underwent a series of 15 stress relaxation segments, each ranging between 3 and 18 minutes (total duration ~100 minutes). The stress was measured at a few instances using TEM images of the 2nd capacitive sensor

connected to the load sensor (see Figure 2.18 in section 2.1.6.2). During the second relaxation segment (measured stress ~380 MPa), some dislocations are observed to traverse grains and/or exit the crystal at the surface as seen in Figure 4.10. During the third relaxation segment, a sustained slip band of dislocations in a (111) plane (see Figure 4.15 in section 4.4) is observed in a large grain (~300 nm; see grain *G4* in Figure 4.12). The slip band is oriented ~30^{o} with respect to the loading axis. The dislocations are nucleated at the top left grain boundary (at the triple junction location, TJ) and are absorbed in the bottom boundary (see Figure 4.12).

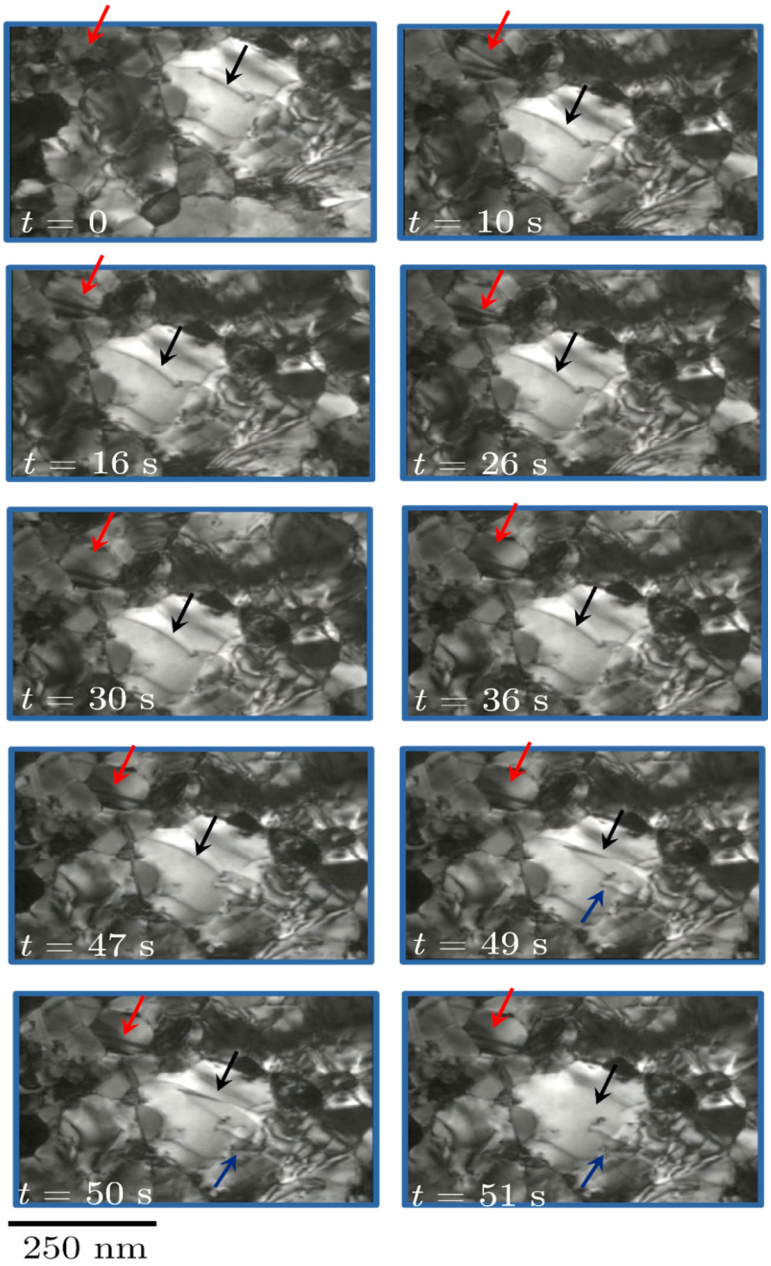

Figure 4.10 Snapshots extracted from a video[5] of a deforming gold specimen where there is a direct evidence of intragranular dislocation plasticity where some dislocations are observed to traverse grains and/or exit the crystal at the surface

[5] The movie could be found in online version of our paper [169] ibid.

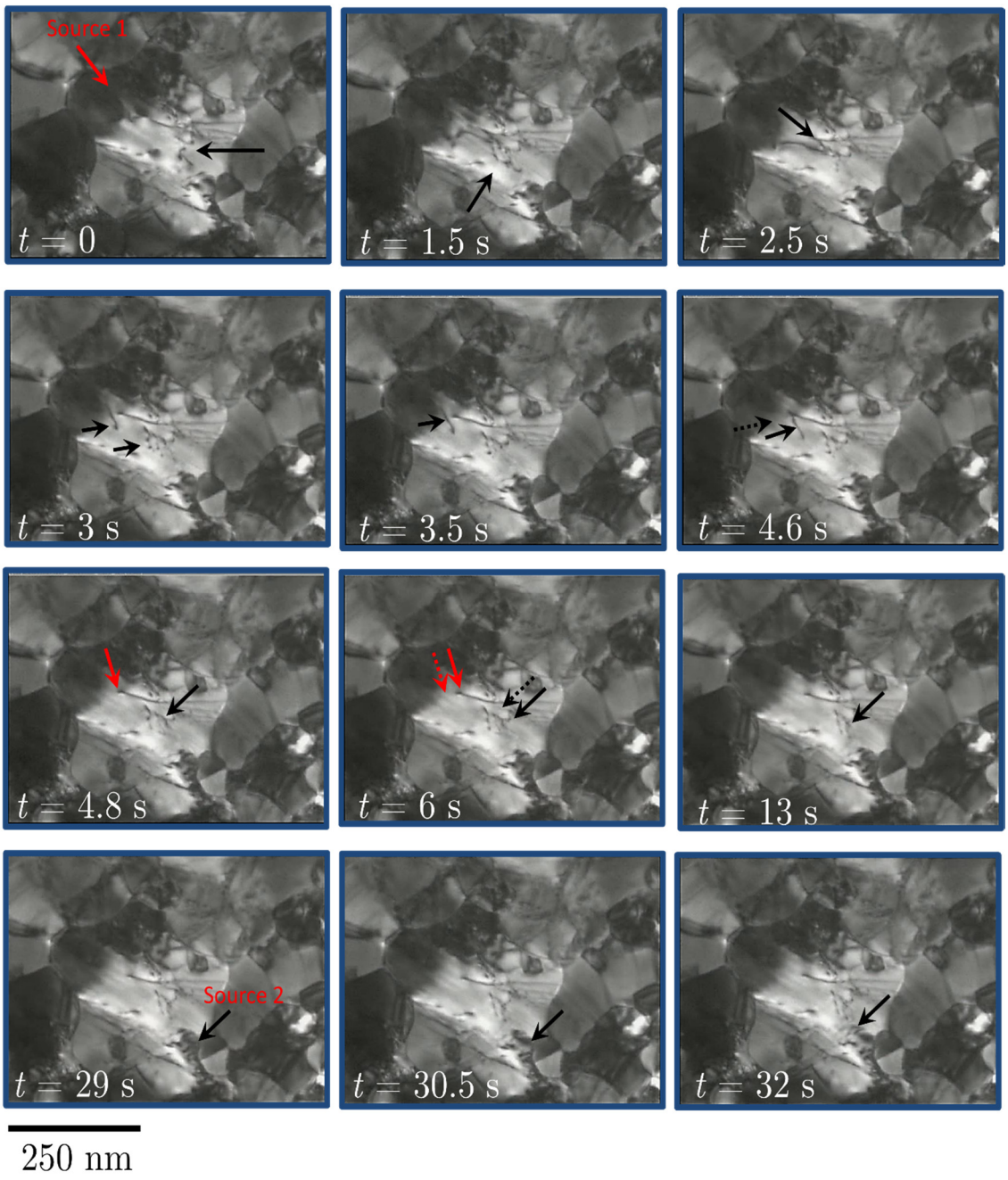

Figure 4.11 Snapshots extracted from a video[6] of a deforming specimen (specimen 2; see text). The dislocations are nucleated at the top left grain boundary and are absorbed in the bottom boundary. At $t = 29$ s, a different pile-up, nucleating at the bottom boundary becomes active.

Additional dislocation activities are observed in the upper part of the grain as well as in adjacent grains. After 8 minutes, these activities have slowed down

[6] The movie could be found in online version of our paper [169] ibid.

significantly, although the dislocation pile-up is still active. Figure 4.12 shows that the triple point moved by ~25 nm after 15 minutes into that relaxation segment. Assuming a $[10\bar{1}]$ Burger's vector in the $(\bar{1}\bar{1}\bar{1})$ activated slip plane (highest Schmid factor: 0.44; see Figure 4.15 in section 4.4), approximately 87 dislocations would be required to produce this shear, which appears consistent with the observed 45 dislocations traversing the grain over the first 3 minutes (when the dislocations are most active). An overview of the entire specimen's gauge section towards the end of this relaxation segment (18 minutes) shows that the relaxation appears to be limited to these few grains, which results in a pronounced necking forming at that particular location. Failure of the specimen occurs when these localized events connects to external cracks (as seen in the right of Figure 4.9(a)) A different pile-up, nucleating at the bottom boundary (close to where the previous pile-up was being absorbed) becomes active at the end of the third relaxation segment and at the beginning of the fourth segment (applied stress ~715 MPa), and remain active throughout the rest of the experiment, suggesting that the initial dislocation source at the triple point has become exhausted as a result of the deformation and stress decrease occurring during the third relaxation segment (see Figure 4.11).

These *in situ* TEM observations suggest that the decrease in n during a relaxation segment from large, initial values ($n > 4$) down to low values (n ~1-2) after several hours (Figure 4.5(d)) is the consequence of these dislocation activities that slow down or stop in the event of dislocation source exhaustion (as in the case of specimen 2), after which diffusion-based deformation becomes dominant.

The observations also clearly reveal that most of the dislocation sources are robust enough to produce additional dislocations upon increasing of the applied stress, which leads to a sudden increase in n as shown with the relaxation experiments consisting of several relaxation segments.

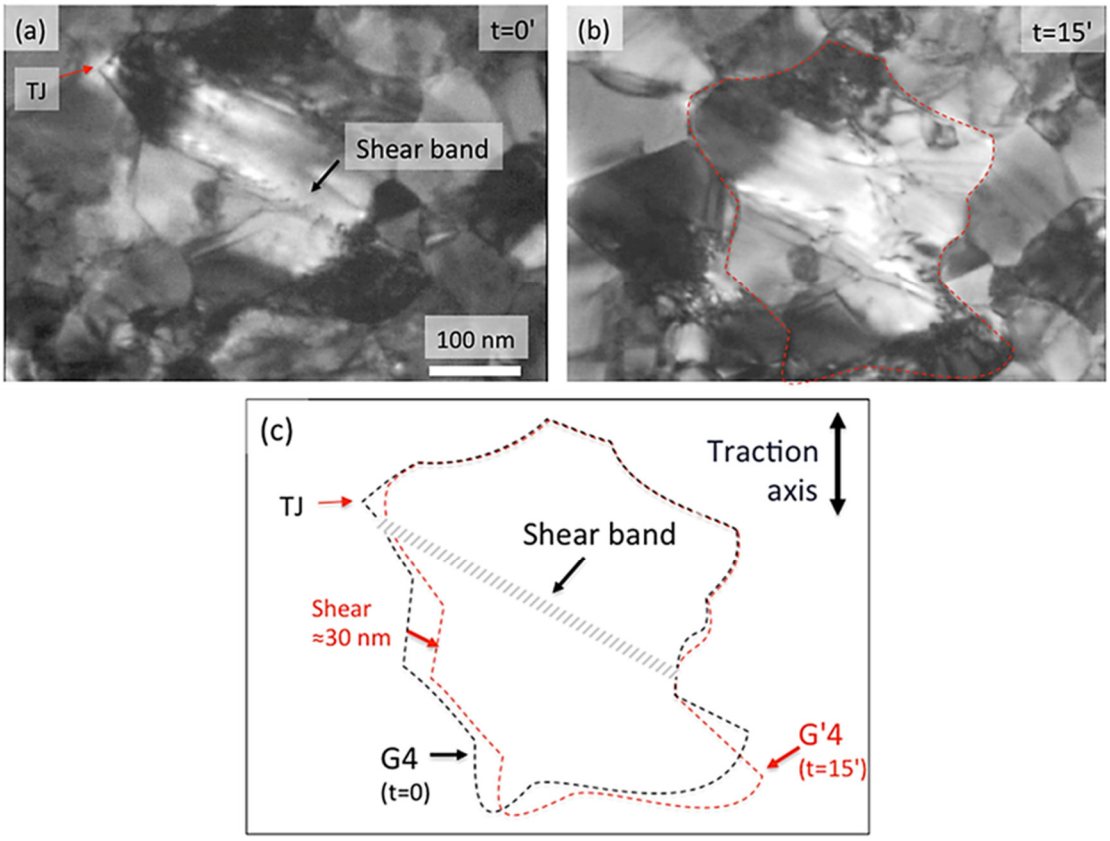

Figure 4.12 (a,b) Snapshots extracted from a video of a deforming specimen (specimen 2; see text) where the deformation concentrates within a slip band in a large grain labeled *G4*. (c) Sketch of the intragranular shear (≈ 30 nm) imposed by the shear band on the (111) plane between the upper and lower part of *G4*. *G4* and *G'4* indicate the shape of the grain before and after shear, respectively.

4.4 Grain Orientation for *In situ* TEM Experiments

Figure 4.13 represents the stereographic projection corresponding to grains *G1* and *G2* in Figure 4.9. The sheared grain boundary corresponds to the (111) plane of *G2* and the $(\bar{1}\bar{1}\bar{1})$ plane in *G1* (bold line in Figure 4.13). The markers X and Y in Figure 4.9 are probably stacking faults or nanotwins oriented along $(\bar{1}\bar{1}1)$ in *G2*.

They remain immobile and mostly unaffected by the plastic deformation that occurs along the *G1/G2*. This makes them relevant to serve as markers for local strain measurement. Figure 4.12(a)-(b), taken 45 minutes apart with the same imaging conditions, show that despite the large strain experienced at the *G1* and *G2* interface, X2 and Y2 did not change neither in direction or width. The apparent change in contrast observed on these markers in Figure 4.14 is due to a slight tilt of the TEM straining holder during the experiment, a common maneuver, frequently repeated to adjust the contrast of a deforming sample. The direction of the tensile axis is vertical in Figure 4.9, Figure 4.12 and Figure 4.14.

Figure 4.15 represents the stereographic projection corresponding to the grain sheared by intragranular dislocations along the $(\bar{1}\,\bar{1}\,\bar{1})$ plane in Figure 4.12. Note that in both cases (Figure 4.9 and Figure 4.12), the localized shear occurs along a plane close to the maximum shear with respect to the tensile axis. In Figure 4.12, the most probable Burgers vector $a/2\{\bar{1}\,0\,1\}$ leads to a Schmid factor of 0.44.

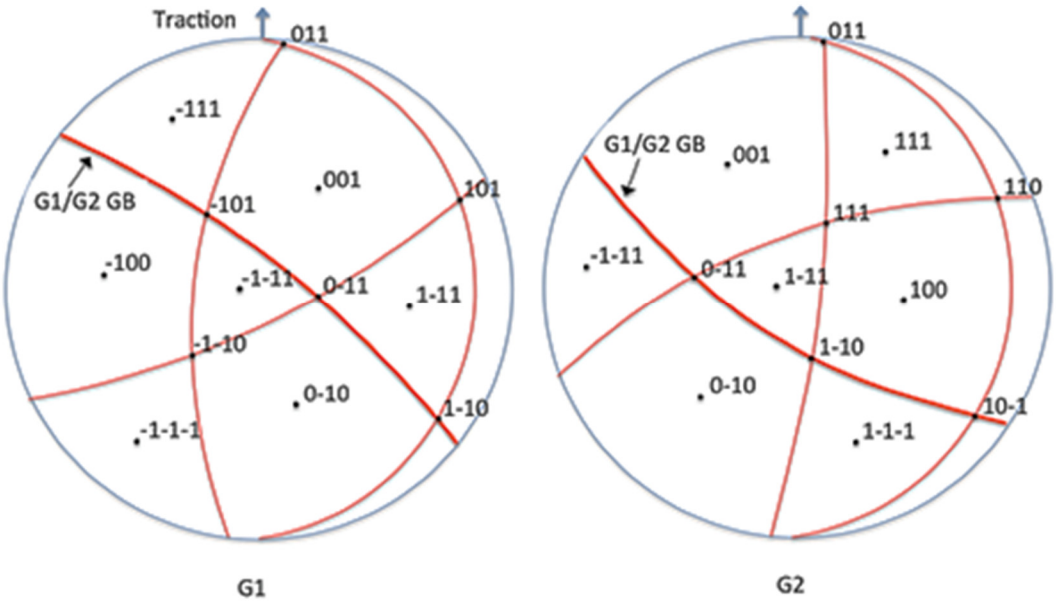

Figure 4.13 Stereographic projections of *G1* and *G2* grains in Figure 4.9(a).

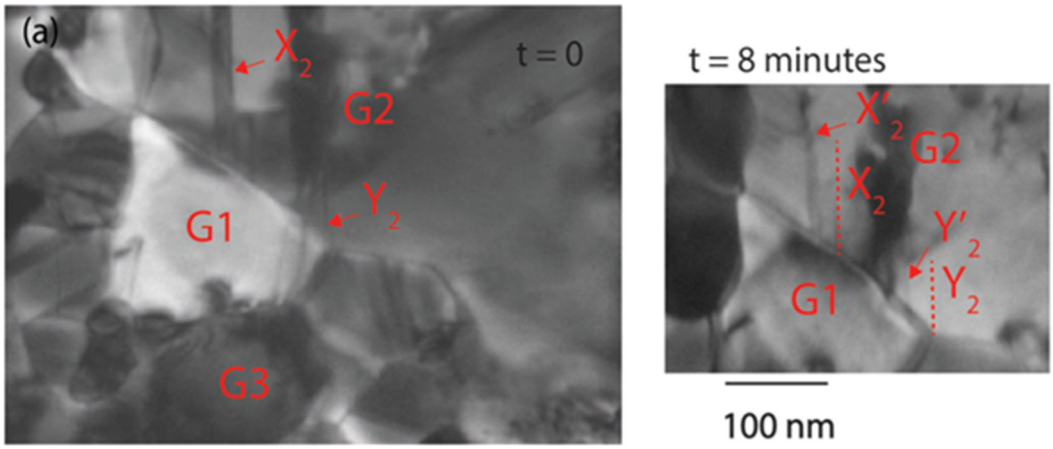

Figure 4.14 Intergranular shear between grains *G1* and *G2* after 8 min relaxation. The shear measured along the *G1/G2* interface is at least 30 nm (Neglecting 3D effects as the image is a projected picture of the grains). X2 and Y2 are fixed markers (immobile stacking faults in grain *G2*).

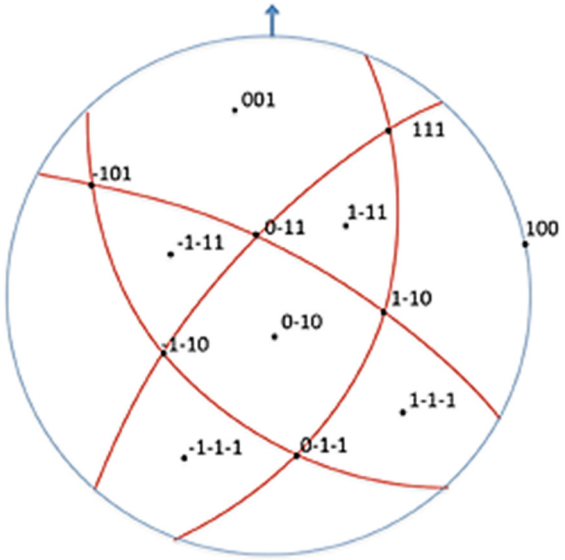

Figure 4.15 Stereographic projection of the grain sheared by intragranular dislocations in Figure 4.12(b).

4.5 Conclusion

In conclusion, this chapter unveils the stress relaxation transient deformation mechanisms in NC metals, thanks to a robust quantitative *in situ* TEM MEMS nanomechanical testing approach to quantify stress relaxation and to perform *in situ* observations of time-dependent deformation in ultrathin NC films. Upon successive relaxation segments, the power-law exponent n continuously decreases from initial large values (n from 6 to 14 at $t = 0$) to low values (n ~1-2) if the test is long enough (several hours). The *in situ* TEM results show that the transient relaxation behavior under large stresses is accommodated by sustained dislocation motion, either intergranular or transgranular, only in a few grains (the larger grains (above ~200 nm) that are favorably oriented for maximum shear (main glide plane or grain boundary orientation close to 45°)), which could only be observed with a technique like *in situ* TEM. Over time, the dislocation sources, located in or close to grain

boundary and triple junctions, become less operative as a result of the decrease in applied stress, or ceased to operate (as in the case of specimen 2), likely leading to a transition to a grain-boundary-diffusion based mechanism. However, most of these sources are robust enough to produce additional dislocations upon increase of the applied stress, contributing to significantly larger ductility than for monotonic tests by maintaining localized shear regions. The results also highlight a promising technique for nanoscale characterization of time-dependent deformation.

CHAPTER V

CRACK GROWTH MECHANISMS IN NC ULTRATHIN FILMS

As mentioned in section 1.4.4, crack growth in thin films no longer follows the classic mechanisms, observed in bulk metals when film thickness decreases to 100 nm and below. This chapter presents the results of *in situ* TEM stress relaxation tests on NC gold films to study the crack growth behavior. We highlight a new intergranular crack growth mechanism that relies on GB dislocations. The results show that this mechanism only operates with large grains (>200 nm), by comparing crack growth processes in two different Au films with different average grain sizes. These direct observations and comparisons improve understanding of the crack growth mechanisms in NC metallic films.

5.1 Crack Growth in 30-nm-thick Au Specimens

One 30-nm-thick Au specimen was tested inside the TEM. The test consisted of twelve successive holds at constant displacements X_A, increasing from 250 nm (V_{in} = 1.5 V)[7] to 460 nm (V_{in} = 2.2 V) nm, each hold lasting up to 10 minutes. Figure

[7] X_A values are approximated using Eq.(2-8). Values of K_s = 2035 N/m and 610 N/m were used for 100 nm and 30 nm-thick films, respectively. Sensing was not operational for the experiments in this chapter.

5.1(a)-(b) shows the specimen's gauge length before and after the test: an intergranular crack propagated from the right edge through the entire specimen's width, along a plane roughly perpendicular to the loading axis.

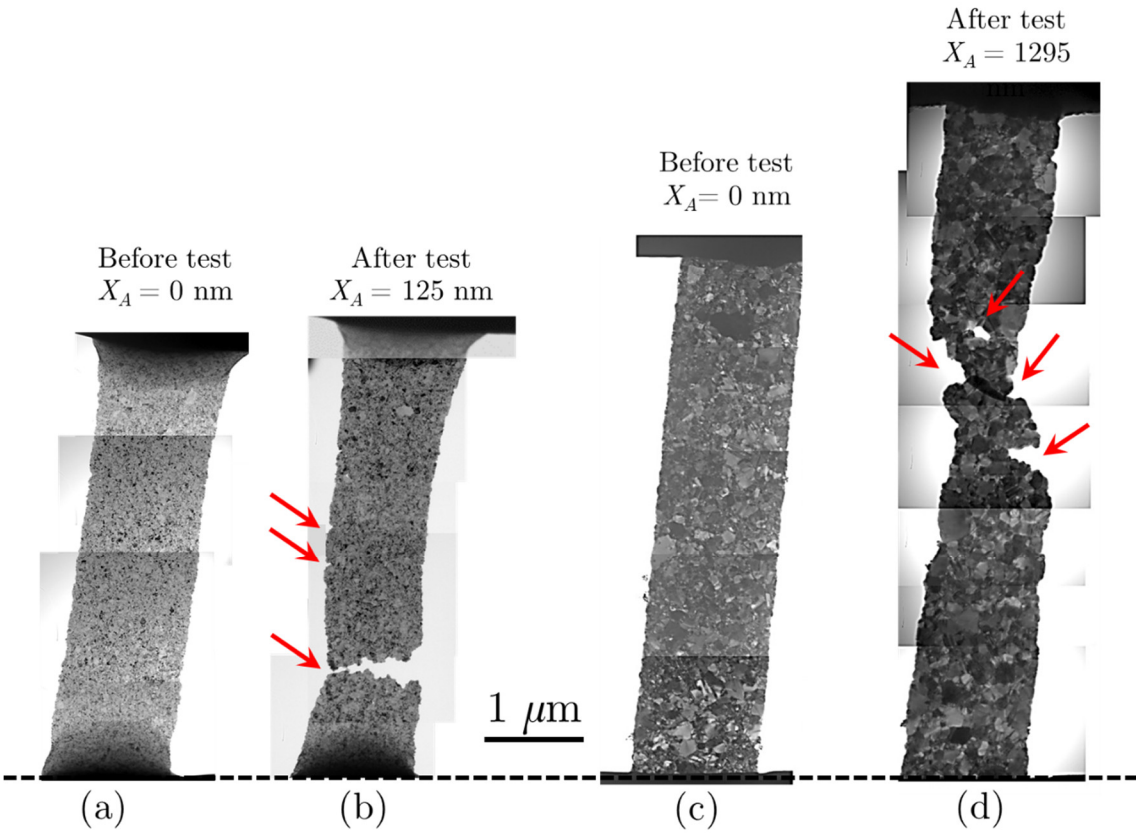

Figure 5.1 (a)-(b) TEM micrograph of the specimen with 30 nm thickness before and after fracture (c)-(d) TEM image of the specimen with 100 nm thickness before test and after failure

At the location of the crack, the width decreased by 15%, indicative of localized plastic deformation in the crack region, which is also consistent with the evidence of grain growth surrounding the crack tip shown in Figure 5.2. The *in situ* TEM observations clearly reveal that the intergranular crack propagates mainly via the growth of nanocracks that form due to GB decohesion ahead of the main crack and that eventually coalesce with the main crack.

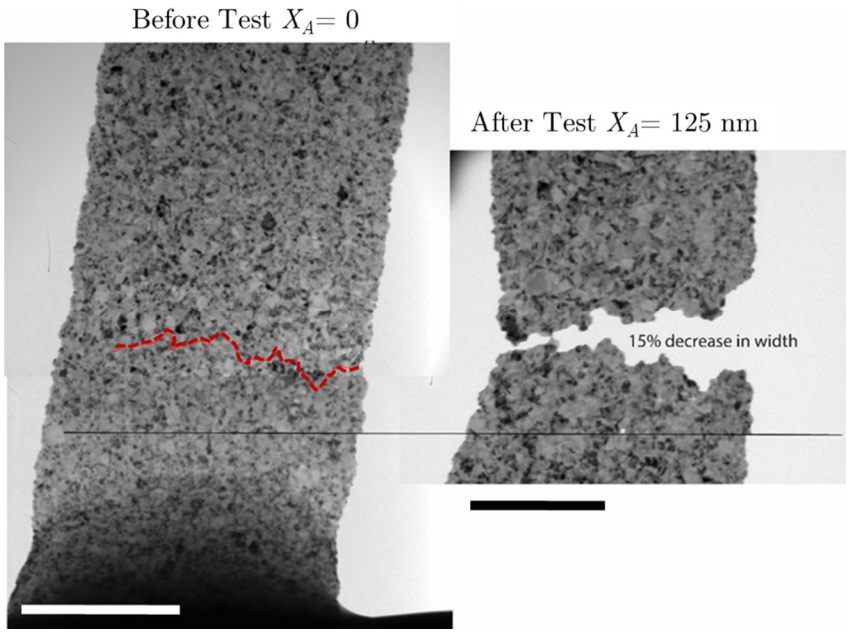

Figure 5.2 Comparison of the fractured area before and after test. Scale bars are 1 μm.

Most of the GB decohesion occurs during the loading steps or at the very beginning (i.e. within the first minute) of the holding steps during which large amounts of dislocation activities can be observed in a localized region ahead of the main crack. Figure 5.3 shows the crack after initiating from the right edge at X_A = 250 nm (V_{in} = 1.5 V). A nanocrack is observed roughly 200 nm ahead of the crack tip, along the GB of a large grain. At the end of the loading step to X_A = 320 nm (V_{in} = 1.78 V), GB decohesion occurs and the nanocracks grows by ~50-60 nm. During the hold at X_A = 320 nm (V_{in} = 1.78V), the main crack blunts (probably because of the large grain present at its tip), and the nanocrack grows by ~60 nm over 10 minutes. Previous study on cracking of brittle structures shows that the maximum triaxiality ahead of a notch appears ahead of the main crack [170]. This might explain the reason for the crack-out ahead of the main crack.

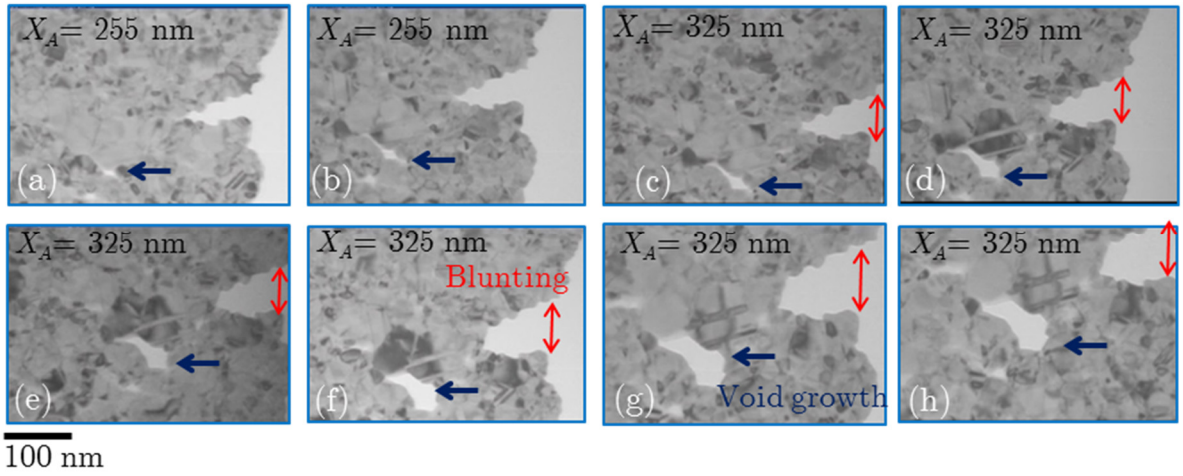

Figure 5.3 Evolution of microstructure and crack opening ahead of a crack. Snapshots extracted over time from a deforming 30 nm-thick specimen during stress relaxation experiment, performed inside transmission electron microscope at room temperature.

The blunting of the main crack and the increased opening of the nanocrack faces suggest that the local stresses decrease and little dislocation activities occur 10 minutes into the hold segment at $X_A = 320$ nm, except for the grain that is ahead of the nanocrack. Figure 5.4 shows clear evidence of GB decohesion ahead of the main crack and coalescence to the main crack tip during a loading step to $X_A = 360$ nm ($V_{in} = 1.9$ V). Towards the end of the loading step, large amounts of dislocation activities are observed in a region ~200 nm ahead of the main crack, leading in some cases to grain growth.

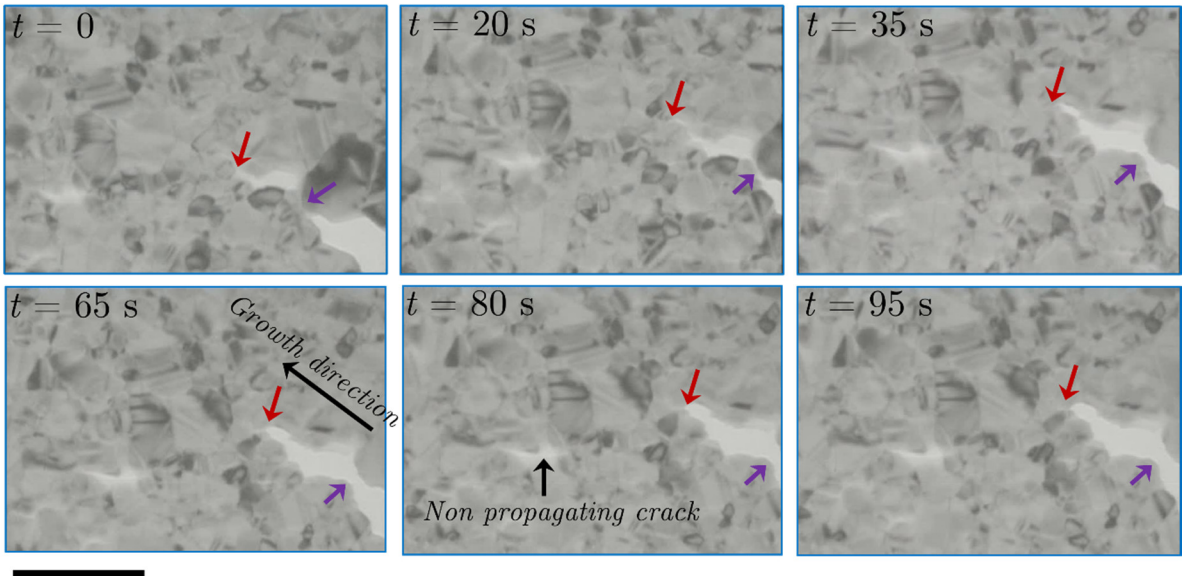

Figure 5.4 Snapshots, taken from a movie showing GB decohesion ahead of the main crack and coalescence to the main crack tip during a loading step to $X_A = 360$ nm. Scale bar is 100 nm.

These activities appear to slow down quickly (within a minute), in part because of the local unloading occurring due to GB decohesion. Very similar events occur during the later loading to $X_A = 375$ nm ($V_{in} = 1.96$ V) and 415 nm ($V_{in} = 2.07$ V). The nanocrack could also blunt, probably due to the presence of a large grain ahead of the crack tip. Three minutes into the hold at $X_A = 420$ nm ($V_{in} = 2.09$ V), Figure 5.5 shows GB decohesion between the nanocrack and the left edge of the specimen. The remaining ligament is ultimately fractured due to GB sliding during the loading to $X_A = 460$ nm ($V_{in} = 2.2$ V).

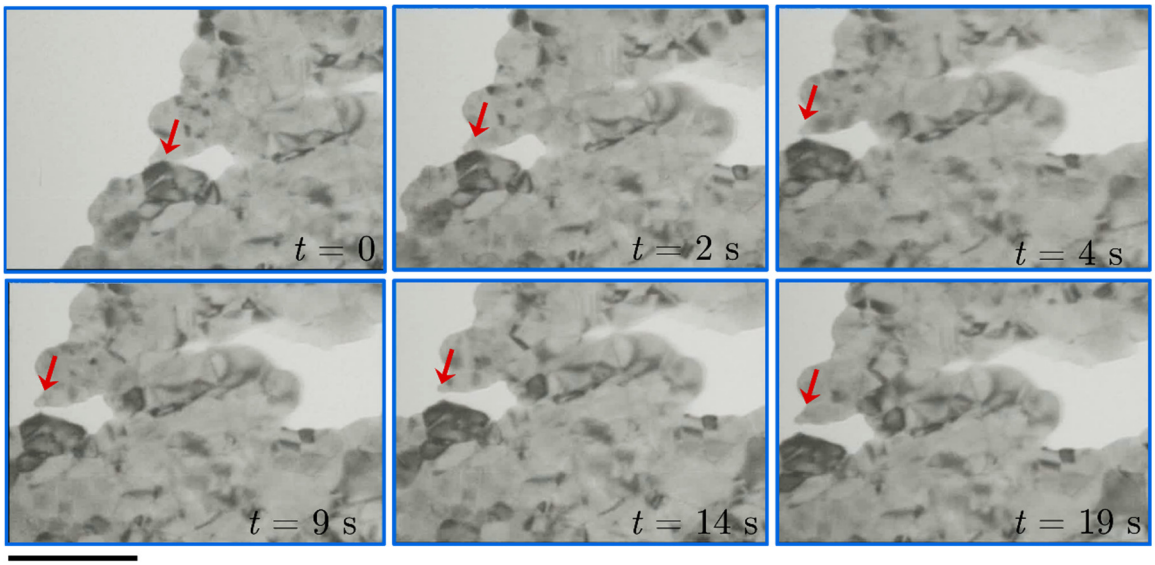

Figure 5.5 Snapshots taken from a movie that shows GB decohesion between the nanocrack and the left edge of the specimen. Scale bar is 100 nm.

5.2 Crack Growth in 100-nm-thick Au Specimens

In contrast, the crack growth process of the 100-nm-thick Au specimens is distinctly different from that of the 30-nm-thick specimens. Although intergranular crack growth also prevails, GB decohesion does not occur ahead of the main crack tip. Instead, the main crack extends in a continuous manner along the GB's as a result of significant GB dislocation activities leading to grain boundary sliding. This behavior was clearly observed during the *in situ* TEM tests of four specimens, as described next Figure 5.1(c)-(d) shows a comparison of the gauge length before and after the test of specimen 1, consisting of a series of fifteen successive holds at constant displacements X_A, increasing from 855 nm (V_{in} = 3 V) to 1295 nm (V_{in} = 3.6 V), each hold lasting between 2 and 10 minutes.

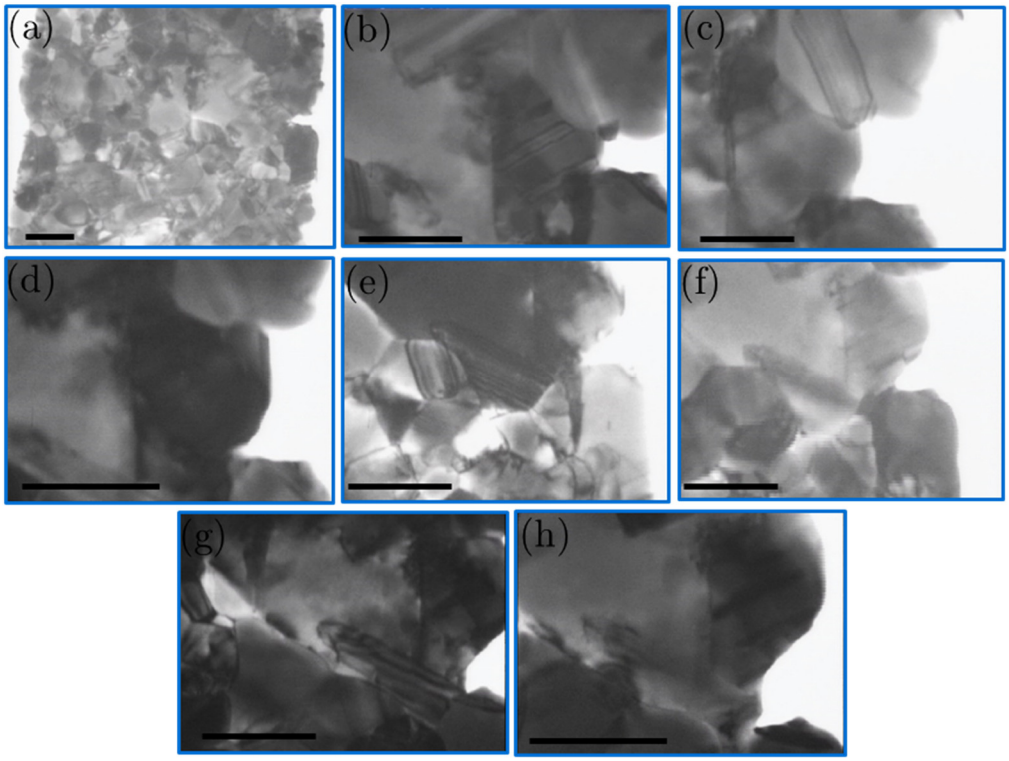

Figure 5.6 Crack tip blunting followed by branching out along adjacent grain boundaries. Scale bars are 200 nm.

At the end of the test, the specimen's elongation is ~30%, with locally a decrease in width of up to ~35%, highlighting a different crack growth behavior with respect to the 30-nm-thick specimen (see Figure 5.1). The main crack, along with another crack below, is oriented at an angle (~30-40°) with respect to the loading axis, also in contrast to the thinner specimen. At $X_A = 855$ nm ($V_{in} = 3$ V), a large (220-nm-long) angle GB, located in the center of the gauge section and oriented 35° with respect to the loading axis, undergoes sliding as a result of significant GB dislocation activities.

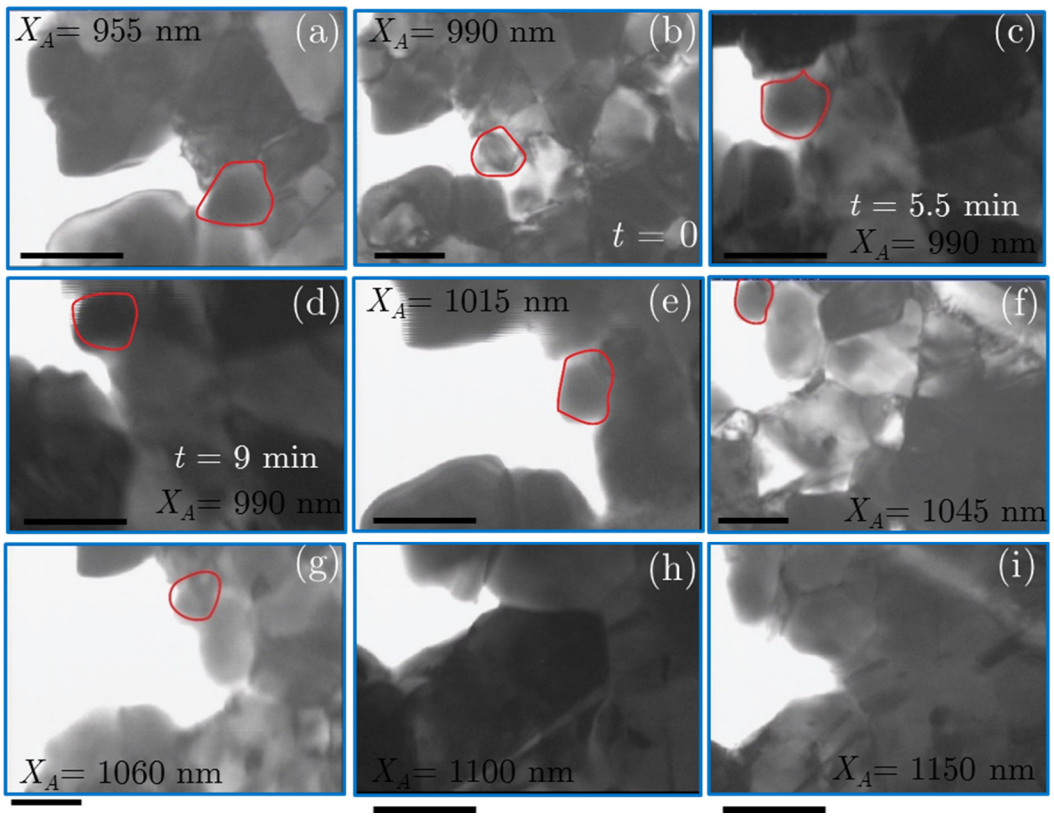

Figure 5.7 Intergranular crack growth. Scale bars are 100 nm.

A 200-nm-long grain boundary crack, oriented perpendicular to the loading axis, has formed on the right edge of the specimen, near the sliding large GB. On the left side of the specimen, slightly above (~500 nm) the sliding GB, another grain boundary crack has formed. Over the successive holds until X_A = 1130 nm (V_{in} = 3.39 V), the crack on the right blunted and branched out along adjacent GB's at angles with respect to the loading axis (see Figure 5.6). The crack on the left did not blunt and kept growing along GB's (see Figure 5.7). Figure 5.8 clearly shows GB activities initiating at the crack tip, resulting in stable intergranular crack growth. A few dislocations traversing grains near the crack tip can also be observed, likely triggered by the large stresses ahead of the crack (see Figure 5.8). GB dislocations flowing continuously from the crack tip to the sliding large GB, as the applied

displacement is increased to $X_A = 1230$ nm. At the end of the test ($X_A = 1295$ nm), a series of TEM images (shown in Figure 5.9) clearly highlights the GB sliding. The sliding path, shown by the dashed yellow line, corresponds to a facet in (111) grain.

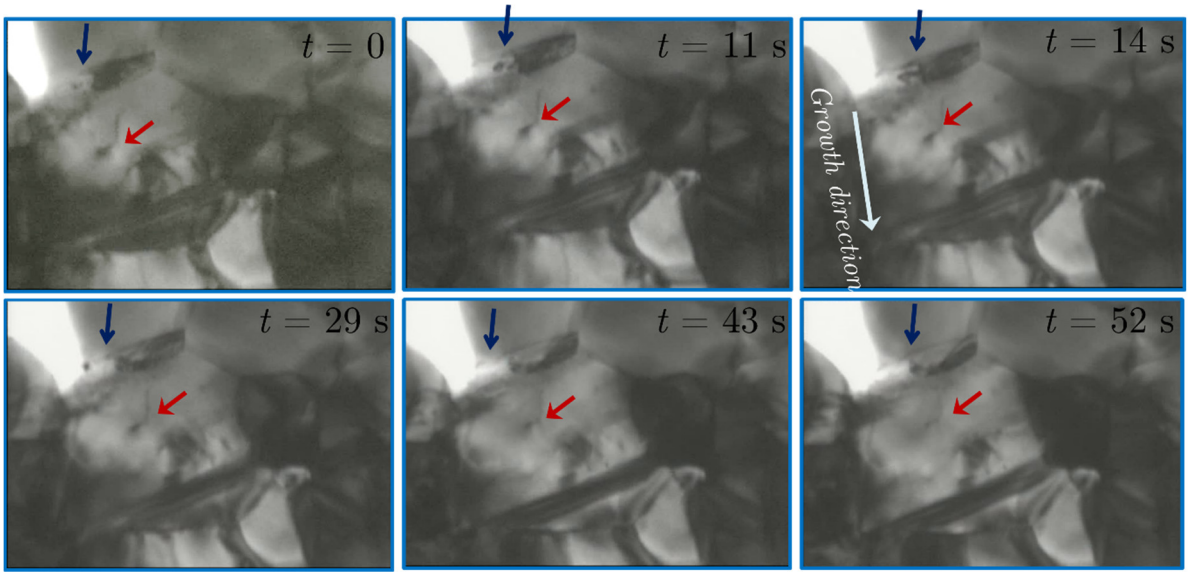

Figure 5.8 GB activities initiating at the crack tip, resulting in stable intergranular crack growth. Scale bar is 100 nm.

Stereographic projections prove that *G1* and *G2* have a relatively large angle of misorientation of about 54 °, close to the axis <011>. Comparison of the images shows a relative shear of 55 nm in a 6-minute period with an angle of approximately 45 degrees with respect to the tensile axis. By defining shear strain as the ratio of displacement along the GB over the diameter of *G1* (400 nm), this shear displacement corresponds to an increase in shear strain from 5.5 to 13.5% in 6 minutes, equivalent to a strain rate on the order of 10^{-5} s^{-1}.

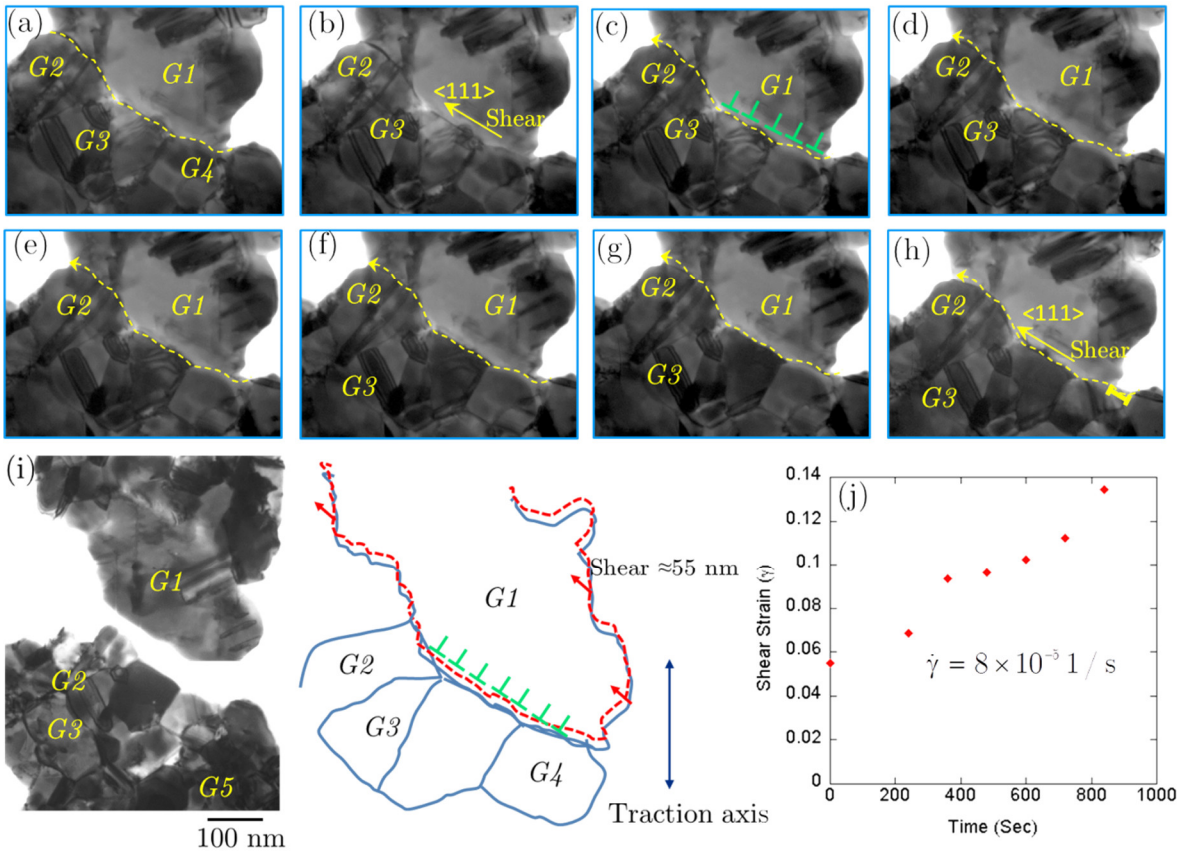

Figure 5.9 (a)-(h) Snapshots of the remaining segment in specimen 1 under the same diffracting conditions. GB sliding observed during relaxation of 100 nm film (i) full fracture (j) Plot of shear strain over time using TEM snapshots by interval of two minute in between.

Intergranular crack extension assisted by GB dislocations was also observed in another specimen (specimen 2). A 165-nm-long GB crack formed early during a 45-minute-long hold at $X_A = 550$ nm ($V_{in} = 2.45$ V, $\sigma \approx 400$ MPa). GB dislocations flow from the crack tip along a 210-nm-long GB that is inclined ~20° with respect to the loading axis, after 20 minutes at $X_A = 550$ nm ($V_{in} = 2.45$ V). A comparison of TEM images taken at an interval of 35 minutes shows a shear angle of 65 degrees resulting from the GB sliding as shown in Figure 5.10. GB dislocation activities increased as the displacement X_A was raised to 625 nm ($V_{in} = 2.6$ V), which led to the fracture of the specimen shortly after.

In one instance (specimen 3), we observed cracking along an active slip band in a large grain (~300 nm). During a hold at $X_A = 360$ nm ($V_{in} = 1.94$ V), a sustained slip band of dislocations in a (111) plane, oriented 30° with respect to the loading axis, concentrates most of the deformation in the specimen [26].

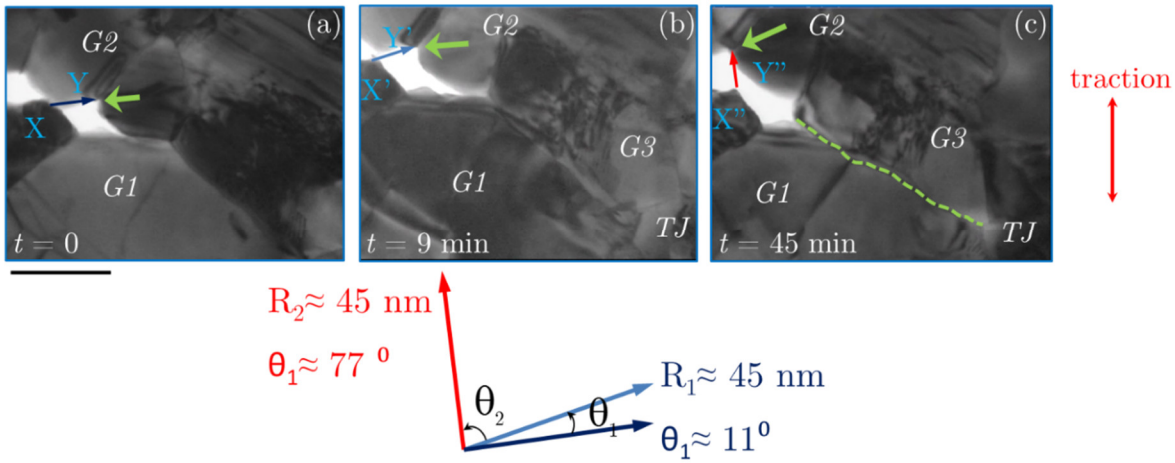

Figure 5.10 Snapshots ahead of the crack in specimen 2 shows significant grain boundary sliding in 30+ minutes. Scale bar is 100 nm.

A GB crack forms on the left side of the specimen near the deforming grain ($X_A = 530$ nm, $\sigma \approx 100$ MPa, $V_{in} = 2.4$ V), while a void forms at a triple point in the lower right of the deforming grain. As the applied displacement is increased to $X_A = 540$ nm, a continuous path of inter and transgranular dislocations flows from the triple junction void to the GB crack in Figure 5.11(a). As X_A is further increased to 550 nm, a crack forms along the slip band (see Figure 5.11(b)), linking the GB crack on the left side to the triple junction void. Crack extension further occurs as a result of GB dislocation motion ($X_A = 565$ nm) in which the crack extends by ~30 nm due to GB sliding during the increase of X_A to 615 nm.

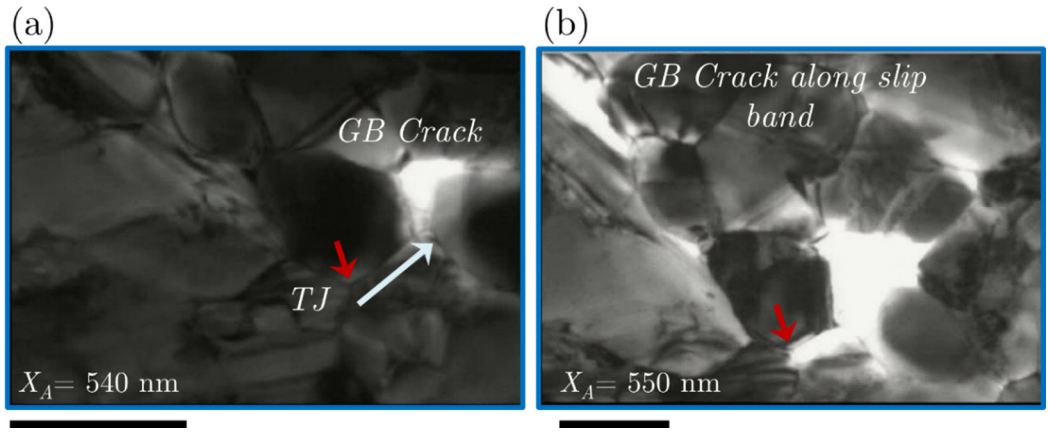

Figure 5.11 (a) transgranular dislocations flows from the triple junction void to the GB crack (b) second crack formed along the slip band. Scalebars are 100 nm.

5.3 Discussion

By employing the same testing technique (*in situ* TEM MEMS-based tensile tests consisting of successive displacement holds), same specimen geometry (1.5-μm-wide, 20-μm-long microbeams with two large ends for clamping) and same material (99.99% Au), this study clearly highlighted significant differences in the intergranular crack growth processes between the two types of specimens that can only result from the effects of thickness (30 vs 100 nm) and grain size distribution (see Figure 5.12).

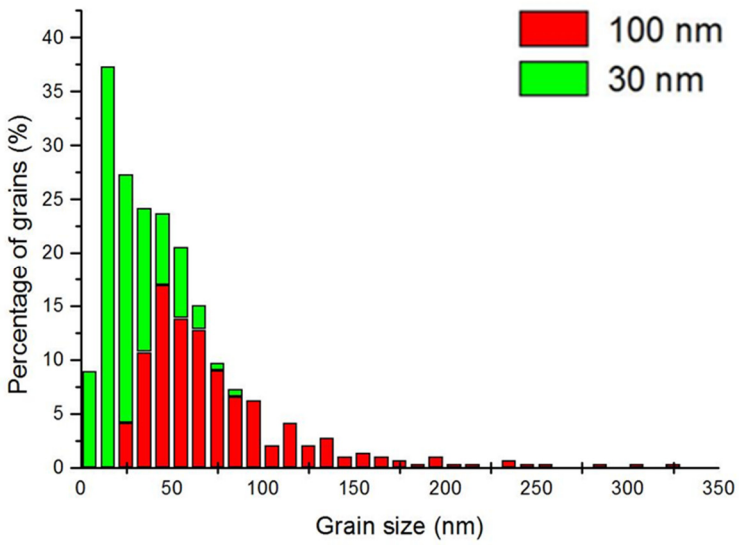

Figure 5.12 Grain size distribution for 30-nm-thick and 100-nm-thick films

For the 30-nm-thick specimens having an average grain size of 40 nm and grains no larger than 100 nm in diameter, the crack growth process occurs mainly due to GB decohesion ahead of the main crack, and coalescence of these nanocracks to the main crack. Upon a displacement impulse, dislocation activities can be observed ahead of the main crack but slow down very quickly (within a minute), likely as a result of local unloading due to nanocrack formation. In contrast, for the 100-nm-thick specimens having an average grain size of 70 nm and grains as large as 350 nm in diameter, intergranular crack growth occurs mainly as a result of sustained (i.e. even after a displacement hold of 30 minutes) GB dislocation activities leading to GB sliding along the large ($>$ 200 nm) grain boundaries. For these thicker specimens, nanocrack formation ahead of the main crack is not observed.

The crack growth process observed in the 30-nm-thick Au specimens is consistent with the majority of previous *in situ* TEM studies showing nucleation and coalescence of nanocracks [134, 135, 137, 171], and with atomistic simulations

performed on NC Ni (grain sizes ranging from 5 to 10-12 nm). These simulations revealed that large stresses are present ahead of the crack tip, which triggers both dislocation activities and GB decohesion, which we observe as well in a region of ~200 nm ahead of the main crack. The simulations also revealed that the nanovoid formation can be assisted by partial dislocation activities, and that it is associated with vacancy cluster formation [130]. A theoretical model also predicted nanocrack formation ahead of blunted cracks due to the combined effects of large stresses ahead of a blunt crack and the superposed stress field associated with GB dislocations at triple junctions [172].

In contrast, the observed GB-sliding-assisted crack growth behavior for the 100-nm-thick Au specimens constitutes a significant difference from the previously documented mechanisms. While the crack growth mode is also intergranular, the mechanism does not involve any nanovoid / nanocrack formation ahead of the main crack, which may be explained by either a lower driving force for GB decohesion or higher resistance against it. As highlighted in the aforementioned theoretical model [172], larger grain sizes decrease the likelihood of nanocrack formation because of the decreased stress levels farther away from the crack tip. It is therefore possible that the larger grains in the 100-nm-thick Au specimens do not provide the necessary conditions to form nanocracks. We also hypothesize that the GB's may be more resistant to decohesion in the thicker films. Both thickness and grain size distribution could therefore affect the formation of nanocracks ahead of the main crack tip, and alternative crack growth mechanisms become dominant if nanocracks formation does

not occur. As in bulk metals, transgranular dislocation activities ahead of the crack tip were observed in several instances, (see Figure 5.8 and Figure 5.11). However, the motion of GB dislocations clearly dictated the intergranular stable crack growth via GB sliding (see Figure 5.9 and Figure 5.10). Slip-induced GB sliding was also observed in 300-nm-thick Al microbeams with an average grain size of about 250 nm [173]. In that study, GB dislocations were observed irrespective of the GB orientations, which led to the conclusion that a thin film effect (GB grooves facilitating GB dislocation nucleation) could be responsible for this behavior. A similar thin film effect may trigger slip-induced GB sliding ahead of the crack tip in the 100-nm-thick Au films.

A key characteristic of the observed slip-induced GB sliding is that it is accommodated along several adjacent grains (see Figure 5.9 and Figure 5.11) showing a continuous path for dislocations across several grains). A theoretical model showed that a significant increase in fracture toughness is predicted in NC metals in which accommodated GB sliding occurs (such as at intermediate temperatures), as a result of crack blunting [174]. It is possible that accommodated GB sliding is more likely to occur in microbeams spanning only a few grains across the width, as opposed to bulk NC metals or thin films with large lateral dimensions (such as membranes). As such, it may allow stable growth of the main crack across the 1.5-μm-wide microbeam, as opposed to forming GB nanovoids / nanocracks in the case of unaccommodated GB sliding, such as in bulk NC metals [137] or thin film membranes [134, 135, 137, 171].

5.4 Conclusion

Crack growth mechanisms of NC gold ultrathin films with thicknesses of 30 nm and 100 nm have been experimentally studied using *in situ* TEM technique. For the 100-nm-thick films, there exist both intragranular and intergranular deformation mechanisms. Mainly, dislocations flow along the grain boundaries, leading to grain boundary sliding. The initiated sharp cracks blunt and grows slowly along the grain boundaries during the stress relaxation segments without requiring to increase the stress even after tens of minutes. In contrast, for the 30-nm-thick film, intergranular crack propagates mainly via the growth of nanocracks that form due to GB decohesion ahead of the main crack and that eventually coalesce with the main crack. Most of the GB decohesion occurs during the loading steps or at the very beginning (i.e. within the first minute) of the holding steps. In contrast to 100 nm films it is required to increase the stress for the cracks in 30-nm-thick film to grow further. These results improve our knowledge on the mechanisms of crack growth in NC metallic films and their dependence on the film thickness and grain size distribution.

CHAPTER VI

SIGNIFICANCE

This thesis presents a novel and versatile MEMS-based nanomechanical testing technique aimed at providing a fundamental understanding of the failure properties in nanocrystalline FCC ultrathin films. This understanding provides useful guidelines for increasing the safety and mechanical reliability of thin films and coatings, frequently used in MEMS technology.

The significant contributions are:

1- The development of a MEMS-based nanomechanical testing technique. We demonstrate a new versatile MEMS-based experimental setup which is used for quantitative *in situ* TEM tensile experiments of NC ultrathin films, whereby the evolution of the stress-strain curve could be monitored over time/cycles, thanks to capacitive sensing of both load and elongation. This is the major advantage of this technique over the existing MEMS-based techniques [41, 175], which let us use TEM imaging solely for high magnification microstructural observations while the MEMS device provides continuous tracking of the material's response, and the possibility to perform the same kind of experiments outside of an electron microscope (*ex situ* testing). Another major accomplishment was to develop an effective manipulation and clamping procedure to circumvent the need for FIB-based manipulation and specimen clamping.

2- The successful employment of the above-mentioned experimental setup to conduct quantitative *in situ* TEM fatigue testing on NC gold ultrathin films. The 100-nm-thick, 1.5-μm-wide NC Au specimens have a tensile strength of ~1 -1.13 GPa, and a total elongation to failure of ~2.8-5%. The specimens exhibit a ratcheting behavior under tension-tension cyclic loading in near stress-controlled conditions. Nanoscale fatigue cracks were observed after nearly 7000 cycles for $\sigma_{max} \sim 0.8$ GPa. The quantitative results along with direct observation of fatigue cracking in nanoscale is the first of its kind in NC ultrathin films, and thus provides important information regarding cyclic plasticity of NC metallic films [33].

3- Quantification and observation of viscoplasticity in NC gold ultrathin films. This work is the first to unveil the transient stress relaxation deformation mechanisms in NC metals. The power-law exponent n continuously decreases from initial large values (n from 6 to 14 at $t = 0$) down to low values ($n \sim$ 1-2) if the test is long enough (several hours). The *in situ* TEM results show that the transient relaxation behavior under large stresses is accommodated by sustained dislocation motion, either intergranular or transgranular, only in a few grains (the larger grains (above ~200 nm) that are favorably oriented for maximum shear), which could only be observed with a technique like *in situ* TEM. Over time, the dislocation sources, located in or close to grain boundary and triple junctions, become less operative as a result of the decrease in applied stress, or exhausted, likely leading to a transition to a grain-boundary-diffusion based mechanism. However, most of these sources are robust enough to produce additional dislocations upon increase of the applied stress,

contributing to significantly larger ductility than for monotonic tests by maintaining localized shear regions.

4- Study of crack growth mechanisms of NC gold ultrathin films with thicknesses of 30 nm (average grain size $\bar{d}$ of ~40 nm) and 100 nm ($\bar{d}$of ~70 nm) using *in situ* TEM technique. For the 100-nm-thick films, there exist both intragranular and intergranular deformation mechanisms. Mainly, dislocations flow along the grain boundaries, leading to grain boundary sliding. The initiated sharp cracks blunt and grow slowly along the grain boundaries during the stress relaxation segments without requiring to increase the stress even after tens of minutes. In contrast, for the 30-nm-thick film, intergranular crack propagates mainly via the growth of nanocracks that form due to GB decohesion ahead of the main crack and that eventually coalesce with the main crack. Most of the GB decohesion occurs during the loading steps or at the very beginning (i.e. within the first minute) of the holding steps. In contrast to 100 nm films it is required to increase the stress for the cracks in 30-nm-thick film to grow further.

CHAPTER VII

RECOMMENDATIONS FOR FUTURE WORK

Although this experimental technique represents a crucial advance in nanomechanical testing there are still some challenges that needs to be considered. Sensing circuit suffers from a limitation that only $\Delta C_1 - \Delta C_2$ is measured and therefore the calculation of load and displacement involves an underlying assumption of elastic behavior of the thin film under tension. Further refinements in the sensing technique should be pursued to eliminate or reduce the noise and drift in stress/strain measurement.

Repeated relaxation tests could be conducted with constant durations, starting at a given stress level to measure true activation volume. The measurement of such quantity could allow the identification of changes in the deformation mechanisms and evolution of dislocation density as a function of strain. Furthermore the back stress and athermal stress for dislocation motion could be identified by dip test technique.

Investigation of other FCC metals such as nickel, platinum and aluminum is recommended. These metallic thin films are regularly used in micro devices and therefore it is of interest to study their failure properties (fatigue, creep and fracture) to understand how stacking fault energy could affect failure mechanisms.

Considering the novel capability of the introduced experimental technique, allowing *ex situ* tests in conjunction with *in situ* experiments, the investigation of the influence of the environment on the fatigue/creep properties of ultrathin films is highly recommended. This could improve the understanding of the environmental effects on underlying fatigue and creep deformation mechanisms in NC thin films.

APPENDIX A

The grain boundary sliding (GBS) mechanism [75, 167] controlled by grain boundary diffusion is governed by the following equation:

$$\dot{\varepsilon} = 2 \times 10^5 D_{0,gb} \, exp\left(\frac{-Q_{gb}}{RT}\right) \frac{\mu b}{kT} \left(\frac{b}{d}\right)^3 \left(\frac{\sigma}{\mu}\right)^2 \tag{8-1}$$

Where $D_{0,gb}$ is the pre-exponential coefficient for grain boundary diffusion, Q_{gb} is the activation energy for grain boundary diffusion, k is Boltzmann's constant, T is the absolute temperature (T = 300° K), μ is the shear modulus, b is Burger's vector, d is the average grain size, and σ is the applied stress. Coble creep is another important mechanism of deformation which could occur for NC metals and ultrafine materials [168]. The Coble creep equation is given by:

$$\dot{\varepsilon} = 14 \pi \delta D_{0,gb} \, exp\left(\frac{-Q_{gb}}{RT}\right) \frac{\Omega}{RT} \frac{\sigma}{d^3} \tag{8-2}$$

Where δ is the grain boundary width, Ω is the molar volume, and R is the ideal gas constant. Finally, the Asbhy-Verral mechanism is governed by the following equation [132, 167]:

$$\dot{\varepsilon} = 330 \, \delta D_{0,gb} \, exp\left(\frac{-Q_{gb}}{RT}\right) \frac{\Omega}{RT} \left(\frac{\sigma}{d^3} - \frac{0.72\Gamma}{d^4}\right) \tag{8-3}$$

Where Γ is the free energy of grain boundary.

Table 8.1 shows the material properties of NC gold that are used in the abovementioned equations.

Table 8.1 Material parameters for NC Au [166].

$D_{0,gb}$ (m^2/s)	Q_{gb} (kJ/mol)	μ (GPa)	b (nm)	d (nm)	δ (nm)	Ω (m^3/mol)	Γ (J/m^2)
6.2×10^{-7}	85	25	0.282	75	0.5	1.44×10^{-5}	0.2

REFERENCES

[1] G. Hass, On the Preparation of Hard Oxide Films with Precisely Controlled Thickness on Evaporated Aluminum Mirrors, J Opt Soc Am, 39(1949) 532-40.

[2] S.S. Shankar, A. Rai, A. Ahmad, M. Sastry, Controlling the optical properties of lemongrass extract synthesized gold nanotriangles and potential application in infrared-absorbing optical coatings, Chem Mater, 17(2005) 566-72.

[3] M.G. Kim, M.G. Kanatzidis, A. Facchetti, T.J. Marks, Low-temperature fabrication of high-performance metal oxide thin-film electronics via combustion processing, Nat Mater, 10(2011) 382-8.

[4] N.S. Lu, Z.G. Suo, J.J. Vlassak, The effect of film thickness on the failure strain of polymer-supported metal films, Acta Mater, 58(2010) 1679-87.

[5] R. Chen, K. Pan, H. Lin, N. Wei, F. Zuo, Ductility of thin metal film on a polymer substrate for stretchable electronics, Materials Research Innovations, 19(2015) S8-268-S8-72.

[6] T. Li, Z. Huang, Z. Xi, S.P. Lacour, S. Wagner, Z. Suo, Delocalizing strain in a thin metal film on a polymer substrate, Mechanics of Materials, 37(2005) 261-73.

[7] S.R. Forrest, The path to ubiquitous and low-cost organic electronic appliances on plastic, Nature, 428(2004) 911-8.

[8] M. Shtein, J. Mapel, J.B. Benziger, S.R. Forrest, Effects of film morphology and gate dielectric surface preparation on the electrical characteristics of organic-vapor-phase-deposited pentacene thin-film transistors, Appl Phys Lett, 81(2002) 268-70.

[9] G. Thomas, Materials science - Invisible circuits, Nature, 389(1997) 907-8.

[10] K. Nomura, H. Ohta, A. Takagi, T. Kamiya, M. Hirano, H. Hosono, Room-temperature fabrication of transparent flexible thin-film transistors using amorphous oxide semiconductors, Nature, 432(2004) 488-92.

[11] H. Oh, S.M. Yoon, M.K. Ryu, C.S. Hwang, S. Yang, S.H.K. Park, Transition of dominant instability mechanism depending on negative gate bias under illumination in amorphous In-Ga-Zn-O thin film transistor, Appl Phys Lett, 98(2011).

[12] A. Suresh, J.F. Muth, Bias stress stability of indium gallium zinc oxide channel based transparent thin film transistors, Appl Phys Lett, 92(2008).

[13] J.K. Jeong, H.W. Yang, J.H. Jeong, Y.G. Mo, H.D. Kim, Origin of threshold voltage instability in indium-gallium-zinc oxide thin film transistors, Appl Phys Lett, 93(2008).

[14] K. Nomura, T. Kamiya, M. Hirano, H. Hosono, Origins of threshold voltage shifts in room-temperature deposited and annealed a-In-Ga-Zn-O thin-film transistors, Appl Phys Lett, 95(2009).

[15] F. Ayazi, K. Najafi, A HARPSS polysilicon vibrating ring gyroscope, J Microelectromech S, 10(2001) 169-79.

[16] O. Tabata, K. Kawahata, S. Sugiyama, I. Igarashi, Mechanical Property Measurements of Thin-Films Using Load Deflection of Composite Rectangular Membranes, Sensor Actuator, 20(1989) 135-41.

[17] T. Straub, E.K. Baumert, C. Eberl, O.N. Pierron, A method for probing the effects of conformal nanoscale coatings on fatigue crack initiation in electroplated Ni films, Thin Solid Films, 526(2012) 176-82.

[18] T.R. Hsu, Reliability in MEMS packaging, Int Rel Phy, (2006) 398-402.

[19] A.M. El-Sherik, J. Shirokoff, U. Erb, Stress measurements in nanocrystalline Ni electrodeposits, J Alloy Compd, 389(2005) 140-3.

[20] S. Van Petegem, F. Dalla Torre, D. Segers, H. Van Swygenhoven, Free volume in nanostructured Ni, Scripta Mater, 48(2003) 17-22.

[21] H. Idrissi, B.J. Wang, M.S. Colla, J.P. Raskin, D. Schryvers, T. Pardoen, Ultrahigh Strain Hardening in Thin Palladium Films with Nanoscale Twins, Adv Mater, 23(2011) 2119-+.

[22] B. Wang, H. Idrissi, M. Galceran, M.S. Colla, S. Turner, S. Hui, et al., Advanced TEM investigation of the plasticity mechanisms in nanocrystalline freestanding palladium films with nanoscale twins, Int J Plasticity, 37(2012) 140-56.

[23] F. Tang, D.S. Gianola, M.P. Moody, K.J. Hemker, J.M. Cairney, Observations of grain boundary impurities in nanocrystalline Al and their influence on micro structural stability and mechanical behaviour, Acta Mater, 60(2012) 1038-47.

[24] B. Amin-Ahmadi, H. Idrissi, M. Galceran, M.S. Colla, J.P. Raskin, T. Pardoen, et al., Effect of deposition rate on the microstructure of electron beam evaporated nanocrystalline palladium thin films, Thin Solid Films, 539(2013) 145-50.

[25] B. Wang, H. Idrissi, H. Shi, M.S. Colla, S. Michotte, J.P. Raskin, et al., Texture-dependent twin formation in nanocrystalline thin Pd films, Scripta Mater, 66(2012) 866-71.

[26] S. Reyntjens, R. Puers, A review of focused ion beam applications in microsystem technology, J Micromech Microeng, 11(2001) 287-300.

[27] N. Bassim, K. Scott, L.A. Giannuzzi, Recent advances in focused ion beam technology and applications, Mrs Bull, 39(2014) 317-25.

[28] L. Giannuzzi, F.A. Stevie, A review of focused ion beam milling techniques for TEM specimen preparation, Micron, 30(1999) 197-204.

[29] S. Matsui, T. Kaito, J.-i. Fujita, M. Komuro, K. Kanda, Y. Haruyama, Three-dimensional nanostructure fabrication by focused-ion-beam chemical vapor deposition, Journal of Vacuum Science & Technology B, 18(2000) 3181-4.

[30] S. Reyntjens, R. Puers, A review of focused ion beam applications in microsystem technology, J Micromech Microeng, 11(2001) 287.

[31] H.D. Espinosa, B.C. Prorok, M. Fischer, A methodology for determining mechanical properties of freestanding thin films and MEMS materials, J Mech Phys Solids, 51(2003) 47-67.

[32] H.D. Espinosa, Y. Zhu, N. Moldovan, Design and operation of a MEMS-based material testing system for nanomechanical characterization, J Microelectromech S, 16(2007) 1219-31.

[33] E. Hosseinian, O.N. Pierron, Quantitative in situ TEM tensile fatigue testing on nanocrystalline metallic ultrathin films, Nanoscale, 5(2013) 12532-41.

[34] S. Cuenot, C. Fretigny, S. Demoustier-Champagne, B. Nysten, Measurement of elastic modulus of nanotubes by resonant contact atomic force microscopy, J Appl Phys, 93(2003) 5650-5.

[35] S. Cuenot, C. Fretigny, S.M. Demoustier-Champagne, B. Nysten, Resonant contact-AFM measurement of the elastic properties of nanomaterials., Abstr Pap Am Chem S, 224(2002) U405-U6.

[36] E.K. Baumert, O.N. Pierron, Fatigue Degradation Properties of LIGA Ni Films Using Kilohertz Microresonators, J Microelectromech S, 22(2013) 16-25.

[37] E.K. Baumert, O.N. Pierron, Very high cycle fatigue crack initiation in electroplated Ni films under extreme stress gradients, Scripta Mater, 67(2012) 45-8.

[38] B. Moser, R. Schwaiger, M. Dao, Size effects on deformation and fracture of nanostructured metals, Nanostructured Coatings, Springer2006, pp. 27-77.

[39] M. Legros, D.S. Gianola, C. Motz, Quantitative In Situ Mechanical Testing in Electron Microscopes, Mrs Bull, 35(2010) 354-60.

[40] M.A. Haque, H.D. Espinosa, H.J. Lee, MEMS for In Situ Testing-Handling, Actuation, Loading, and Displacement Measurements, Mrs Bull, 35(2010) 375-81.

[41] M.A. Haque, M.T.A. Saif, In-situ tensile testing of nano-scale specimens in SEM and TEM, Exp Mech, 42(2002) 123-8.

[42] M.A. Haque, M.T.A. Saif, In situ tensile testing of nanoscale freestanding thin films inside a transmission electron microscope, J Mater Res, 20(2005) 1769-77.

[43] M.A. Haque, M.T.A. Saif, Deformation mechanisms in free-standing nanoscale thin films: A quantitative in situ transmission electron microscope study, P Natl Acad Sci USA, 101(2004) 6335-40.

[44] Y. Zhu, A. Corigliano, H.D. Espinosa, A thermal actuator for nanoscale in situ microscopy testing: design and characterization, J Micromech Microeng, 16(2006) 242-53.

[45] Y. Zhu, H.D. Espinosa, An electromechanical material testing system for in situ electron microscopy and applications, P Natl Acad Sci USA, 102(2005) 14503-8.

[46] Y. Zhu, N. Moldovan, H.D. Espinosa, A microelectromechanical load sensor for in situ electron and x-ray microscopy tensile testing of nanostructures, Appl Phys Lett, 86(2005).

[47] S. Gravier, M. Coulombier, A. Safi, N. Andre, A. Boe, J.P. Raskin, et al., New On-Chip Nanomechanical Testing Laboratory - Applications to Aluminum and Polysilicon Thin Films, J Microelectromech S, 18(2009) 555-69.

[48] Y. Lu, Y. Ganesan, J. Lou, A Multi-step Method for In Situ Mechanical Characterization of 1-D Nanostructures Using a Novel Micromechanical Device, Exp Mech, 50(2010) 47-54.

[49] B. Merle, M. Goeken, Bulge fatigue testing of freestanding and supported gold films, J Mater Res, 29(2014) 267-76.

[50] H. Guo, K. Chen, Y. Oh, K. Wang, C. Dejoie, S.A.S. Asif, et al., Mechanics and Dynamics of the Strain-Induced M1-M2 Structural Phase Transition in Individual VO2 Nanowires, Nano Lett, 11(2011) 3207-13.

[51] D. Kiener, A.M. Minor, Source Truncation and Exhaustion: Insights from Quantitative in situ TEM Tensile Testing, Nano Lett, 11(2011) 3816-20.

[52] C. Koch, Nanocrystalline Materials: Mechanical Properties, Encyclopedia of Materials: Science and Technology, (2005) 5901-5.

[53] M. Dao, L. Lu, R.J. Asaro, J.T.M. De Hosson, E. Ma, Toward a quantitative understanding of mechanical behavior of nanocrystalline metals, Acta Mater, 55(2007) 4041-65.

[54] M.A. Meyers, A. Mishra, D.J. Benson, Mechanical properties of nanocrystalline materials, Prog Mater Sci, 51(2006) 427-556.

[55] A. Pineau, A.A. Benzerga, T. Pardoen, Failure of metals III. Fracture and fatigue of nanostructured metallic materials, Acta Mater, (2015).

[56] P. Cavaliere, Mechanical Properties of Nanocrystalline Materials, Handbook of Mechanical Nanostructuring, (2015) 1-16.

[57] I. Ovid'Ko, Review on the fracture processes in nanocrystalline materials, J Mater Sci, 42(2007) 1694-708.

[58] T. Hanlon, E.D. Tabachnikova, S. Suresh, Fatigue behavior of nanocrystalline metals and alloys, Int J Fatigue, 27(2005) 1147-58.

[59] K.S. Kumar, H. Van Swygenhoven, S. Suresh, Mechanical behavior of nanocrystalline metals and alloys, Acta Mater, 51(2003) 5743-74.

[60] W. Wang, Y. Zhong, K. Lu, L. Lu, D.L. McDowell, T. Zhu, Size effects and strength fluctuation in nanoscale plasticity, Acta Mater, 60(2012) 3302-9.

[61] F. Dalla Torre, H. Van Swygenhoven, M. Victoria, Nanocrystalline electrodeposited Ni: microstructure and tensile properties, Acta Mater, 50(2002) 3957-70.

[62] R.T. Zhu, J.Q. Zhou, H. Jiang, D.S. Zhang, Strain localization of fully dense nanocrystalline Ni sheet, J Mater Sci, 45(2010) 759-64.

[63] K.M. Youssef, R.O. Scattergood, K.L. Murty, C.C. Koch, Ultratough nanocrystalline copper with a narrow grain size distribution, Appl Phys Lett, 85(2004) 929-31.

[64] J. Chen, L. Lu, K. Lu, Hardness and strain rate sensitivity of nanocrystalline Cu, Scripta Mater, 54(2006) 1913-8.

[65] V. Yamakov, D. Wolf, S.R. Phillpot, A.K. Mukherjee, H. Gleiter, Deformation-mechanism map for nanocrystalline metals by molecular-dynamics simulation, Nat Mater, 3(2004) 43-7.

[66] D. Wolf, V. Yamakov, S.R. Phillpot, A. Mukherjee, H. Gleiter, Deformation of nanocrystalline materials by molecular-dynamics simulation: relationship to experiments?, Acta Mater, 53(2005) 1-40.

[67] J. Schiotz, K.W. Jacobsen, A maximum in the strength of nanocrystalline copper, Science, 301(2003) 1357-9.

[68] A.H. Chokshi, A. Rosen, J. Karch, H. Gleiter, On the Validity of the Hall-Petch Relationship in Nanocrystalline Materials, Scripta Metall Mater, 23(1989) 1679-83.

[69] D. Farkas, M. Willemann, B. Hyde, Atomistic mechanisms of fatigue in nanocrystalline metals, Phys Rev Lett, 94(2005).

[70] J.R. Trelewicz, C.A. Schuh, The Hall–Petch breakdown in nanocrystalline metals: a crossover to glass-like deformation, Acta Mater, 55(2007) 5948-58.

[71] H. Hirakata, N. Fukuhara, S. Ajioka, A. Yonezu, M. Sakihara, K. Minoshima, The effect of thickness on the steady-state creep properties of freestanding aluminum nano-films, Acta Mater, 60(2012) 4438-47.

[72] N.J. Karanjgaokar, C.S. Oh, J. Lambros, I. Chasiotis, Inelastic deformation of nanocrystalline Au thin films as a function of temperature and strain rate, Acta Mater, 60(2012) 5352-61.

[73] N. Karanjgaokar, F. Stump, P. Geubelle, I. Chasiotis, A thermally activated model for room temperature creep in nanocrystalline Au films at intermediate stresses, Scripta Mater, 68(2013) 551-4.

[74] L. Lu, M.L. Sui, K. Lu, Superplastic extensibility of nanocrystalline copper at room temperature, Science, 287(2000) 1463-6.

[75] H. Van Swygenhoven, P.A. Derlet, Grain-boundary sliding in nanocrystalline fcc metals, Phys Rev B, 64(2001).

[76] Y.B. Wang, B.Q. Li, M.L. Sui, S.X. Mao, Deformation-induced grain rotation and growth in nanocrystalline Ni, Appl Phys Lett, 92(2008).

[77] Z.W. Shan, E.A. Stach, J.M.K. Wiezorek, J.A. Knapp, D.M. Follstaedt, S.X. Mao, Grain boundary-mediated plasticity in nanocrystalline nickel, Science, 305(2004) 654-7.

[78] M. Legros, D.S. Gianola, K.J. Hemker, In situ TEM observations of fast grain-boundary motion in stressed nanocrystalline aluminum films, Acta Mater, 56(2008) 3380-93.

[79] A.J. Haslam, D. Moldovan, V. Yamakov, D. Wolf, S.R. Phillpot, H. Gleiter, Stress-enhanced grain growth in a nanocrystalline material by molecular-dynamics simulation, Acta Mater, 51(2003) 2097-112.

[80] X.L. Wu, Y.T. Zhu, E. Ma, Predictions for partial-dislocation-mediated processes in nanocrystalline Ni by generalized planar fault energy curves: An experimental evaluation, Appl Phys Lett, 88(2006).

[81] Y.F. Shen, L. Lu, Q.H. Lu, Z.H. Jin, K. Lu, Tensile properties of copper with nano-scale twins, Scripta Mater, 52(2005) 989-94.

[82] Y.F. Shen, L. Lu, M. Dao, S. Suresh, Strain rate sensitivity of Cu with nanoscale twins, Scripta Mater, 55(2006) 319-22.

[83] M. Dao, L. Lu, Y.F. Shen, S. Suresh, Strength, strain-rate sensitivity and ductility of copper with nanoscale twins, Acta Mater, 54(2006) 5421-32.

[84] O. Anderoglu, A. Misra, H. Wang, F. Ronning, M.F. Hundley, X. Zhang, Epitaxial nanotwinned Cu films with high strength and high conductivity, Appl Phys Lett, 93(2008).

[85] O. Anderoglu, A. Misra, J. Wang, R.G. Hoagland, J.P. Hirth, X. Zhang, Plastic flow stability of nanotwinned Cu foils, Int J Plasticity, 26(2010) 875-86.

[86] W.D. Nix, J.R. Greer, G. Feng, E.T. Lilleodden, Deformation at the nanometer and micrometer length scales: Effects of strain gradients and dislocation starvation, Thin Solid Films, 515(2007) 3152-7.

[87] T.A. Parthasarathy, S.I. Rao, D.M. Dimiduk, M.D. Uchic, D.R. Trinkle, Contribution to size effect of yield strength from the stochastics of dislocation source lengths in finite samples, Scripta Mater, 56(2007) 313-6.

[88] S.H. Oh, M. Legros, D. Kiener, G. Dehm, In situ observation of dislocation nucleation and escape in a submicrometre aluminium single crystal, Nat Mater, 8(2009) 95-100.

[89] T. Tsuchiya, O. Tabata, J. Sakata, Y. Taga, Specimen size effect of tensile strength of surface-micromachined polycrystalline silicon thin films, J Microelectromech S, 7(1998) 106-13.

[90] R.M. Keller, S.P. Baker, E. Arzt, Quantitative analysis of strengthening mechanisms in thin Cu films: Effects of film thickness, grain size, and passivation, J Mater Res, 13(1998) 1307-17.

[91] E. Arzt, Overview no. 130 - Size effects in materials due to microstructural and dimensional constraints: A comparative review, Acta Mater, 46(1998) 5611-26.

[92] K. Jonnalagadda, N. Karanjgaokar, I. Chasiotis, J. Chee, D. Peroulis, Strain rate sensitivity of nanocrystalline Au films at room temperature, Acta Mater, 58(2010) 4674-84.

[93] N. Wang, Z.R. Wang, K.T. Aust, U. Erb, Room temperature creep behavior of nanocrystalline nickel produced by an electrodeposition technique, Mat Sci Eng a-Struct, 237(1997) 150-8.

[94] C.L. Wang, Y.H. Lai, J.C. Huang, T.G. Nieh, Creep of nanocrystalline nickel: A direct comparison between uniaxial and nanoindentation creep, Scripta Mater, 62(2010) 175-8.

[95] J. Weissmuller, J. Markmann, Deforming nanocrystalline metals: New insights, new puzzles, Adv Eng Mater, 7(2005) 202-7.

[96] G. Guisbiers, M.S. Colla, M. Coulombier, J.P. Raskin, T. Pardoen, Study of creep/relaxation mechanisms in thin freestanding nanocrystalline palladium films through the lab-on-chip technology, J Appl Phys, 113(2013).

[97] S. Baik, Mechanisms of creep-fatigue interaction: Cornell University, Jan.; 1982.

[98] Z. Sun, S. Van Petegem, A. Cervellino, K. Durst, W. Blum, H. Van Swygenhoven, Dynamic recovery in nanocrystalline Ni, Acta Mater, 91(2015) 91-100.

[99] I.C. Choi, Y.J. Kim, M.Y. Seok, B.G. Yoo, J.Y. Kim, Y.M. Wang, et al., Nanoscale room temperature creep of nanocrystalline nickel pillars at low stresses, Int J Plasticity, 41(2013) 53-64.

[100] W.M. Yin, S.H. Whang, R. Mirshams, C.H. Xiao, Creep behavior of nanocrystalline nickel at 290 and 373 K, Mat Sci Eng a-Struct, 301(2001) 18-22.

[101] V. Yamakov, D. Wolf, S.R. Phillpot, H. Gleiter, Grain-boundary diffusion creep in nanocrystalline palladium by molecular-dynamics simulation, Acta Mater, 50(2002) 61-73.

[102] S. Van Petegem, S. Brandstetter, B. Schmitt, H. Van Swygenhoven, Creep in nanocrystalline Ni during X-ray diffraction, Scripta Mater, 60(2009) 297-300.

[103] Z.S. Basinski, R. Pascual, S.J. Basinski, Low Amplitude Fatigue of Copper Single-Crystals .1. The Role of the Surface in Fatigue Failure, Acta Metall Mater, 31(1983) 591-602.

[104] N. Thompson, N. Wadsworth, N. Louat, The Origin of Fatigue Fracture in Copper, Philos Mag, 1(1956) 113-&.

[105] H. Mughrabi, Cyclic Slip Irreversibilities and the Evolution of Fatigue Damage, Metall Mater Trans B, 40(2009) 431-53.

[106] E.A. Repetto, M. Ortiz, A micromechanical model of cyclic deformation and fatigue-crack nucleation in fcc single crystals, Acta Mater, 45(1997) 2577-95.

[107] P.J.E. Forsyth, Exudation of Material from Slip Bands at the Surface of Fatigued Crystals of an Aluminium Copper Alloy, Nature, 171(1953) 172-3.

[108] B.T. Ma, C. Laird, Overview of Fatigue Behavior in Copper Single-Crystals .1. Surface-Morphology and Stage-I Crack Initiation Sites for Tests at Constant Strain Amplitude, Acta Metall Mater, 37(1989) 325-36.

[109] R.C. Boettner, A.J. Mcevily, Fatigue Slip Band Formation in Silicon-Iron, Acta Metall Mater, 13(1965) 937-&.

[110] J. Polak, P. Liskutin, Nucleation and Short Crack-Growth in Fatigued Polycrystalline Copper, Fatigue Fract Eng M, 13(1990) 119-33.

[111] B.L. Boyce, H.A. Padilla, Anomalous Fatigue Behavior and Fatigue-Induced Grain Growth in Nanocrystalline Nickel Alloys, Metall Mater Trans A, 42A(2011) 1793-804.

[112] P. Lukas, L. Kunz, M. Svoboda, Fatigue notch sensitivity of ultrafine-grained copper, Mat Sci Eng a-Struct, 391(2005) 337-41.

[113] A.B. Witney, P.G. Sanders, J.R. Weertman, J.A. Eastman, Fatigue of Nanocrystalline Copper, Scripta Metall Mater, 33(1995) 2025-30.

[114] H.W. Hoppel, Z.M. Zhou, H. Mughrabi, R.Z. Valiev, Microstructural study of the parameters governing coarsening and cyclic softening in fatigued ultrafine-grained copper, Philos Mag A, 82(2002) 1781-94.

[115] B. Moser, T. Hanlon, K.S. Kumar, S. Suresh, Cyclic strain hardening of nanocrystalline nickel, Scripta Mater, 54(2006) 1151-5.

[116] S.R. Agnew, A.Y. Vinogradov, S. Hashimoto, J.R. Weertman, Overview of fatigue performance of Cu processed by severe plastic deformation, J Electron Mater, 28(1999) 1038-44.

[117] H.W. Hoppel, Mechanical properties of ultrafine grained metals under cyclic and monotonic loads: An Overview, Mater Sci Forum, 503-504(2006) 259-66.

[118] H.W. Hoppel, M. Kautz, C. Xu, A. Murashkin, T.G. Langdon, R.Z. Valiev, et al., An overview: Fatigue behaviour of ultrafine-grained metals and alloys, Int J Fatigue, 28(2006) 1001-10.

[119] H. Mughrabi, H.W. Hoppel, M. Kautz, Microstructural aspects of cyclic deformation and fatigue of ultrafine-grained metals, Nato Sci Ser Ii Math, 212(2006) 209-16.

[120] A. Vinogradov, S. Hashimoto, Fatigue of severely deformed metals, Adv Eng Mater, 5(2003) 351-8.

[121] S.R. Agnew, J.R. Weertman, Cyclic softening of ultrafine grain copper, Mat Sci Eng a-Struct, 244(1998) 145-53.

[122] J. Rajagopalan, C. Rentenberger, H.P. Karnthaler, G. Dehm, M.T.A. Saif, In situ TEM study of microplasticity and Bauschinger effect in nanocrystalline metals, Acta Mater, 58(2010) 4772-82.

[123] H. Mughrabi, H.W. Hoppel, M. Kautz, Fatigue and microstructure of ultrafine-grained metals produced by severe plastic deformation, Scripta Mater, 51(2004) 807-12.

[124] H. Mughrabi, On the grain-size dependence of metal fatigue: Outlook on the fatigue of ultrafine-grained metals, Nato Sci S Prt 3 Hi, 80(2000) 241-53.

[125] T. Hanlon, Y.N. Kwon, S. Suresh, Grain size effects on the fatigue response of nanocrystalline metals, Scripta Mater, 49(2003) 675-80.

[126] S. Cheng, A.D. Stoica, X.L. Wang, G.Y. Wang, H. Choo, P.K. Liaw, Fracture of Ni with grain-size from nanocrystalline to ultrafine scale under cyclic loading, Scripta Mater, 57(2007) 217-20.

[127] P. Cavaliere, Fatigue properties and crack behavior of ultra-fine and nanocrystalline pure metals, Int J Fatigue, 31(2009) 1476-89.

[128] R.A. Meirom, D.H. Alsem, A.L. Romasco, T. Clark, R.G. Polcawich, J.S. Pulskamp, et al., Fatigue-induced grain coarsening in nanocrystalline platinum films, Acta Mater, 59(2011) 1141-9.

[129] R.A. Meirom, T.E. Clark, C.L. Muhlstein, The role of specimen thickness in the fracture toughness and fatigue crack growth resistance of nanocrystalline platinum films, Acta Mater, 60(2012) 1408-17.

[130] D. Farkas, S. Van Petegem, P. Derlet, H. Van Swygenhoven, Dislocation activity and nano-void formation near crack tips in nanocrystalline Ni, Acta Mater, 53(2005) 3115-23.

[131] D. Farkas, H. Van Swygenhoven, P. Derlet, Intergranular fracture in nanocrystalline metals, Phys Rev B, 66(2002) 060101.

[132] M.F. Ashby, R.A. Verrall, Diffusion-Accommodated Flow and Superplasticity, Acta Metall Mater, 21(1973) 149-63.

[133] S. Kumar, X. Li, A. Haque, H. Gao, Is stress concentration relevant for nanocrystalline metals?, Nano Lett, 11(2011) 2510-6.

[134] K. Hattar, J. Han, M. Saif, I. Robertson, In situ transmission electron microscopy observations of toughening mechanisms in ultra-fine grained columnar aluminum thin films, J Mater Res, 20(2005) 1869-77.

[135] R. Hugo, H. Kung, J. Weertman, R. Mitra, J. Knapp, D. Follstaedt, In-situ TEM tensile testing of DC magnetron sputtered and pulsed laser deposited Ni thin films, Acta Mater, 51(2003) 1937-43.

[136] H.-G. Kim, J.-W. Yi, S.-W. Kim, K.-S. Kim, K.S. Kumar, Fracture toughness of free-standing nanocrystalline copper–chromium composite thin films, Acta Mater, 84(2015) 95-109.

[137] K. Kumar, S. Suresh, M. Chisholm, J. Horton, P. Wang, Deformation of electrodeposited nanocrystalline nickel, Acta Mater, 51(2003) 387-405.

[138] S. Kumar, M. Haque, H. Gao, Notch insensitive fracture in nanoscale thin films, Appl Phys Lett, 94(2009) 253104.

[139] S. Kumar, M. Haque, H. Gao, Transformation induced toughening and flaw tolerance in pure nanocrystalline aluminum, Int J Plasticity, 44(2013) 121-8.

[140] R. Mitra, A. Chiou, J. Weertman, In situ study of deformation mechanisms in sputtered free-standing nanocrystalline nickel films, J Mater Res, 19(2004) 1029-37.

[141] H.T. Wang, A.M. Nie, J.B. Liu, P. Wang, W. Yang, B.D. Chen, et al., In situ TEM study on crack propagation in nanoscale Au thin films, Scripta Mater, 65(2011) 377-9.

[142] Y. Zhang, F. Wang, P. Zang, J. Wang, S. Mao, X. Zhang, et al., In-situ observation of crack propagation through the nucleation of nanoscale voids in ultra-thin, freestanding Ag films, Materials Science and Engineering: A, 618(2014) 614-20.

[143] P. Derlet, H.V. Swygenhoven, The role played by two parallel free surfaces in the deformation mechanism of nanocrystalline metals: a molecular dynamics simulation, Philosophical Magazine A, 82(2002) 1-15.

[144] B. Pant, S. Choi, E.K. Baumert, B.L. Allen, S. Graham, K. Gall, et al., MEMS-Based Nanomechanics: Influence of MEMS Design on Test Temperature, Exp Mech, 52(2012) 607-17.

[145] MEMSCAP, SOIMUMPs, MEMSCAP Corporation2003.

[146] B. Pant, Experimental nanomechanics of 1D nanostructures, (2010).

[147] D. Caillard, J.L. Martin, Thermally Activated Mechanisms in Crystal Plasticity: Elsevier Science; 2003.

[148] W.D. Nix, Mechanical properties of thin films, Metallurgical and Materials Transactions A, 20(1989) 2217-45.

[149] M. Yilmaz, J.W. Kysar, Monolithic integration of nanoscale tensile specimens and MEMS structures, Nanotechnology, 24(2013).

[150] M.A. Haque, M.T.A. Saif, Mechanical behavior of 30-50 mn thick aluminum films under uniaxial tension, Scripta Mater, 47(2002) 863-7.

[151] K.F. Murphy, L.Y. Chen, D.S. Gianola, Effect of organometallic clamp properties on the apparent diversity of tensile response of nanowires, Nanotechnology, 24(2013).

[152] R. Agrawal, B. Peng, H.D. Espinosa, Experimental-Computational Investigation of ZnO nanowires Strength and Fracture, Nano Lett, 9(2009) 4177-83.

[153] R.A. Bernal, R. Agrawal, B. Peng, K.A. Bertness, N.A. Sanford, A.V. Davydov, et al., Effect of Growth Orientation and Diameter on the Elasticity of GaN Nanowires. A Combined in Situ TEM and Atomistic Modeling Investigation, Nano Lett, 11(2011) 548-55.

[154] T. Filleter, R. Bernal, S. Li, H.D. Espinosa, Ultrahigh Strength and Stiffness in Cross-Linked Hierarchical Carbon Nanotube Bundles, Adv Mater, 23(2011) 2855-+.

[155] T. Filleter, S. Ryu, K. Kang, J. Yin, R.A. Bernal, K. Sohn, et al., Nucleation-Controlled Distributed Plasticity in Penta-twinned Silver Nanowires, Small, 8(2012) 2986-93.

[156] S. Gupta, O.N. Pierron, MEMS based nanomechanical testing method with independent electronic sensing of stress and strain, Extreme Mechanics Letters, (2016).

[157] H.D. Espinosa, B.C. Prorok, B. Peng, Plasticity size effects in free-standing submicron polycrystalline FCC films subjected to pure tension, J Mech Phys Solids, 52(2004) 667-89.

[158] J. Rajagopalan, J.H. Han, M.T.A. Saif, Plastic deformation recovery in freestanding nanocrystalline aluminum and gold thin films, Science, 315(2007) 1831-4.

[159] C.J. Youngdahl, J.R. Weertman, R.C. Hugo, H.H. Kung, Deformation behavior in nanocrystalline copper, Scripta Mater, 44(2001) 1475-8.

[160] A.G. Froseth, P.M. Derlet, H. Van Swygenhoven, Twinning in nanocrystalline fcc metals, Adv Eng Mater, 7(2005) 16-20.

[161] H. Van Swygenhoven, P.M. Derlet, A.G. Froseth, Stacking fault energies and slip in nanocrystalline metals, Nat Mater, 3(2004) 399-403.

[162] G. Grochola, S.P. Russo, I.K. Snook, On fitting a gold embedded atom method potential using the force matching method, J Chem Phys, 123(2005).

[163] S. Kumar, M.T. Alam, M.A. Haque, Fatigue Insensitivity of Nanoscale Freestanding Aluminum Films, J Microelectromech S, 20(2011) 53-8.

[164] K.J. Hemker, H. Last, Microsample tensile testing of LIGA nickel for MEMS applications, Mat Sci Eng a-Struct, 319(2001) 882-6.

[165] B. Pant, B.L. Allen, T. Zhu, K. Gall, O.N. Pierron, A versatile microelectromechanical system for nanomechanical testing, Appl Phys Lett, 98(2011).

[166] G.D. Sim, J.J. Vlassak, High-temperature tensile behavior of freestanding Au thin films, Scripta Mater, 75(2014) 34-7.

[167] R. Raj, M.F. Ashby, Grain Boundary Sliding and Diffusional Creep, Metall Trans, 2(1971) 1113-&.

[168] R.L. Coble, A Model for Boundary Diffusion Controlled Creep in Polycrystalline Materials, J Appl Phys, 34(1963) 1679-&.

[169] E. Hosseinian, M. Legros, O.N. Pierron, Quantifying and observing viscoplasticity at the nanoscale: highly localized deformation mechanisms in ultrathin nanocrystalline gold films, Nanoscale, 8(2016) 9234-44.

[170] J. Cook, C.C. Evans, J.E. Gordon, D.M. Marsh, Mechanism for Control of Crack Propagation in All-Brittle Systems, Proc R Soc Lon Ser-A, 282(1964) 508-+.

[171] Y.F. Zhang, F. Wang, P. Zang, J. Wang, S.C. Mao, X.N. Zhang, et al., In-situ observation of crack propagation through the nucleation of nanoscale voids in ultra-thin, freestanding Ag films, Mat Sci Eng a-Struct, 618(2014) 614-20.

[172] I.A. Ovid'ko, A.G. Sheinerman, Generation and growth of nanocracks near blunt cracks in nanocrystalline solids, Eur J Mech a-Solid, 33(2012) 39-47.

[173] F. Mompiou, M. Legros, A. Boe, M. Coulombier, J.P. Raskin, T. Pardoen, Inter- and intragranular plasticity mechanisms in ultrafine-grained Al thin films: An in situ TEM study, Acta Mater, 61(2013) 205-16.

[174] S.V. Bobylev, A.K. Mukherjee, I.A. Ovid'ko, A.G. Sheinerman, Effects of intergrain sliding on crack growth in nanocrystalline materials, Int J Plasticity, 26(2010) 1629-44.

[175] D.S. Gianola, C. Eberl, Micro- and nanoscale tensile testing of materials, Jom-Us, 61(2009) 24-35.